Marine and Petroleum Geology
June 2021, Volume 128, Pages 105002 (29p.)
https://doi.org/10.1016/j.marpetgeo.2021.105002
https://archimer.ifremer.fr/doc/00683/79475/

Siliciclastic and bioclastic contouritic sands: textural and geochemical characterisation

de Castro S. [1, *], Miramontes E. [2, 3], Dorador J. [1], Jouet Gwenael [4], Cattaneo Antonio [4],
Rodríguez-Tovar F.J. [5], Hernández-Molina F.J. [1]

[1] Dept. Earth Sciences, Royal Holloway Univ. London, Egham, Surrey TW20 0EX, United Kingdom
[2] Faculty of Geosciences, University of Bremen, 28359 Bremen, Germany
[3] MARUM – Center for Marine and Environmental Sciences, University of Bremen, Bremen 28359, Germany
[4] IFREMER, Unité Géosciences Marines, Plouzané, France
[5] Departamento de Estratigrafía y Paleontología, Universidad de Granada, 18002 Granada, Spain

* Corresponding author : S. de Castro, email address : Sandra.deCastroSantos.2017@live.rhul.ac.uk

Abstract :

The purpose of this study is to differentiate and characterise contouritic sands in two different locations with variable sediment compositions (siliciclastic and bioclastic) based on a multiproxy approach that includes the analysis of sedimentary texture, semi-quantitative geochemistry, microfacies and ichnological information, as well as a Principal Component Analysis (PCA) applied to geochemical and sedimentary data on sediment cores. The integration of sedimentological analyses and the PCA permits also to the differentiation between fine-grained deep-water deposits such as hemipelagites, muddy contourites and hyperpycnites. A depositional model is proposed here, based on geochemical and sedimentological characteristics of the Holocene-highstand Mozambique Channel upper slope sands, and glacial-lowstand Corsica Contourite Depositional System middle slope sands. The upper continental slope of the Mozambican margin is characterised by siliciclastic sandy contourites, muddy contourites and muddy hyperpycnites. Mozambique siliciclastic sandy contourites constitute large accumulations of well-sorted very fine to coarse sand with evidences of strong winnowing and reworking under high-energy conditions. The sedimentary facies represents highstand contourite sands and shows a reversely-graded trend. The contourite drift on the Pianosa ridge (eastern flank of the Corsica Trough) consists of bioclastic sandy and muddy contourites and hemipelagites. Bioclastic sandy contourites are made up of shallow-marine winnowed bioclasts with a reversely- and normally-graded trend and represent lowstand contourite sands. The PCA in the two environments —showing a distinctive geochemical signal— allows for differentiation of the contourite deposits. In siliciclastic sands, reworking is marked by an accumulation of Si, Zr, and Sr in fine- to medium-grained sands. In bioclastic sands, reworking is less evident but it is characterised by accumulations of Ca and Sr. The reworking and winnowing bottom current effects are also observed at the microfacies scale. Both types of contourite deposits show evidences of intermittent depositional conditions depending on the ichnodiversity, distribution and abundance of trace fossils. This work is useful to discriminate similar fine-grained deposits in different continental margins which would contribute to a better understanding of sedimentary deposits and processes in deep-marine environments.

Graphical abstract

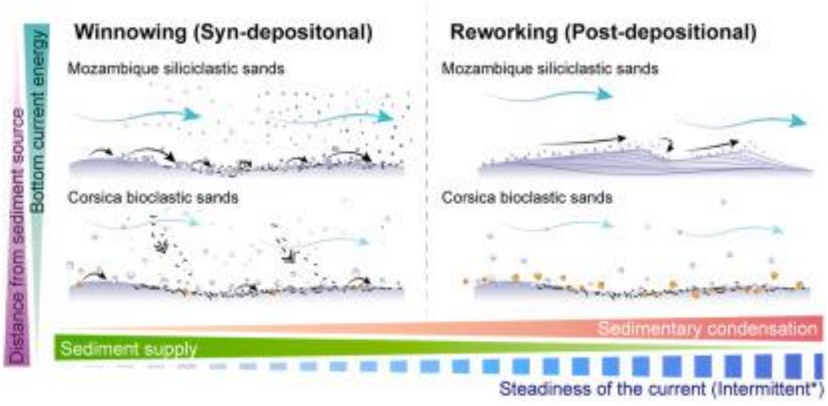

Highlights

► Reworking proxies are different for bioclastic and siliciclastic sands ► Winnowing and reworking bottom current effects have a distinctive geochemical signal and they are observed at the microfacies scale ► Bi-gradational contourite sequence show evidences of intermittent depositional conditions ► Sediment input and distance to sediment source has a strong impact on the bi-gradational contourite sequence formation ► Contourite drifts are not only formed by contourite deposits

Keywords : hemipelagite, contourite, hyperpycnite, reworking, winnowing, sediment transport, Mozambique Channel, Corsica

1. INTRODUCTION

Along-slope bottom (contour) currents can generate vast erosional or depositional features that strongly influence a margin's overall sedimentary architecture (Rebesco et al., 2014; Miramontes et al., 2020a). If bottom currents are the dominant depositional process, a Contourite Depositional System develops (CDS; Hernández-Molina et al., 2008). These systems are composed of depositional (contourite drifts), erosional (contourite channels, moats, furrows) or mixed depositional-erosional elements (contourite terraces, subcircular depressions). Contourites have to do with their depositional elements (Faugères et al., 1999; Hernández-Molina et al., 2008), as large sediment accumulations result from the semi-continuous long-term activity of bottom-currents (Rebesco et al., 2014). Researchers have also increasingly recognised the role of bottom currents in effectively modifying or entirely obliterating evidence of gravity flow processes (Rebesco et al., 2002; Mutti et al., 2014; Badalini et al., 2016; Creaser et al., 2017; Mulder et al., 2018a, b; Wang et al., 2018; Fonnesu et al., 2020; Fuhrmann et al., 2020; Miramontes et al., 2020a), or in reworking hemipelagic deposits (Gambacorta et al., 2014; Hüneke et al., 2020).

The three main sedimentary processes in deep-water environments are the settling of pelagic and hemipelagic particles in the water column, sediment gravity flows, and bottom-current controlled sedimentation (Hüneke and Mulder, 2011; Rebesco et al., 2014; Stow and Smillie, 2020). Turbidite deposits commonly reflect a gradual decrease in flow velocity. The gradual decrease in velocity is responsible for the fining-upward grain size distribution in these deposits, and reflects a change from rapid deposition to sedimentation by sediment fallout (Middleton and Hampton, 1973; Shanmugam, 2006, 2016). Consequently, the finest part of the turbidite sequence, which is the suspension fallout of the turbidity cloud, shows a very close resemblance to hemipelagic deposition (Stow and Wetzel, 1990). Given that suspension fallout deposition takes a significant amount of time, these deposits might also be mixed with the normal hemipelagic settling. Long-term gravity currents induced by changes in river discharge rates (hyperpycnal flows) can also generate similar sedimentary facies (Mulder and Alexander, 2001; Mulder et al., 2003). The same is applicable for fine-grained contourite deposits, which can be an admixture of contouritic and hemipelagic sediments (Stow and Smillie, 2020). This continuum of sediment mixing could include a variety of sedimentary facies showing attributes related to gravity, contouritic and hemipelagic processes (Stanley, 1988; Hüneke and Stow, 2008; Mulder et al., 2008). However, despite the co-occurrence of these processes in the sedimentary record, we often lack indisputable diagnostic criteria to identify and differentiate between hemipelagites, contourites and hyperpycnites. Although the three endmembers facies models are very distinct, discerning them is still problematic, especially when data is limited to the diameters of a core. Understanding the sedimentological origin of these deep-water deposits is fundamental for: palaeoclimatology and palaeoceanography research (Rebesco et al., 2014); slope-stability/geological hazard assessment (Miramontes et al., 2018); hydrocarbon exploration (Rebesco et al., 2005; Viana et al., 2008; Fonnesu et al., 2020); and recently for studying distribution of microplastics in the seafloor as well (Näkki et al., 2017, 2019; Courtene-Jones et al., 2019; Kane et al., 2020).

The purposes of this study are to characterise different contourite sands having different sediment compositions (siliciclastic and bioclastic) and to differentiate hemipelagite, contourite and hyperpycnite deep-water sedimentary deposits in two different settings based on sedimentological analyses and by applying a Principal Component Analysis (PCA) to geochemical and sedimentological data from sediment cores. Two sediment cores were retrieved from two contourite drifts located in the upper continental slope of the Mozambican margin (The Mozambique Channel; Fig. 1A and B) and the eastern flank of the Corsica Trough (CDS of the Pianosa Ridge, Fig. 1C and D). In addition, the following objectives are pursued: i) to characterise the vertical association of hemipelagites, turbidites and contourites in view of their sedimentary texture and geochemical signals; ii) to discuss the applied methodology in terms of the effects of bottom currents on deep-water sedimentation; iii) to examine the hydrodynamic behaviour of the components of different compositional contouritic sands; and iv) to establish the controlling factors on the deposition of contouritic sands and how they contribute to overall contourite construction along different continental margins.

2. MORPHOSEDIMENTARY AND OCEANOGRAPHIC FRAMEWORK

2.1. Mozambique Channel

The Mozambique Channel is located in the southwest Indian Ocean, between the East African continental margin of Mozambique and Madagascar (Fig. 1A). The Mozambican continental slope hosts a contourite depositional system with erosive (abraded surfaces, contourite channels, moats, furrows and scours), depositional (plastered and elongated-mounded drifts, sedimentary waves), and mixed (terraces) features (Thiéblemont et al., 2019).

The upper continental slope of the Mozambican margin consists laterally of: a) a convex slope with a plastered drift and a contourite terrace to the southwest, offshore the Zambezi delta (Figs. 1B and 2A; Thiéblemont et al., 2019); and b) a concave slope with a plastered drift and a dune field, 50 km further northeast or west offshore the Zambezi delta (Miramontes et al., 2020b). This work focuses on the sector between the distal part of that contourite terrace and the deeper adjacent plastered drift (core MOZ4-CSF19; Fig. 1A). In this area (at about 300 m water depth), the seafloor is covered by straight to slightly sinuous sandy current ripples (Fig. 2B in Miramontes et al., 2020b). The principal source of sediment feeding this part of the continental slope along the Mozambique Channel is the Zambezi River (Fig. 1A) — it is the largest single suspended sediment supplier and drains a considerable part of the southeast African continent (Walford et al., 2005). Due to the prevailing easterly winds and the absence of other large regional dust source areas, lithogenic sediments in the Mozambique Channel have a predominantly riverine origin, and their composition is directly related to continental climatic conditions (van der Lubbe et al., 2016).

The surface and upper-intermediate oceanic circulation along the upper Mozambican continental slope consists primarily of the southward-flowing Mozambique Current (MC; Fig. 1A; de Ruijter et al., 2002), which is part of the Agulhas current system (Lutjeharms, 2006). It is characterised by anticyclonic eddies (ME, Mozambique eddies) with diameters of ∼300 km able to affect the whole water column and generate currents up to 2 m s^{-1} at the surface and 0.5 m s^{-1} in the deep part of the basin (Fig. 1A; Miramontes et al., 2019a). The MC carries Tropical Surface Water, Subtropical Surface Water (TSW and STSW, respectively; <300 m water depth), South Indian Central Water (SICW, between 300 and 600 m water depth) (de Ruijter et al., 2002), and the northwest Indian-origin intermediate water mass of Red Sea Water (RSW, 900–1200 m water depth) (Beal et al., 2000; Donohue et al., 2000; Swart et al., 2010). Below the MC, the Antarctic Intermediate Water (AAIW) enters from the south as part of the Mozambique Undercurrent (MUC; de Ruijter et al., 2002; Ullgren et al., 2012) (Fig. 1A). The upper slope of the Mozambique margin is affected by internal waves that have been suggested to generate a channel and sand dunes on the landward part of the contourite terrace (Miramontes et al., 2020b).

2.2. Corsica Trough

The Pianosa CDS (Miramontes et al., 2016) is located in the Corsica Trough, a narrow basin in the Northern Tyrrhenian Sea. It is flanked by Corsica Island to the west and by the Pianosa Ridge and the Tuscan shelf to the east (Fig. 1C). The Pianosa CDS is located along the upper and middle continental slope between 170 and 850 m water depth. It is 120 km long, has a maximum width of 10 km and is composed of a large muddy sediment plastered drift, which may form locally mounded and separated or multicrested drifts (Miramontes et al., 2016; Fig. 1C). The area of study lies offshore of the Pianosa Island. In this zone, faster bottom currents formed moats and associated contourite drifts along the slope (Fig. 1D) (Miramontes et al., 2016). The studied site (PSM3-CS009) is located at 370 m water depth in the crest of a mounded drift on the slope (Figs. 1D and 2C). The western side of the Corsica Trough is dominated by downslope gravity-driven depositional processes (Fig. 1C) that resulted in the formation of the Golo turbidite system (Gervais et al., 2004, 2006; Deptuck et al., 2008; Calvès et al., 2013; Sweet et al., 2020).

The Pianosa CDS developed under the influence of Levantine Intermediate Water (LIW). The LIW is located just below the Modified Atlantic Water (MAW), that circulates at water depths ranging from the sea surface to 200 m (Astraldi and Gasparini, 1992; La Violette, 1994; Millot, 1999). Circulation along the eastern part of the Corsica Trough is characterised by northward-flowing currents that change seasonally, being enhanced during the cold seasons (reaching 10–40 cm s^{-1}) (Astraldi and Gasparini, 1992; Vignudelli et al., 1999; Miramontes et al., 2019b). This seasonality is related to the LIW formation process, which is formed by a process of evaporation during the summer in the southeastern Mediterranean Sea, resulting in a warm and salty surface water mass; later, winter cooling increases its density. More arid and colder climatic conditions could therefore favour the production of denser LIW (Cacho et al., 2000) enhancing the Mediterranean Outflow Water (MOW) at the exit of the Strait of Gibraltar (Sierro et al., 1999, 2020).

3. MATERIAL AND METHODS

3.1. Bathymetry and seismic data

The regional bathymetry used for Mozambique Channel (Fig. 1A) is GEBCO bathymetry (GEBCO_08, version 2010-09-27; http://www.gebco.net), with a 30 arc-second resolution. The main multibeam bathymetric data shown in the present study were collected during the PAMELA-MOZ04 survey in 2015 (R/V Pourquoi pas?; Jouet and Deville, 2015). The multibeam bathymetry from the Corsica Trough (Fig. 1B) was acquired during the SIGOLO survey in 2008 (Savoye, 2008) and completed with the zone of the Pianosa Ridge during surveys PRISME2 (Cattaneo, 2013a), PAMELA-PAPRICA (Cattaneo and Jouet, 2013) and PRISME3 (Cattaneo, 2013b) carried out by IFREMER in 2013 onboard the R/V Atalante and the R/V Pourquoi pas?, respectively. The outer bathymetric data of the northern Tyrrhenian Sea were retrieved from the EMODnet Bathymetry compilation (http://portal.emodnet-bathymetry.eu/). The seismic data used to locate the cores correspond to a 72-channel high-resolution mini GI-gun seismic reflection profile (50–250 Hz) collected in the Mozambique Channel during the PAMELA-MOZ04 cruise (Jouet and Deville, 2015) and a sub-bottom profiler profile (1800-5300 Hz) collected in the Corsica Trough during the PRISME2 cruise (Cattaneo, 2013a).

3.2. Grain size analysis

The 9.24 m long Calypso piston core in the Mozambique Channel (MOZ4-CSF19, Table 1) was collected during the PAMELA-MOZ04 survey (Jouet and Deville, 2015) in 2015 on the upper continental slope at 315 m water depth, in the offshore zone of a contourite terrace (Fig. 1B). MOZ4-CSF19 was sampled for grain size analysis with 10 cm spacing including 92 splits of core material. The Calypso piston core used in the Pianosa CDS (PSM3-CS009; Table 1) was collected during the PRISME3 cruise (Cattaneo, 2013b) in 2013 along the Pianosa Ridge at 370 m water depth. PSM3-CS009 was sampled for grain size analysis with variable spacing, ranging from 10 cm (in the homogeneous muddy facies) to 2 cm (in the sandy areas and mud-sand transitions), giving a total of 310 sediment samples. Grain size measurements were performed on core MOZ4-CSF19 using a Malvern Mastersizer 3000 laser diffraction particle size analyser and on core PSM3-CS009 using a Coulter LS200 laser diffraction particle size analyser. In both cores, measurements were performed in the bulk sediment with no chemical pre-treatment. Grain size parameters were analysed by means of Gradistat software, adopting its grain size scale (Blott and Pye, 2001). Mean grain size, sorting, skewness, and kurtosis were calculated using the method of Folk and Ward (1957). Results were compared by cross-plots (Folk and Robles, 1964; Martins, 2003).

3.3. X-Ray Fluorescence (XRF) and Principal Component Analysis (PCA)

In MOZ4-CSF19 and PSM3-CS009 cores, the bulk sediment semi-quantitative geochemical composition was measured at 1-cm intervals using an Avaatech X-Ray Fluorescence (XRF) core scanner at IFREMER on split cores. Sampling time was 10 s at the split core surface, with respective generator settings of 10 and 30 kV at 0.6 mA and 1 mA. Data were retained only from elements that gave consistently good signal quality (i.e., Al, Si, K, Ca, Ti, Mn, Br, Fe, Sr, and Zr). These elements were normalised according to their mean values and standard deviations at each core.

To investigate the different factors influencing the geochemical composition of the sediment, Principal Component Analysis (PCA) was conducted using the PAST version 4.0 software package (Hammer et al., 2001). PCA is a well-established dimension-reducing statistical technique, applied for pattern recognition in multivariate datasets (Wold et al., 1987; Zou et al., 2006; Abdi and Williams 2010). The calculated eigenvalues provide a measure of the variance accounted for by the corresponding components (axes of the PCA). Recently, de Castro et al. (2020b) proposed a PCA-based method that serves to discriminate hemipelagic deposits from other sediments affected by bottom current reworking and winnowing processes in a contourite drift, in the Gulf of Cadiz CDS. The calculated eigenvalues indicate the variance accounted for the corresponding components downcore (i.e., grain size and major element geochemistry). Hemipelagic deposits were defined by high loading of the first principal component (PC1), as they represent the background sedimentation in deep-marine settings. In the Gulf of Cadiz CDS (de Castro et al., 2020b), this PC1 is characterised by the aluminosilicate element association (Al, K, Fe and Rb) in fine-grained sediment (silt-clay). Once the settling of sediment is affected by other deep-water sediment processes, such as bottom currents, the variance and loading of this PC1 decrease drastically. The main advantage of this statistical method lies in its comparatively quick examination and distinction of facies showing very subtle changes (e.g., hemipelagites from muddy contourites or muddy hyperpycnites and turbidites from sandy contourites).

3.4. 2D X-Ray images (XCT)

2D X-Ray images were obtained from split sections of core MOZ4-CSF19 using a Geotek-XCT system at the IFREMER laboratories, Brest (France). X-Ray scans were also performed on slabs collected from three sections from core MOZ4-CSF19 (S1, S2 and S3) and one section from core PSM3-CS009 (S14) in order to reduce the imaged volume and thus to better observe the sedimentary and the biogenic structures. The resolution of the images is 1 mm.

3.5. Thin sections

Samples for thin sections were obtained from MOZ4-CSF19 and PSM3-CS009 (Table 1). The database includes 6 large (10 × 5 cm) thin sections in MOZ4-CSF19 and 3 large (10 × 5 cm) thin sections in PSM3-CS009. Thin sections of impregnated sediments were used to document sedimentary structures and microfacies variation at the bed scale; they were prepared at the University of Greifswald (Germany). The relative percentage frequency of different components was determined by means of the visual-comparison charts of Baccelle and Bosellini (1965) and Matthew et al. (1991).

3.6. Sediment dating

The cores used in this study were dated by means of radiocarbon measurements on bulk planktonic foraminifera. Radiocarbon ages of core PSM3-CS009 (Table 2) were obtained at Poznan and Beta Analytic laboratories, they were calibrated using Calib 8.2 software (Stuiver et al., 2020) and the Marine20 calibration curve (see Heaton et al., 2020). Radiocarbon ages of core MOZ4-CSF19 (Table 2) were measured at Beta Analytic laboratories and were calibrated using the Marine20 calibration curve (Heaton et al., 2020).

3.7. Ichnological analysis

Ichnological analysis of core samples was conducted after digital enhancement of high-resolution images to increase visibility of biogenic structures. This procedure is described in Dorador et al. (2014a, 2014b) and Dorador and Rodríguez-Tovar (2018). Ichnogenera characterisation was conducted based on the recognition of ichnotaxobases (Knaust, 2017). Special attention was paid to the distribution of traces and their infilling material. Moreover, ichnofabrics were differentiated mainly based on ichnological attributes: ichnodiversity, cross-cutting relationships, tiering structure, relative abundance and degree of bioturbation (Rodríguez-Tovar and Dorador, 2014; Dorador and Rodríguez-Tovar, 2016).

3.8. Nomenclature

The term “contourite” is used for sediments deposited or substantially reworked by the persistent action of bottom currents (Faugères and Stow, 2008; Rebesco et al., 2014). Thick, extensive contourite sediment accumulations are defined as contourite drifts. Interpretation of these features follows the criteria for drift morphologies and internal configurations defined by Faugères et al. (1999) and Rebesco et al. (2014). The classification of bioclastic and siliciclastic contourite deposits is based on Rebesco et al. (2014). In turn, “hemipelagic deposits” is used for sediments deposited from both vertical settling and slow lateral advection through the water column (Hesse, 1975; O'Brien et al., 1980; Stow and Tabrez, 1998; Stow and Smillie, 2020). "Turbidites" refer to beds deposited rapidly (from a few hours to a few days) from a single sedimentation event, in which the granular materials are mainly supported by turbulence while deposition occurs through traction sedimentation and suspension settling (Middleton and Hampton, 1973; Lowe, 1982; Stow and Piper, 1984; Talling et al., 2012). "Hyperpycnite" refers to a fine-grained deposit characterised by a coarsening and then fining upward bed, reflecting an increasing and then decreasing magnitude in the fluvial-related discharge (Mulder and Alexander 2001). A hyperpycnal flow is defined according to the density-contrast at the coastline between that of an incoming river-derived relatively dense flow and that of the water in a water body that last for days, weeks or even months (Zavala, 2020).

4. RESULTS AND INTERPRETATION

4.1. Mozambique Channel

The MOZ4-CSF19 core comprises two main deposits with different grain sizes: coarse-grained sediments at the core top (Fig. 3A) and fine-grained sediments at the bottom of the core. The integrated analysis of the sediment core allowed us to identify three facies that we will detail in this section (Table 3). The upper 2.1 m of the sediment core are mainly composed of coarsening-up sandy deposits defined as Mozambique Facies 1 (MF1). Muddy sediments represent a 6.9 m-thick homogeneous succession below MF1 (Fig. 3A) that can be separated into two facies —Mozambique Facies 2 (MF2) and 3 (MF3). Radiocarbon dating shows that the coarse-grained sediments (MF1) are younger than 9 kyr BP, whereas the fine-grained sediments are dated up to 17.2 kyr BP (Fig. 3A).

Mozambique Principal Component Analysis (M-PCA)

The MOZ4-CSF19 PCA of semi-quantitative geochemical composition (XRF) gave two significant Principal Components (PC) in the Mozambique Channel sediments (Table 2). The first two axes of the PCA respectively yield variance percentages of 52% and 18%, accounting for 70% of the total variability (Table 2). The main positively-loaded elements in M-PC1 are Si, Ca, Sr and Zr, as opposed to the main negatively-loaded Al, K, Ti, Fe and Rb (Fig. 3A). The main positively-loaded elements in M-PC2 consist of Si, K, Ti, Br, Rb and Zr against the negatively-loaded Al and Fe (Fig. 3B).

Ichnological analysis

The analysis of high-resolution images and XCT of MOZ4-CSF19 core reveal a moderately diverse trace fossil assemblage (Figs. 4 and 8), mainly consisting of *Palaeophycus*, *Planolites*, and *Thalassinoides*, occasional *Nereites* and *Scolicia*, and rarely possible *Skolithos* and *Mycellia*. In some facies (*see below*) a mottled background determined by biodeformational structures (i.e., structures having no distinct outlines and no recurrent geometry) is observed. Ichnological features allow for differentiation of three ichnofabrics: i1) *Mottled background with fine-grained infilled traces ichnofabric*, characterised by *Planolites*, *Palaeophycus* and *Scolicia* filled by fine-grained material, similar to the host sediment, over a mottled background; i2) *Fine-grained sediment with coarse-grained infilled trace ichnofabric*, consisting of fine-grained sediment with *Thalassinoides* and *Planolites* filled by coarse-grained material; and i3) *Mottled background with coarse-grained infilled trace ichnofabric*, intensely bioturbated, showing a well-developed mottled background and *Planolites* and *Thalassinoides* filled by coarse-grained material similar to the host sediment. Ichnological features, including differentiated ichnofabrics, indicate variable vertical distribution.

Mozambique Facies 1 (MF1): Mottled fine-grained sand

This facies is found at 0-2.13 m below the seafloor (mbsf; Fig. 3A) and consists of structureless mottled siliciclastic coarse-grained silt to fine-grained sand (19.1-152.6 µm). It comprises a 2.13 m-thick reversely-graded bed with subtle changes in grain size volume throughout the sequence (Fig. 3A). It is characterised by a gradational base and the seafloor at its top, which shows long, crested, slightly sinuous current ripples (Fig. 2B). The sediment is poorly to very poorly sorted (Fig. 5A) and has a unimodal grain size distribution ranging from platykurtic to very leptokurtic, with a fine to very fine skew (Fig. 5B). A positive excursion is observed in M-PC1, with an increasing-upward trend from 2 to 0 mbsf, and M-PC2 is positively loaded between 0.77 and 2.91 mbsf (Fig. 3A). At 0.77-2 mbsf, M-PC1 and M-PC2 show positive values in fine-grained sands (Fig. 3A). The XRF K+Fe+Ti/Ca+Sr curve decreases from 2.13 to 0 mbsf, whereas the XRF Zr/Ti curve increases upwards, which is well correlated with the grain size distribution curve and the M-PC1.

The trace fossil assemblage consists of *Palaeophycus*, *Planolites*, *Thalassinoides* and occasional *Scolicia* (Fig. 4A-F). The three differentiated ichnofabrics are recognised with the i1, i2 and i3 stacked vertical trend (Fig. 4A-F). An irregular surface can be identified at 0.7 mbsf, under which *Thalassinoides* are very well developed (Fig. 4A and B). Between 1.88 and 2.13 mbsf, the sediment is darker than in the rest of the sequence (Fig. 4E and F).

Thin sections show different textures from the base to the top. The top of MF1 lacks on matrix content, yet bioclasts, foraminifers and accessory minerals contents increase (Fig. 7A, B and C). Here, the microfacies consist of massive grain-supported quartz grains (40-60%), planktonic foraminifers (5-15%), benthic foraminifers (5%), and other bioclasts (5-20%). Quartz grains usually show remains of a residual matrix attached to the grains in MOZ4-S2 (Fig. 7C), but towards the top of the sequence, quartz grains lack any residual matrix (Fig. 7A and B). Other bioclasts include bivalve fragments, coralline algae, echinoid spines, and gastropod shells, and most of them reaching up to 0.5 mm (Fig. 7C). Accessory minerals are characterised by dark minerals (potentially iron oxides), amphibole, pyroxene, titanite, epidote and zircon, the latter more abundant towards the top of MF1 (Fig. 7A and B). Glauconite grains are rare throughout MF1. The base of MF1 features a patchy texture between matrix-rich (20-50% matrix; Table 4, Fig. 6B and 7D) and matrix-free (0% matrix; Table 4, Fig. 6A, 7E and F) cm-scale irregular patches resulting from intensive bioturbation (Fig. 6A). The grains consist of predominantly subangular quartz (up to 70%; Table 4) with other bioclasts and foraminifers, and common accessory minerals (Fig. 7E and F) such as transparent heavy minerals: opaques, amphibole, pyroxene, epidote and zircon (Fig. 7E and F). Muscovite, chlorite and biotite comprise the micas as acicular grains and may have a preferential oblique orientation (Fig. 7F) or lack any orientation. The argillaceous iron-rich matrix supported areas show a similar composition, with dominant subangular quartz grains and a few planktic foraminifers (Fig. 7D). In these areas, accessory minerals are less common (Fig. 7D).

Mozambique Facies 2: Homogenous medium-grained silt

Mozambique Facies 2 (MF2) (2.13-4.74 and 5.75-9 mbsf; Fig. 3A) consists of homogenous fine- to medium-grained silt (4.9-20.32 µm). This facies shows gradational top and bottom contacts (Figs. 4E and F; 8A and B). The sediment is very poorly sorted (Fig. 5A) and has a polymodal mesokurtic grain-size distribution, with an overall symmetrical skew (Fig. 5B). MF2 shows negative or zero values in both M-PC1 and M-PC2 (Fig. 3A). The XRF K+Fe+Ti/Ca+Sr curve has higher values than in MF1 (Fig. 3A). The Zr/Ti ratio is perfectly correlated with the grain size distribution curve, showing no important variations.

MF2 presents similar trace fossil assemblages to those of MF1, with the presence of *Palaeophycus*, *Planolites, Thalassinoides*, *Nereites,* possible *Skolithos and Mycellia*. Noteworthy are the absence of *Scolicia*, and the abundance of *Palaeophycus,* concentrated in high-density intervals (Fig. 4E). The three ichnofabrics i1, i2 and i3 can be recognised and show a clear differentiation: i1 is the more extended, whereas i2 is registered only in a short interval, in the transition with MF1. Here, in i1 some *Thalassinoides* are filled by coarse-grained sediment. (Fig. 4E and F).

Microfacies from MF2 shows a matrix-supported patchy texture with abundant subangular quartz grains (up to 50%; Table 4) and rare foraminifers and other bioclasts (Fig. 7G and H). The matrix content is variable throughout the thin section (25-85%; Table 4) and is composed of very fine-grained iron-rich argillaceous material (Fig. 7G and H). Opaque minerals are common, but epidote, zircon, amphibole and pyroxene are less abundant than in MF1 (1-5%; Table 4).

Mozambique Facies 3: Thin-bedded medium-grained silt

Mozambique Facies 3 (MF3) (4.74-5.75 mbsf; Fig. 3A) is characterised by homogenous fine- to medium-grained silt (4.9-12.3 µm). This facies consists of approximately 1 m-thick massive silt with gradational top and bottom contacts (Fig. 8A and B). In the X-Ray images, two subdivisions are recognised. The lower interval is characterised by silty thin beds of 3-5 cm thick. The upper interval consists of well-developed parallel to low-angle laminated muddy silts consisting of 1-2 cm-thick very thin beds (Fig. 8A and B). The sediment is very poorly sorted (Fig. 5A) and has a polymodal platykurtic grain-size distribution, with a coarse to symmetrical skew (Fig. 5B). MF3 M-PC1 is negatively loaded without important variations in M-PC2 and in the XRF Zr/Al. In the XRF K+Fe+Ti/Ca+Sr, this facies shows an increasing and decreasing trend, reaching a maximum at 5.28 m depth, which corresponds with the top of the lower subdivision of the sequence (Fig. 3A).

MF3 presents a slightly different trace fossil assemblage with *Planolites, Thalassinoides*, and *Nereites*, but also with rare *Chondrites* and possible *Zoophycos,* as well as local *Mycellia* (Fig. 8C and D). A conclusive assignation of the differentiated ichnofabrics is therefore difficult.

4.2. Corsica Trough

Core PSM3-CS009 is characterised by a 22 m-thick succession of bioturbated, structureless, fine-grained sediment that includes three bioclastic coarse-grained beds at 0.65-1.35, 12.17-12.71 and 15.62-16.10 mbsf (Fig. 9A), defined as Corsica Facies 1 (CF1) (Table 3). Two different fine-grained sediments, denoted Corsica Facies 2 (CF2) and Corsica Facies 3 (CF3), can be distinguished according to the PCA and geochemical proxies. Radiocarbon dating yielded approximately the same age (~30 kyr BP; Fig. 9A) for the muddy sediment above (at 11.26 mbsf) and below (at 14.00 mbsf) the thickest CF1 sandy bed.

Corsica principal component analysis (C-PCA)

The PSM3-CS009 PCA-analysis gave two significant Principal Components (PC) in the Corsica succession (Table 2). The first two axes of the PCA yield respective variance percentages of 62% and

15%, thereby accounting for 77% of the total variability (Table 2). The main positively loaded C-PC1 elements are Al, Si, K, Fe, Mn, Rb and Zr, in contrast to the main negatively loaded Ca and Sr (Fig. 9B). The main positively loaded C-PC2 elements are Al, Si, Ca and Mn against the negatively loaded K, Fe and Br (Fig. 9C).

Ichnological analysis

Analysis of high-resolution images of the PSM3-CS009 core reveals, in general, a less abundant and diverse trace fossil assemblage than in the Mozambique core. This trace fossil assemblage mainly consists of *Planolites* and *Thalassinoides*, but *Scolicia* and *Chondrites* were also observed, along with possible *Nereites* and vertical traces. Ichnofabric features allow for identification of the three ichnofabrics (i1 to i3), but with a significant difference: i1 is clearly dominant (Fig. 10).

Corsica Facies 1: Mottled fine-grained sand

Corsica Facies 1 (CF1) (0-2.5 mbsf; Fig. 9A) consists of mottled reversely- and normally-graded decimetre-thick bed, ranging from fine-grained silt to fine-grained sand (6.1-275.4 µm). The S14 section (12.17-12.71 mbsf) includes the sandiest interval of PSM3-CS009, which consists of a 60 cm-thick bed (from fine-grained silt to fine-grained sand) with gradational top and bottom contacts (Fig. 10A and B). CF1 shows coarser bioclast lags throughout the sequence (Fig. 10A and B). The sediment is very poorly sorted (Fig. 5A) and has a trimodal to polymodal mesokurtic and platykurtic grain-size distribution, ranging between coarse to fine skew (Fig. 5B). This facies has a marked negative excursion in C-PC1 and K+Fe+Ti/Ca+Sr, and the highest fine-grained sand volume (up to 70 %) being in the core (12.59 mbsf depth in Fig. 9A). The C-PC2 shows a subtle negative loading, whereas the XRF Sr/Ca curve shows increasing and decreasing upwards trends, all of which correlate well with the grain size distribution curve (Fig. 9A).

Analysis of high-resolution images and X-Ray images of the thickest CF1 bed section (12.43-13.03 mbsf) reveals the presence of i2 and mainly i3 (Fig. 10A). Thus, coarse-grained filled *Thalassinoides*, and occasionally *Planolites*, are registered in fine-grained (i2) and coarse-grained (i3) host sediment. A significant ichnological feature consists of the well-developed *Thalassinoides* structures observed in both i2 and i3. Coarse-infilled *Thalassinoides* registered in i2 are found at 20-35 cm down from the top. Two levels of fine-grained *Thalassinoides* can be observed throughout the sequence (Fig. 10A). Ichnofabric i1 is present again at the top of the bed (0-10 cm), consisting of fine-grained sediment with *Planolites* filled by the same host sediment.

Microfacies from CF1 remain similar throughout the sequence in the different thin sections studied. CF1 thin sections present a distinctive patchy texture (Fig. 11A, B and C). Grain-supported fabric (packstone) is predominant, although areas with mud-supported textures (wackestone) are locally present. Packstone areas are enriched mainly in planktonic (20-40 %) and benthic (10-15 %) foraminifera, and in other bioclasts (10-15 %) (Fig. 12A and B). Distinctly planktonic foraminifera tests composed of hyaline calcite —with typically globular chambers— are ubiquitous. The planktonic foraminifers are of different sizes (up to 200 μm) and unevenly distributed, and the vast majority are well preserved. The benthic foraminifera are usually larger than the planktonic foraminifers (up to 500 μm) and are also well preserved. The planktonic and benthic test chambers may be filled with glauconite (5-20 %) or lack any filling (15-20 %) (Fig. 12A and B). Other bioclasts consist of thin-shelled fragmented brachiopods, molluscs and algae (Fig. 12A and B). Glauconite grains are usually authigenic (rare detrital glauconite grains can be found) and they are randomly distributed throughout the sequence presenting different degrees of maturation from brownish to greenish colours (Fig. 12A and B). Usually, the glauconite-filled foraminifers present brownish colours, whereas the solitary grains present greenish colours (Fig. 12A and B). Wackestone areas present the same composition as the packstone and usually show sub-circular patches 0.5-1 cm-thick; they develop from organic matter streaks, in turn resulting from the refilling of biogenic traces (Fig. 11B and C). Within the wackestones patches, there is a higher content in matrix and a lower content in glauconite (Fig. 12C and D). Here, empty foraminifers' tests are more abundant than those filled with glauconite (Fig. 12C and D). These areas are slightly enriched in silt-size subangular quartz grains (Fig. 12C and D).

Corsica Facies 2: Mottled fine- to coarse-grained silt

Corsica Facies 2 (CF2) is found in different intervals (0-1 mbsf; 11.20-15.58 mbsf; 16.20-17.20 mbsf; 20.20-21.15 mbsf; Fig. 9A) and consists of mottled fine- to coarse-grained silt (6.10-30.83 µm). This facies is up to 4 m-thick and shows gradational/indistinct top and bottom contacts. The sediment is very poorly sorted (Fig. 5A) and has a trimodal to polymodal mesokurtic and platykurtic grain-size distribution, with coarse and symmetrical skew (Fig. 5B). CF2 is negatively loaded in C-PC1 and has low values of K+Fe+Ti/Ca+Sr (Fig. 9A). The C-PC2 values are next to zero and the Sr/Ca curve exhibits increasing and decreasing upwards trends that are less pronounced than in CF1, and are well correlated with the grain size distribution curve (Fig. 9A).

Ichnological analysis reveals the presence of the three ichnofabrics (i1 to i3), with the dominance of i1, which is characterised by fine-grained sediment mainly with fine-grained infilled *Planolites* and *Thalassinoides*, and also some *Scolicia* and *Chondrites*. Crosscutting relationships between traces are observed. The interval of i2 (14.47-14.23 m) consists of *Planolites* and *Scolicia* filled by the fine-grained host sediment and *Thalassinoides* filled by coarse-grained sediment from above (Fig. 10C). Interval i3 (14.23-14.15 mbsf) shows coarse-grained sediment with *Thalassinoides* filled by the same host sediment (Fig. 10C).

Corsica Facies 3: Homogenous fine-grained silt

Corsica Facies 3 (CF3) is highly variable in thickness reaching up to 9.7 m (Fig. 9A), and consists of mottled fine- to medium-grained silt (5.96-11.49 µm). CF3 shows gradational/indistinct top and bottom contacts (Fig. 10D and E). The sediment is very poorly sorted (Fig. 5A) and has a trimodal to polymodal mesokurtic and platykurtic grain-size distribution, with a coarse and symmetrical skew (Fig. 5B). This facies is positively loaded in C-PC1, which shows a good correlation with the K+Fe+Ti/Ca+Sr curve (Fig. 9A). At approximately 9 m depth (Fig. 9A), this facies shows an important peak in C-PC1 and in K+Fe+Ti/Ca+Sr, which decreases upwards along a 2-m-thick interval. C-PC2 and Sr/Ca curves do not show any important variation.

CF3 shows the near exclusiveness of i1 and local presence of i2. Thus, discrete fine-grained filled traces are registered over a mottled background. The trace fossil association mainly consists of *Planolites* and *Thalassinoides*, but *Scolicia* and *Chondrites* can also be identified (10.35 and 10.80 mbsf, respectively, in Fig. 10D). These traces show a clear crosscutting relationship, with *Chondrites* overlapping the other traces. Occasionally, i1 in CF3 presents scarce traces lacking any mottled background (S10 in Fig. 10E), or the record of possible *Nereites* and vertical traces. Punctually, i2 contains coarse-grained filled *Thalassinoides* into fine-grained sediment.

6. INTERPRETATION OF SEDIMENTARY FACIES

6.1. MF1: Siliciclastic sandy contourite

Given their gradational base, the reversely- graded trend, the lack of primary sedimentary structures and the high level of mixing produced by extensive bioturbation, MF1 facies shows similarities with published examples of the sandier central interval of the standard bi-gradational sequence (Gonthier et al., 1984) or the interval C3 from Stow and Faugères (2008). The inverse relationship between sorting and grain size in this facies cross-plot (Fig. 5), which occurs approximately at 50 to 60 µm, suggests an increase in bedload transport and the onset of significant winnowing (Brackenridge et al., 2018; Yu et al., 2020) in sandy contourites. This also agrees with the presence of fine-grained sandy current ripples at the present-day seafloor (Fig. 2B), thus indicating a predominant deposition from bedload transport. However, no sedimentary structures were found in this facies. Extensive bioturbation resulted in the mixing of sediment, making it very poorly to poorly sorted, with irregular patches of matrix-rich and matrix-poor sediment observed at core and thin-section scale at the base of the sequence (Fig. 6A and B). This texture can be interpreted as relics of primary sedimentary structures of well- and less-sorted laminae that were severely disturbed by bioturbation (de Castro et al., 2020a, b) and are probably related to the presence of current ripples.

The smaller-scale internal grading is also observed in the ichnological features, including the distribution of ichnotaxa, the type of infilling in the trace fossil assemblages, and the differentiated ichnofabrics (i1 to i3) (Fig. 4). A remarkable feature of these ichnofabrics is the infilling material of the included trace fossils: from those with traces infilled with fine-grained material (i1), to those with traces infilled with coarse-grained material registered within fine- (i2) or coarse-grained (i3) host sediment. In the absence of signals evidencing changes in deep-sea benthic environmental parameters, such as oxygen or nutrient availability, each ichnofabric can be related to different depositional conditions, mainly involving hydrodynamic energy, rate of sedimentation, erosion and continuity in deposition (Ekdale et al., 2012; Rodríguez-Tovar and Dorador, 2014; Alonso et al., 2016; Rodríguez-Tovar et al., 2019). Thus, the record of i1 characterised by a mottled background and fine-grained infilled traces would mark low and continuous deposition of fine-grained sediment by low-energy depositional processes, without disruption at any scale, in a well-oxygenated seafloor environment (Rodríguez-Tovar and Dorador, 2014). The successive record of i2 reveals similar depositional processes, but a potential increase in the rate of sedimentation that impeded a well-developed mottled background in the fine-grained host sediment. The sequence of ichnofabrics i2 to i3 reveals a significant change in depositional conditions. The record of coarse-grained filled *Thalassinoides* and *Planolites* inside i2 points to a decrease in sedimentation or even erosion before the development of i3, and an increase in substrate consistency. The record of coarse-grained filled *Thalassinoides* and *Planolites* could reveal minor-scale erosion phases with no record of any evident erosional surfaces (de Castro et al., 2020a, b). Finally, a continuous deposition in a higher energy context can be interpreted for i3, in light of the presence of intensive coarse-grained infilled bioturbation (de Castro et al., 2020a, b). The next i1, could be associated, again, with the erosive phases; for example, the presence of well-developed *Thalassinoides* at 70 cm depth below an irregular surface between i3 and i1 may be linked to the presence of an omission surface (Fig. 4A and B), according to the relationship between these ichnogenera a substrate consistency (Rodríguez-

Tovar et al., 2017). In sum, the identified ichnofabrics evidence sedimentary interruptions and erosional processes, throughout of MF1.

The positive M-PC1 loading indicates a high concentration of Si, Ca, Sr and Zr in the fine-grained sands (Fig. 3B), which is consistent with the main microfacies components (quartz grains, foraminifers, other bioclasts and heavy minerals; Table 4). When the intensity of the bottom current is enhanced, the coarser sediment particles (quartz, foraminifers, other bioclasts and heavy minerals) start to concentrate, resulting in a relative increase of Si, Ca, Sr and Zr in the sediment (positively loaded M-PC1; Fig. 3B). The finer-grained detritics (negative loaded M-PC1) are winnowed away from 2 mbsf until the present-day on periods of relatively low sedimentation rates (about 30 cm/kyr Fig. 3A). This interpretation agrees with previous models for sandy contourites, where coarser beds are often mixed by bioturbation hosted in sediments with relatively rich coarser siliciclastic and carbonate particles (Gonthier et al., 1984; Mulder et al., 2013; Stow et al., 2013a). In addition, the fact that peaks in Zr/Ti indicate higher heavy mineral concentrations evokes a heightened bottom current influence (Bahr et al., 2014).

6.2. MF2: Siliciclastic muddy contourite

The matrix supported texture, the absence of primary sedimentary structures, and the fine-grained nature of the sediment suggest that MF2 resulted from deposition by lateral advection of fine-grained terrigenous particles. Low excursions in the Zr/Ti curve and nearly zero values in M-PC1 indicate a low-energy regime with high sedimentation rates (about 95 cm/kyr; Fig. 3A), in agreement with the symmetrical skewness values (Fig. 5B). These fine-grained sediments could be mistaken for hemipelagic deposits; however, their geochemical signal provides some insight about their origin. As proposed by de Castro et al. (2020b), when bottom current reworking or gravity-driven flows are not dominant sedimentary processes, the marine productivity and continental input constitute the main mechanisms of sedimentation, which will be reflected in a high excursion of the first principal component. A pure hemipelagic deposit should be high-negatively loaded in M-PC1, but the close to zero values in M-PC1 suggest that the hemipelagic signal is slightly overprinted and, thus, it implies a slight reworking in the sediment. The dominant presence of detrital grains (quartz) and high values in K+Fe+Ti/Ca+Sr would mean that these deposits could generally be related to river plumes, changes in productivity and/or fluctuations in the hydrodynamic regime (e.g., Arz et al., 1999; Hodell et al., 2013).

Ichnological information reveals changes in depositional and ecological conditions with respect to MF1. The abundance of *Palaeophycus*, in some cases in dense horizons (Fig. 4E and F), might indicate some punctual, localised, rapid nutrients input, meaning an increased sedimentation rate; the rapid burial of organic matter at the seafloor prevents its oxidation, leaving it available for shallow/middle tier organisms as *Palaeophycus* tracemakers (Dorador et al., 2019). Because MOZ4-CSF19 is located in the upper slope, in the distal part of a contouritic terrace under the influence of the sediment supply by the Zambezi river and the MC current, this facies is related to high sedimentation rates flood events that were transported along the outer shelf and upper slope by the MC current, hence interpreted as muddy contourites.

6.3. MF3: Muddy hyperpycnite

MF3 is interpreted as deposits from waning, dilute, turbulent flow. The lower subdivision (538-583 cm) is interpreted as the result of a distal waning flow by turbulent transport. This muddy facies has been sourced via river input, based on the positive excursions peaks in K+Fe+Ti/Ca+Sr and the irrelevant reworking (negative M-PC1; Fig. 3). The absence of sand in this facies can be explained by: (i) the dominance of mud-grade sediment delivered to the basin (river-floods); and (ii) a distal position relative to the feeder system. MF3 may have originated with the plunging of sustained sediment-laden turbulent flows (hyperpycnal flows), the suspended load being mainly composed of a clay-silt fraction (e.g., Mulder and Alexander, 2001; Mulder et al., 2003; Zavala et al., 2011, Zavala, 2020). As these flows can combine suspension fallout and traction, sedimentary structures may form, as observed in the upper part of the sequence (Fig. 8D), which represent the waning part of the flood event (Mulder et al., 2001). MF3 could correspond to a wetter event during late Bølling-Allerød (aprox. 13-14 kyr BP), while precipitation and river discharges increased at the onset of East African Humid Period (Romahn et al., 2015).

The fact that MF3 has a different trace fossil assemblage than MF1 and MF2 supports a distinct depositional and ecological context. The record of *Zoophycos* and the presence of *Mycellia* could be related to distal and deeper environments likely involving low bottom-water oxygen levels, increased of sediment load (in agreement with high sedimentation rates about 110 cm/kyr; Fig. 3A) and low-energy conditions. Amelioration of sea-bottom conditions, involving nutrient availability and oxygenation, led to an increase in trace fossil diversity and the occurrence of *Thalassinoides* and *Planolites* at the top of MF3, gradationally evolving to hemipelagites (MF2). This transition represents the transition from the late Bølling-Allerød wet period to the Younger Dryas drier period with the progressive reduction of sediment fluxes from Zambezi (Romahn et al., 2015).

6.4. CF1: Bioclastic sandy contourite

CF1 is principally made up of well-preserved foraminifers, which constitute the sand-sized particles, occasionally together with shallow-water materials such as benthic foraminifers and other bioclasts. It is best interpreted as a bioclastic (up to medium-grained) sandy contourite that can be related to the central interval of the standard sequence of facies (interval C3) defined by Gonthier et al. (1984) and Stow and Faugères (2008) for contourites, in a context of increasing and decreasing bottom-current velocities, respectively. This is likewise observed in the bi-gradational negatively loaded C-PC1 at these intervals, which represents the accumulation of carbonates with respect to the terrigenous fraction (Fig. 9A). Enhanced Sr may indicate the presence of high-Sr aragonite, which usually requires a shallow-water source (Thomson et al., 2004; Rothwell et al., 2006). Biogenic aragonite often contains much more Sr than biogenic calcite in foraminifers (Thomson et al., 2004). Hence, the Sr/Ca proxy may reflect an enrichment in shallow-marine bioclasts over foraminifers (Table 4, Fig. 12).

Ichnological features are largely similar to those of MF1, noteworthy differences being the absence of i1 and the well-developed *Thalassinoides* traces in CF1. As in MF1, the sequence of ichnofabrics i2 to i3 reveals a significant change in depositional conditions; the record of coarse-grained filled *Thalassinoides* and *Planolites* into i2 points to a decrease in the sedimentation rate or even erosion before the development of i3, increasing the substrate consistency. In the case of CF1, the better development of *Thalassinoides* suggests a greater increase in substrate consistency.

Microfacies also support the interpretation of the C-PC1; the source area of the calcareous contourites could be attributed to a mix of shallow-marine and deep-water pelagic environments. The enrichment of foraminifers in contourite sands may reflect different depositional processes: i) selective deposition of particles released from the nepheloid layer on the basis of settling velocity through the boundary layer (McCave and Hall, 2006; McCave, 2008), or ii) current reworking and redistribution, close to the critical shear stress threshold (Cooke et al., 2004; Mulder et al., 2019; Hüneke et al., 2020). The selective winnowing of carbonate mud is not held to be an important bottom-current sorting process, as carbonate muds behave cohesively and undergo particle aggregation (Winterwerp and van Kesteren, 2004; McCave, 2008). The presence of empty and glauconite-filled planktonic tests moreover implies a mixing of foraminifers by means of settling throughout the water column, and reworking and winnowing of previous hemipelagic deposits, respectively. The glauconitisation inside foraminifers has been previously described as a common process at the water/sediment interface in environments affected by bottom currents (Giresse, 2008; Tallobre et al., 2019).

6.5. CF2: Bioclastic muddy contourite

The generally homogeneous and highly bioturbated sediments —often with an indistinct mottled appearance (as described by Gonthier et al., 1984; Stow and Faugères, 2008)— and the fine-grained and symmetrical skewness values suggest that CF2 resulted from deposition of fine sediment directly from suspension through a weak laminar boundary layer. This facies presents geochemical characteristics similar to bioclastic sandy contourites (CF1), with a high negatively loaded PC1 and low excursions of K+Fe+Ti/Ca+Sr implying an enrichment of foraminifers and other bioclasts in a finer-grained fraction. As in CF1, the enrichment of foraminifers can be related to reworking and winnowing by weak bottom currents. Thus, these facies are interpreted as muddy contourites according to Gonthier et al. (1984) and Stow and Faugères (2008).

Ichnological information, with the successive record of i1, i2, and i3, is in agreement with the interpretation of muddy contourites. The record of i1, characterised by a mottled background and fine-grained infilled traces, suggests low and continuous deposition of fine-grained sediment by low-energy depositional processes, without disruption at any scale, allowing for well-developed tracemaker community as indicated by crosscutting relationships. The successive record of i2 shows that similar depositional processes governed the deposition of fine-grained sediment, given the similar fine-grained trace fossil assemblage including *Planolites* and *Scolicia*. The sequence of ichnofabrics i2 to i3 reveals a decrease in sedimentation rate or even erosion before the development of i3, meaning greater substrate consistency, and leading to the record of coarse-grained filled *Thalassinoides* within i2. As in Mozambique facies, the extended record of coarse-grained *Thalassinoides* into i2, could signal minor-scale erosional phases that did not leave any evident erosional surfaces.

6.6. CF3: Hemipelagite

The visual discrimination between CF2 and CF3 is difficult at core-scale. CF3 usually consists of indistinct beds, typically grading into CF2. However, their geochemical signals show different trends. The high positively loaded C-PC1 and high excursions in K+Fe+Ti/Ca+Sr suggest that this facies is made up of fine-grained aluminosilicates. Therefore, this facies is interpreted as hemipelagic depositional suspension fallout and lateral advection of fine-grained terrigenous particles (Hesse, 1975; O'Brien et al., 1980). This interpretation is supported by the symmetrical skewness values, which are typical of hemipelagic deposits (Brackenridge et al., 2018; de Castro et al., 2020b). When sediments are not subjected to currents, a small proportion of pelagic carbonate is deposited, hence high K+Fe+Ti/Ca+Sr. The occurrence of a distinct peak in detrital input (at 9 mbsf; Figs. 9A and 10E) supports that the hemipelagic deposition would have been subjected to terrigenous sediment suspension linked to a distal turbidite currents from the nearby Golo turbidite system (Sweet et al., 2020).

This interpretation is supported by the ichnological analysis. i1 is consistent with continuous, fine-grained deposition. A low rate of sedimentation and low energy conditions facilitate a well-developed tracemarker community and the record of crosscutting relationships. In this favourable general context for the macrobenthic tracemaker community, punctual variations in paleoenvironmental conditions can be envisaged. Thus, the record of *Scolicia* and *Nereites* could be associated with locally higher concentrations of benthic food, and the presence of vertical traces or the absence of discrete traces might indicate greater sedimentation rates. This supports the notion that hemipelagic sedimentation can be promptly favoured to very diluted turbidity flows. The fine-grained sediment carried downslope by turbidity currents on the opposite side of the basin is retransported in suspension by oceanic gyres to the location of the core analysed in our study and in part settles as hemipelagic sediment (Miramontes et al., 2016, 2019)

7. DISCUSSION

7.1. Winnowing and reworking proxies in siliciclastic and bioclastic sandy contourites

The use of PCA score plots and loading plots constitutes a useful and complementary tool to discern multi-variable elemental changes related to different depositional conditions in a wide variety of sedimentary environments (Barbera et al., 2009; Margalef et al., 2013; Flood et al., 2015, 2018; López Pérez et al., 2019). Applied to contouritic sedimentary environments, this method links the distinctive geochemical element associations to the interplay of diverse sedimentary processes and to the hydrodynamic energy tied to bottom current activity (de Castro et al., 2020b). Contourite sedimentation is influenced by the interplay of different deep-water processes, such as: i) settling of biogenic particles mixed with fine-grained terrigenous sediment (hemipelagic sedimentation), ii) reworking and winnowing by deep-water bottom currents (sensu Shanmugam, 2008), iii) gravity flows of coarse- and fine-grained sediments, and iv) bioturbation.

In most sedimentary environments, the first PC tends to give a relatively high variance (>50%) and is commonly used as a measure of carbonate (marine productivity) versus terrigenous sediment input, as suggested by previous studies of deep-marine systems (Bahr et al., 2014; van den Berg et al., 2018; de Castro et al., 2020b). However, the interpretation can differ for other sedimentary systems. It is therefore crucial to undertake complementary sedimentary analysis, for instance of sedimentary texture, microfacies, ichnological information and dating. Sound knowledge of the local sedimentary settling (based on seismic or multibeam echosounder data set), is needed to arrive at a robust interpretation. This first component represents the dominant pattern in the element matrix in terms of a complementary set of score and loading plots, as seen in the Mozambique and Corsica datasets (52% and 62%, respectively; Figs. 3 and 9). However, the geochemical signal of winnowing and reworking by bottom currents is different for siliciclastic and bioclastic contouritic sands.

From a compositional point of view, M-PC1 is characterised by an enrichment of Si, Ca, Sr and Zr, with a diminution of Al, K and Fe. Siliciclastic contouritic sands (MF1) show a positively loaded M-PC1. In thin sections, this facies is made up mainly of quartz grains (Si), foraminifers and other bioclasts (Ca and Sr), and heavy minerals (Zr). It lacks matrix, in agreement with the negatively loaded Al, K and Fe— elements which are typically associated with detrital clays and oxides. Therefore, M-PC1 cannot be interpreted as marine productivity vs. terrigenous sediment input. The contourite terrace on the upper slope of Mozambique Channel, where MOZ4-CSF19 is located, is an area under high-energetic conditions (Miramontes et al., 2016) where different bottom currents (sensu Shanmugam, 2008) can modify the standard geochemical signal of deep-marine environments (marine productivity vs. terrigenous sediment input; Bahr et al., 2014; van der Berg et al., 2018).

Examination of the M-PC1 against the M-PC2 biplot in the Mozambique dataset (Fig. 13A) reveals that sandy contourites (MF1) are positively loaded in M-PC1 (winnowed and reworked), but they may be either positively or negatively loaded in M-PC2, hence making a different sediment source (Fig. 13A). A positive M-PC2 in the Mozambique sandy contourites (sediment source A; top-right quadrant in Fig. 13A) implies predominantly fine-grained terrigenous input (Ti, Rb, K, Si and Zr) synchronous with vigorous bottom currents (positively loaded M-PC1 and high excursions in Ln Zr/Ti). This data cloud corresponds to the base of the sequence (0.77-2.1 mbsf; Fig. 3C) and correlates with a severe reduction in river runoff, meaning arid conditions in East Africa (Romahn et al., 2015; van der Lubbe et al., 2016; Caley et al., 2018). Enrichments in Ti (positively loaded in M-PC2) help trace density differences in siliciclastic materials, especially to those deriving from aeolian sources (Chen et al., 2013; Martinez-Ruiz et al., 2015). Ti has been used (along with Zr) to track changes in the supply of wind-blown dust because of enhanced concentrations of aeolian particles in marine sediments (Martinez-Ruiz et al., 2015). Therefore, a positive load in M-PC2 could indicate an aeolian sediment source.

In contrast, the data cloud from the top of the sequence (0-0.77 mbsf; Fig. 3C) is characterised by positive M-PC1 and negative M-PC2 (Fig. 13A), corresponding to the sedimentary condensation of Si and Zr along with biogenic sediments (Ca and Sr), as well as a total depletion of the fine-grained terrigenous fraction (Ti, Rb and K) (Fig. 13A). A negatively loaded M-PC2 would correspond to an enrichment in Al and Fe, linked to fluvial sediment input, as represented by Fe-based proxies around the western and eastern Africa continental margins (Adegbie et al., 2003; Dickson et al., 2010; Revel et al., 2015; Ziegler et al., 2013; Rohling et al., 2014; Caley et al., 2018). This indicates that MF1 was subjected to different sediment sources during its deposition. However, distinguishing between aeolian and fluvial sources of certain terrigenous elements is challenging; both input sources may supply the same detrital minerals, they could have similar elemental ratios. The detailed provenance of these different terrigenous sources therefore lies beyond the scope of this study.

The top of the MF1 represents the establishment of the present interglacial circulation along the outer shelf and upper slope. The retreat of the sediment source to the present delta and shoreline led the fine-grained sediments to be deflected to the north of the margin (Schulz et al., 2011). A decrease in the distal fine-grained sediment load, plus the establishment of the present interglacial circulation, favoured the deposition of reworked coarser-grained sediments.

Notwithstanding, the winnowing and reworking evidenced in the Corsica dataset differ from the processes recorded in Mozambique. Corsica bioclastic sandy contourites are mostly negatively loaded in terrigenous-sourced elements (C-PC1; Si, Al, Mn, Zr, Rb, Fe, K and Br; Fig. 9), indicating a relative enrichment in carbonates (Ca and Sr). The sediment is thus depleted of terrigenous-sourced elements, which are mainly present in the fine-grained fraction, as observed in the predominantly bioclast-rich packstone texture (Figs. 11 and 12). Moreover, bioclastic-sandy contourites can be positively (top-left quadrant in Fig. 13B) or negatively (bottom-left quadrant in Fig. 13B) loaded in C-PC2. A negatively loaded C-PC2 indicates an enrichment in K and Fe, especially in the studied bi-gradational sequence at 13 mbsf (Fig. 9), and could mark the abundance of glauconite in the sediment (Fig. 12A, B and D). CF1 contains abundant bioclasts and authigenic and detritic glauconite grains, including a mixture of empty- and glauconite-filled-foraminifer tests. Glauconitisation occurs frequently at the water/sediment interface, especially from the outer shelf to the upper slope, with low sedimentation rates, to promoting the incorporation of Fe and subsequently K (Giresse and Wiewióra, 2001; Giresse, 2008; López-Quirós et al., 2019). The predominantly rounded shape of the grains points to foraminifers as a widespread host for glauconite growth (Hesse and Schacht, 2011). Once deposited on the seafloor, foraminifer tests are subjected to long periods of cation exchange across the seawater/sediment interface, thereby promoting glauconite growth inside the chambers (Giresse and Wiewióra, 2001; Giresse, 2008; López-Quirós et al., 2019; Tallobre et al., 2019).

7.2. Hydrodynamic depositional conditions for siliciclastic and bioclastic contouritic sands

Sediment properties —mean grain size, sorting, particle density, particle shape and settling velocity— are, together with the dynamic forces of the fluid, the most important features controlling depositional processes (e.g., Krumbein, 1943; Menard, 1950; Simons et al., 1961). The link between contourite grain size, sorting and bottom-current speed has long been recognised (Ledbetter and

Ellwood, 1980; McCave, 1984, 2008) and is proposed to be the principal factor controlling the standard bi-gradational sequence model for contourites (Gonthier et al., 1984; Stow and Faugères, 2008). Both Mozambique (siliciclastic) and Corsica (bioclastic) contourite sequences show clearly trend towards grain-support and low-mud content as a result of sorting during bottom-current-induced sediment transport and deposition. Particularly significant is the finding that the Mozambique siliciclastic sands are better sorted overall than the Corsica bioclastic sands (Fig. 5A). In general, the bioclastic data cloud trend is clearly displaced upwards, towards to poorer sorting; this appears to be an inherent feature, most plausibly explained by the predominately polymodal and platykurtic grain size distribution and the presence of different-shaped skeletal grains (Figs. 11 and 12). By contrast, the siliciclastic sand trend is displaced downwards, towards a better sorted, unimodal and leptokurtic grain size distribution (Fig. 5A and B), possibly indicating an increase of bedload transport and reworking at high current speeds (Brackenridge et al., 2018). This means that the more rounded siliciclastic contouritic sands can achieve better sorting than the irregularly shaped bioclastic contourite sands. It is also important to point out, however, that the siliciclastic and bioclastic particle groups were not exposed to the same sorting process. The difference in sorting should be regarded as a systematic feature evidencing hydraulically different states or processes: winnowing and reworking.

Winnowing denotes the removal of fine-grained material from a coarser sediment by flowing water. It implies a synchronous interaction between sediment input and bottom currents, favouring the depletion of the fine-grained fraction of the sediment (typically associated with clays/oxides and elements such as Al, K, Ti, Fe and Rb; Fig. 14A). Only the larger, denser and more resistant components (quartz grains, skeletal particles and heavy minerals) remain in place, as observed in siliciclastic and bioclastic contouritic sands (Figs. 3 and 9).

If bottom currents are vigorous and persistent over longer periods of time, the sediment on the seafloor may undergo reworking (Fig. 14B). Sediment reworking is the post-depositional erosion and redeposition of pre-existing sediments favouring the condensation of a particular sediment composition (Föllmi, 2016). Sedimentary condensation may the result not only from low sedimentation supply or a hydrodynamically active depositional regime, in which winnowing, sediment accumulation, erosion, reworking and bypass could alternate according to changes in the intensity of currents (Föllmi, 2016). Sediment reworking may or may not include a component of lateral displacement —sediments can be reworked yet remain more or less at the place where they were originally deposited (e.g., bottom current reworked sands; Shanmugam et al., 1993; de Castro et al., 2020a) or else be transported over longer distances by bedload transport without preserving signs of other depositional processes (sandy contourites). Sediment reworking during condensation is mainly a physical process, although biological processes such as bioturbation also assist (Föllmi, 2016), as observed at both locations (Fig. 14B).

However, because bioclastic particles show a large diversity of shapes and bulk-densities compared to the sub-rounded particles found in most detrital sands, they reduce the prediction of transport rates in energy-based transport models (Prager et al., 1996; Smith and Cheung, 2005). This variability makes it difficult to directly relate grain size to current strength in bioclastic sands (McCave and Hall, 2006). For example, disaggregated bivalves with concave blades react to current differently, depending on which side is exposed to the current (Eberli and Betzler, 2019); in addition, owing to their lower density, they require a lower shear stress to initiate transport than other carbonate particles (Prager et al., 1996). In turn, the very flat shape of the bioclastic particles, resulting in low-settling velocity values, also promotes stability and bed armouring when arranged on a sediment surface, so that higher bottom current velocities are needed to rework this type of sediment. Since Corsica bioclastic sands are located in a quieter environment (mounded drift) and Mozambique siliciclastic sands in a higher energy environment (contourite terrace), it is most likely that Corsica bioclastic sands were subjected mainly to winnowing but also to reworking. The winnowing of shallow-marine sediment input generated a deposit enriched in a relatively well-preserved mixture of fauna from different palaeodepths (planktonic and benthic foraminifers and other bioclast fragments) showing minimal thickness. The mixture of empty- and glauconite-filled foraminifer tests suggests seafloor reworking and limited clastic sediment input despite current velocities powerful enough to resuspend previously deposited foraminifers (glauconite-filled foraminifer tests; Fig. 14B). "Autochthonous" foraminifers (especially planktonic empty-foraminifer tests) have the erodibility of very coarse silt. They have the settling velocity of very fine sand, however; they are not transported over great distances, being largely confined to bedload (McCave, 2008), and mixed with the glauconite-filled-foraminifer tests.

Because fine-grained sediments —even carbonate muds— behave cohesively and are subject to particle aggregation (Winterwerp and van Kesteren, 2004; McCave, 2008), bottom currents between 20 to 30 cm/s are needed in order to remove clay and carbonate muds, thereby giving way to winnowed and reworked sandy beds (McCave and Hall, 2006). It is important to underline that winnowing and reworking would nonetheless depend on the state of consolidation of the sediment, its composition and its content in mud. The diagram of Press and Siever (1986) shows that the threshold motion velocity in unconsolidated mud is between 2 and 5 cm/s (McCave and Hall, 2006; McCave et al., 2017).

7.3. The balance for contourite formation: sediment input vs. bottom-current intensity

Contourites develop when the energy of bottom currents is high enough to: i) affect vertical settling of pelagic and hemipelagic sediments; ii) affect gravity flows, and/or iii) rework the sediments on the seafloor (Rebesco et al., 2014 and references therein). In areas with higher direct sediment supply and faster sediment rates, the energy of bottom currents does not suffice to rework the original deposits (de Castro et al., 2020b). These conditions could correspond to areas closer to sediment supply, especially during sea-level lowstands (e.g., by an adjacent large river, in zones having active turbidite flows, or next to the upper slope along some continental margins). In addition, sediment accumulation rates often oscillate due to changes in sea-level and in climatic conditions (e.g., Haq et al., 1993; Catuneanu, 2006). Takashimizu et al. (2016) proposed three different age models for the formation of the bi-gradational sequences (see explanation in Fig. 15). For these reasons, the Mozambique and Corsica systems are especially sensitive to changes in sediment supply, and the formation of the bi-gradational sequence could differ for siliciclastic and bioclastic contourite sands.

7.3.1. Siliciclastic contouritic sands

In Mozambique, radiocarbon dates obtained from planktonic foraminifera show a continuous increase in age down the core, even in the bi-gradational sequence, from 9,135 cal kyr BP to 2,761 cal kyr BP (i.e., $\Delta T \neq 0$), suggesting relatively continuous deposition with accumulation rates about 30 cm/kyr (Fig. 3A and Table 2). This evokes Models 1 and 2 of Takashimizu et al. (2016) (Fig. 15). The three different ichnofabric distributions would suggest more variability than those models, with shorter time changes in hydrodynamic conditions, shorter term and higher sedimentation rates with lower bioturbation rates, and flow variability during the deposition of the siliciclastic sequence (MF1). Such variability may be linked to intermittent interactions between bottom currents and sediment supply, hence different environmental conditions for tracemakers (Rodríguez-Tovar et al., 2019a, b). However, these changes —interpreted in view of ichnological features (see Fig. 16 for explanation)— are punctual, relatively rapid, bearing little influence on the comparatively long in duration of the entire sequence seen in the ancient and modern record (Rodríguez-Tovar et al., 2019a, b; de Castro et al., 2020a, b; Hüneke et al., 2020). Unfortunately, all possible dating methods (applicable to this sites) do not allow researchers to 1) building a robust high-resolution age model; or 2) to identify with precision the presence and duration of such sediment hiatuses.

The muddy contourite facies (MF2) developed during the post-glacial sea-level rise, under sedimentation rates of about 100 cm/kyr (Fig. 3A). Such high sedimentation rates suggest the direct input of sediments from the adjacent Zambezi river to the study area (Schulz et al., 2011). During sea-level highstands offshore currents transport a large part of the sediments from the Zambezi river northwards, leaving a reduced amount accumulated on the slope in the study area (Schulz et al., 2011), which may explain the reduced accumulation rates (about 30 cm/kyr) of the siliciclastic sequence (Fig. 3B). The considerable distance of the sediment source, the reduction of sediment input, and enhanced bottom currents during sea-level highstands would contribute to the winnowing and reworking of previously deposited sediments.

7.3.2. Bioclastic contouritic sands

Mozambique siliciclastic sands are continuously supplied from the adjacent continent and shelf. Yet in Corsica there is no direct source of siliciclastic sand from the adjacent continent and shelf (Fig. 1; Schulz et al., 2011; Miramontes et al., 2016). Therefore, a higher percent of shallow-marine bioclastic sands is transported onto the slope, then mixed with autochthonous biogenic particles, most likely during isolated episodes of transport and winnowing of sediments from the shelf and the shelf edge. Based on the age model of the Corsica contouritic sands, the top and the base of the sandy interval are of similar age (29,507±408 cal yr BP and 30,368±636 cal yr BP; Fig. 9A), and therefore ΔT ~ 0 (Fig. 15). This model suggests a more rapid deposition for the bioclastic contourite sands, possibly related to gravity-driven processes. In the absence of high-resolution radiocarbon ages throughout the bioclastic bi-gradational sequence, including the muddier intervals, ichnological data provide useful complementary information regarding the relative duration of the sandy interval deposition. The sequence of ichnofabrics i2 to i3 in Corsica's bi-gradational sequence marks a significant change in depositional conditions throughout the sequence; the record of coarse-grained-filled *Thalassinoides* and *Planolites* within i2 lead us to surmise as a decrease in sedimentation rates or even erosion before the development of i3, with increased substrate consistency (Fig. 16). Such intermittent depositional conditions are similar to those observed in Mozambique siliciclastic sands, discarding a fast event as the trigger of its formation (Fig. 16). Corsica's bioclastic sands could therefore represent the small-scale cyclicity of contourite deposition, as recorded in the Gulf of Cadiz (Brackenridge et al., 2018; de Castro 2020a, b), most likely related to short-term (possibly multicentennial scale) fluctuations of the bottom currents as observed in the Capo Vaticano upper slope in the Mediterranean Sea (Martorelli et al., 2020). The duration of these short-term fluctuations is within the error limits of the radiocarbon ages measured on the core of Corsica, so they could not be unequivocally identified (Fig. 9A). Given this situation, model 2 of Takashimizu et al. (2016) would fit the Corsica bi-gradational sequence better. As in the case of Mozambique, the bi-gradational sequence in Corsica developed during a period of active bottom currents and isolated episodes of sediment input (Calvès et al., 2013; Miramontes et al., 2016). Considering the present-day hydrological structure in the Corsica Trough, an active bottom current period might signal intensified Levantine Intermediate Water (LIW) inflow and bottom water oxygenation during stadials MIS 3 and MIS 2 (Toucanne et al., 2012; Minto'o et al., 2015), followed by weaker LIW ventilation during the Holocene.

Chabaud et al. (2016) demonstrated that the overall bi-gradational grain-size trend in the carbonate contourites can be interpreted along the lines of siliciclastic sequences described by Gonthier et al. (1984) — an acceleration followed by a deceleration of bottom currents over time. However, the processes involved in the bioclastic sandy contourite sandy interval (CF1) are quite different from those of the siliciclastic one (MF1). Mulder et al. (2019) proposed that the bioclastic central interval corresponds to currents with enhanced velocity, increasing fine-grained particle winnowing under very low sedimentation rates (<3 cm/kyr) and reworking of the sediments. The skeletal particles of Corsica's bioclastic sands range from round (foraminifers), rod (echinoid spines), and blade (bivalves), to plate-shaped particles (echinoid plates). It can be expected that the bulk of the material of each shape group would be transported at a different average height above the seafloor in the bottom boundary layer (Flemming, 2016). The fact that we lack bottom current velocities, the threshold of motion, and settling velocity parameters, impedes attempts to unravel the hydrodynamic conditions of deposition of these contouritic sands. Still, we can anticipate a higher drag coefficient —and higher shear stress— in flat-shaped bioclasts (as bivalves or coralline algae) than in rounded foraminifers during the post-depositional reworking. At the same bottom current speed, foraminifers would be transported more easily in suspension, and most of the bioclasts would remain near the bottom bed. In other words, in an active bottom current setting, a bioclastic-rich sediment input is prone to be exposed during longer periods to the bottom currents. But once it is deposited, more vigorous bottom currents are needed for the reworking of bioclastic particles. As the Corsica mounded plastered drift represents a low-energy environment, it is most likely that the C3 interval of the bi-gradational sequence marks the interaction of bioclastic-rich sediment input and bottom currents for a short period of time, in agreement with a previously mentioned short multicentennial cycles. During the synchronous interaction between the bottom currents and the gravity-driven flow, the fine-grained suspended load is winnowed downstream from the depositional site, as observed in flume experiments (Miramontes et al., 2020), and most of the coarser particles are deposited in the drift as sediment lags.

7.4. Bi-gradational sequence: contourite terrace vs. plastered drift

The standard bi-gradational sequence defined by Gonthier et al. (1984) has been widely used as a diagnostic criterion for modern and ancient bottom-current activity and contourite mounded drift deposits in deep-marine environments in recent years (Duan et al., 1990; Balaky and Tamar-Agh, 2017; Capella et al., 2017; Li et al., 2019; Rodríguez-Tovar et al., 2019; de Castro et al., 2020b; Hüneke et al., 2020; Zhang et al., 2020). This sequence consists of five intervals (C1-C5) related to a flow with a waning-waxing trend, giving rise to the typical superposition of coarsening-upward (reversely graded) and fining-upward (normally graded) sequences (Gonthier et al., 1984). Recently, de Castro et al. (2020b) proposed the genesis of bi-gradational sequences with precessional-driven changes in bottom current speed coetaneous with higher sediment input in the Gulf of Cadiz. Stow and Faugères (2008) proposed that incomplete bi-gradational sequences are also common in contourite drifts, suggesting the terms “base-cut” (intervals C3-C5), “top-cut” (intervals C1-C3) or “base and top cut” (interval C3). These complete and incomplete sequences were identified during the IODP 339 expedition in the Gulf of Cadiz (Stow et al., 2013; Hernández-Molina et al., 2014, 2016). Alonso et al. (2016) and de Castro et al. (2020a) described the base-cut contourite sequences in areas near contourite channels and moats, that is, in a channel-drift transition zone. De Castro et al. (2020a) related those incomplete sequences to the sedimentary input by dilute turbiditic flows, later reworked by the bottom currents. However, the genesis of the top-cut contourite sequences is still poorly understood.

Mozambique sandy contourites (MF1) have developed since approximately 9,135±152 kyr BP until the present day; indeed, current ripples can be found in the present-day seafloor on a contourite terrace (Fig. 2A and B). Unlike Corsica sandy contourites (CF1), which present the full bi-gradational sequence, the Mozambique sandy contourite (MF1) serves as a good example of a top-cut contourite sequence (Fig. 3A) formed under sedimentation rates of approximately 30 cm/kyr.

During the late Holocene, the sedimentation rate along the Mozambique contourite terrace in the upper slope was very low, owing to a combination of circumstances: i) the general sea-level high stand; ii) less sediment supply in the distal part of the studied terrace because the Zambezi river was mainly transported northward by longshore currents (Schulz et al., 2011); and iii) the Mozambique current (MC) actively flowed along the shelf break and the upper slope (Fig. 17A). Given the combination of these processes, the contourite terrace was and is still affected by vigorous bottom currents which winnow, rework and predominantly erode previously deposited sediments (Thiéblemont et al., 2019; Miramontes et al., 2020b).

We therefore propose that one setting for the formation of top-cut contourite sequences is the distal zone of contourite terraces due to higher bottom current energy conditions than in a contourite drift. Thiéblemont et al. (2019) shows clear evidence for high current velocities influencing contourite terraces (> 25 cm/s). This model agrees with the sedimentary model proposed by Viana and Faugères (1998) offshore Brazil, where a sequence of facies similar to those Mozambique was described. From the viewpoint of these authors, sandier and dominant siliciclastic sediment is supplied from the outer shelf to the upper slope terraces during the transgression, then later reworked by the Brazil Current. In their model, the carbonate accumulation would occur during relative sea-level falls, before subaerial exposure of the shelf, as observed also in the Bahamas Bank (Mulder et al., 2019) and in the example in of Corsica studied in this work (Fig. 17B).

8. CONCLUSIONS

Based on the comparison between two different contourite depositional systems located in the upper-middle continental slope of the Mozambican margin (SW Indian Ocean) and the Corsica Trough (northern Tyrrhenian Sea), that are characterised by the presence of siliciclastic and bioclastic sandy contouritic layers respectively, we draw the following conclusions:

- The interaction between sediment supply and bottom current activity is reflected in the Principial Component Analysis (PCA). Reworking proxies are represented differently depending on the nature of the sediment. In siliciclastic contourite sands, the reworking is marked by an enrichment of quartz (Si), large bioclastic-skeletal grains (Ca and Sr), and heavy minerals (Zr), and a diminution of the terrigenous elements (Fe, K, Al, Ti and Rb) due to winnowing and reworking. In bioclastic contourite sands, winnowing and reworking is mainly represented by an enrichment of coarse-grained bioclastic particles (Ca and Sr) and diminution of the terrigenous elements (Fe, K, Al, Ti and Rb).
- Sorting in a contourite system is not only a function of particle size but also of particle shape, density and composition. The more rounded siliciclastic contouritic sands in Mozambique can achieve a relative better sorting, while the irregularly shaped bioclastic sandy contourites in Corsica are very poorly sorted. Differences in the sorting of contouritic sands could be related to the particular hydrodynamic behaviour of bioclastic sands. The settling velocities of bioclastic particles are much lower than those of the siliciclastic sand fraction, hence a bioclastic-rich sediment input is prone to be exposed during longer periods to bottom currents. Once it is deposited, however, more vigorous bottom currents would be needed for reworking of the bioclastic particles.
- The variability in the ichnodiversity, abundance and distribution of bioturbation in both Mozambique and Corsica is linked to intermittent interactions between bottom currents and sediment supply, thus different environmental conditions for tracemakers. This points to the

intermittency of processes during the bi-gradational sequence deposition. The intermittency reflects shorter-time changes in hydrodynamic conditions, shorter-term higher accumulation rates and lower bioturbation rates, and flow variability during its deposition. We can therefore affirm that the formation of the studied bi-gradational sequences was discontinuous.

- Sediment input has a strong impact on the bi-gradational contourite sequence formation. Both, the Mozambique and the Corsica bi-gradational sequences developed mainly during periods of vigorous bottom currents in different contourite environments: in a contourite terrace in the Mozambican upper slope, and in a contourite drift in the Corsica Trough. However, they differ in terms of the proximity of the source area. The contourite drift offshore Corsica is located in the middle slope, and bioclastic sands would have been transported to the slope during sea-level lowstands probably during isolated episodes of winnowing and reworking and transport of sediments from the shelf and the shelf edge, mixed with pelagic and hemipelagic particles. In contrast, the Mozambique contourite terrace occupies shallower locations and lies directly offshore the Zambezi delta, meaning it was continuously supplied from the adjacent continent and shelf and by alongslope currents, especially during sea-level highstands. At further reflected by the thicknesses of the two bi-gradational sequences: the one offshore Mozambique has a thickness of about 2 m, while bi-gradational sequences in the contourite drift offshore Corsica have thicknesses below 60 cm.

In summary, the sedimentological characteristics of sandy contourites and bi-gradational sequences vary depending on the sediment composition (e.g., siliciclastic or bioclastic sands) and on the factors controlling the development of contourites in the area (i.e., oscillations in sediment supply and bottom-current velocity). It is therefore necessary to have a broad understanding of the geological, sedimentary and oceanographic setting in order to arrive at correct and detailed interpretations regarding bi-gradational sequences in contouritic deposits.

Acknowledgements

This project was funded through the Joint Industry Project supported by BP, ENI, ExxonMobil, TOTAL, Wintershall Dea and TGS, within the framework of "The Drifters" Research Group at Royal Holloway University of London (RHUL). The authors thank the Captain, crew and onboard scientific team of the PAMELA-MOZ04 cruise onboard the R/V Pourquoi pas?, as well as those of the PRISME2-PAPRICA and PRISME3 cruises (2013) onboard the R/V Atalante and the R/V Pourquoi pas?, respectively. The oceanographic cruise PAMELA-MOZ04 was co-funded by TOTAL and IFREMER as part of the PAMELA (PAssive Margin Exploration Laboratories) scientific project. The PAMELA project is a scientific project led by Ifremer and TOTAL in collaboration with Université de Bretagne Occidentale, Université Rennes 1, Université Pierre and Marie Curie, CNRS and IFPEN. The research by Javier Dorador was funded through a EU's Horizon 2020 research and innovation program under the Marie Skłodowska-Curie grant agreement No 792314 (ICON-SE). Heiko Hüneke (University of Greifswald, Germany) is thanked for the production of many excellent thin sections. We also thank two anonymous reviewers for their constructive comments that contributed and helped to sharpen the concepts presented in this contribution.

Data availability

Sediment cores collected offshore Mozambique and in Corsica Trough are curated at IFREMER core repository in Plouzané (France). Core data related to this article can be requested at:

Core MOZ4-CSF19: IGSN BFBGX-128004 (http://igsn.org/BFBGX-128004)

Core PSM3-CS009: IGSN BFBGX-87773 (http://igsn.org/BFBGX-87773)

References

Abdi, H., Williams, L.J. 2010. Principal component analysis. *Wiley interdisciplinary reviews: computational statistics*, 2(4), 433–459.

Adegbie, A.T., Schneider, R.R., Röhl, U., Wefer, G. 2003. Glacial millennial-scale fluctuations in central African precipitation recorded in terrigenous sediment supply and freshwater signals offshore Cameroon. *Palaeogeogr., Palaeoclimatol., Palaeoecol.,* 197, 323–333.

Alonso, B., Ercilla, G., Casas, D., Stow, D.A.V., Rodríguez-Tovar, F.J., Dorador, J. Hernández-Molina, F.J., 2016. Contourite vs gravity-flow deposits of the Pleistocene Faro Drift (Gulf of Cadiz): Sedimentological and mineralogical approaches. *Mar. Geol.,* 377, 77–94.

Astraldi, M., Gasparini, G.P. 1992. The seasonal characteristics of the circulation in the north Mediterranean basin and their relationship with the atmospheric-climatic conditions. *Journal of Geophysical Research: Oceans,* 97(C6), 9531–9540.

Arz, H.W., Pätzold, J., Wefer, G. 1999. Climatic changes during the last deglaciation recorded in sediment cores from the northeastern Brazilian Continental Margin. *Geo-Marine Letters*, 19(3), 209–218.

Baccelle, L. and Bosellini, A. 1965. Diagrammi per la stima visiva della composizione percentuale nelle rocce sedimentarie. Ann. Univ. Ferrara, N.S., Sez. IX, *Sci. Geol. Paleont.,* 1, 59–62.

Badalini, G., Thompson, P., Wrigley, S., Walker, R., Argent, J., Hernandez-Molina, J., de Santa Ana, H. 2016. Giant Cretaceous mixed contouritic-turbiditic systems, offshore Uruguay: the interaction between rift-related basin morphology, contour currents and downslope sedimentation. In *AAPG A*CE 2016, Calgary, 19–22 June 2016.

Bahr, A., Jiménez-Espejo, F.J., Kolasinac, N., Grunert, P., Hernández-Molina, F.J., Röhl, U., Voelker, A.H.L., Escutia, C., Stow, D.A.V., Hodell, D., Alvarez-Zarikian, C.A. 2014. Deciphering bottom current velocity and paleoclimate signals from contourite deposits in the Gulf of Cádiz during the last 140 kyr: An inorganic geochemical approach. *Geochem. Geophys.*, 15(8), 3145–3160.

Balaky, S.M. and Tamar-Agha, M.Y. 2017. Sedimentology and stratigraphy of Geli Khana Formation (Anisian–Ladinian), a contourite depositional system in the northeastern passive margin of Arabian plate, northern Iraq-Kurdistan region. *Arabian Journal of Geosciences*, 10, 118.

Barbera, G., Giudice, A.L., Mazzoleni, P., Pappalardo, A. 2009. Combined statistical and petrological analysis of provenance and diagenetic history of mudrocks: Application to Alpine Tethydes shales (Sicily, Italy). *Sed. Geol*, 213(1-2), 27–40.

Beal, L.M., Field, A., Gordon, A.L. 2000. The spreading of Red Sea overflow waters in the Indian Ocean. J. *Geophys. Res. Ocean*., 105 (C4), 8549–8564.

Blott, S.J., Pye, K. 2001. GRADISTAT: a grain size distribution and statistics package for the analysis of unconsolidated sediments. *Earth Surf. Process. Landforms*, 26(11), 237–1248.

Brackenridge, R.E., Hernández-Molina, F.J., Stow, D.A.V., Llave, E. 2013. A Pliocene mixed contourite–turbidite system offshore the Algarve Margin, Gulf of Cadiz: seismic response, margin evolution and reservoir implications. *Mar. Pet. Geol.,* 46, 36–50.

Brackenridge, R.E., Stow, D.A.V., Hernández-Molina, F.J., Jones, C., Mena, A., Alejo, I., Ducassou, E., Llave, E., Ercilla, G., Nombela, M.A., Pérez-Arlucea, M., Frances, G. 2018. Textural characteristics and facies of sand-rich contourite depositional systems. *Sedimentology*, 65(7), 2223–2252.

Cacho, I., Grimalt, J.O., Sierro, F.J., Shackleton, N., Canals, M. 2000. Evidence for enhanced Mediterranean thermohaline circulation during rapid climatic coolings. *Earth and Planetary Science Letters*, 183(3-4), 417–429.

Caley, T., Extier, T., Collins, J.A., Schefuß, E., Dupont, L., Malaizé, B., Rossignol, L., Souron, A., McClymont, E.L., Jimenez-Espejo, F.J., García-Comas, C., Eynaud, F., Martinez, P., Roche, D.M., Jorry, S.J., Jorry, Charlier, K., Wary, M., Gourves, P.Y., Billy, I., Giraudeau, J. 2018. A two-million-year-long hydroclimatic context for hominin evolution in southeastern Africa. *Nature*, 560, 76–79.

Calves, G., Toucanne, S., Jouet, G., Charrier, S., Thereau, E., Etoubleau, J., Marsset, T., Droz, L., Bez, M., Abreu, V., Jorry, S., Mulder, T., Lericolais, G. 2013. Inferring denudation variations from the sediment record; an example of the last glacial cycle record of the Golo Basin and watershed, East Corsica, western Mediterranean sea. *Basin Research*, 25(2), 197–218.

Capella, W., Hernández-Molina, F.J., Flecker, R., Hilgen, F. J., Hssain, M., Kouwenhoven, van Oorschot, M., Sierro, F.J., Stow, D.A.V., Trabucho-Alexandre, J., Tulbure, M.A., de Weger, W., Yousfi, M.Z. and

Krijgsman, W. 2017. Sandy contourite drift in the late Miocene Rifian Corridor (Morocco): Reconstruction of depositional environments in a foreland-basin seaway. *Sed. Geol.,* 355, 31–57.

Cattaneo, A. 2013a. PRISME 2 cruise, RV L'Atalante, doi.org/10.17600/13010050

Cattaneo, A. 2013b. PRISME 3 cruise, RV Pourquoi pas?, doi.org/10.17600/13030060

Cattaneo, A., Jouet, G. 2013. PAMELA-PAPRICA cruise, RV L'Atalante, doi.org/10.17600/13010300

Chabaud, L., Ducassou, E., Tournadour, E., Mulder, T., Reijmer, J.J., Conesa, G., Giraudeau, J., Hanquiez, V., Borgomano, J., Ross, L. 2016. Sedimentary processes determining the modern carbonate periplatform drift of Little Bahama Bank. *Mar. Geol.,* 378, 213–229.

Catuneanu, O. 2006. Principles of Sequence Stratigraphy: New York, Elsevier, 386 p.

Chen, H.F., Yeh, P.Y., Song, S.R., Hsu, S.C., Yang, T.N., Wang, Y., Chi, Z., Lee, M.T., Chen, M.T., Cheng, C.L., Zou, J., Chang, Y.P. 2013. The Ti/Al molar ratio as a new proxy for tracing sediment transportation processes and its application in aeolian events and sea level change in East Asia. *Journal of Asian Earth Sciences*, 73, 31–38.

Cooke, P.J., Nelson, C.S., Crundwell, M.P., Field, B.D., Elkington, E.S., Stone, H.H. 2004. Textural variations in Neogene pelagic carbonate ooze at DSDP Site 593, southern Tasman Sea, and their paleoceanographic implications. *New Zealand Journal of Geology and Geophysics*, 47(4), 787–807.

Courtene-Jones, W., Quinn, B., Ewins, C., Gary, S.F., Narayanaswamy, B.E. 2019. Consistent microplastic ingestion by deep-sea invertebrates over the last four decades (1976–2015), a study from the North East Atlantic. *Environ. Pollut.*, 244, 503–512.

Creaser, A., Hernández-Molina, F.J., Badalini, G., Thompson, P., Walker, R., Soto, M., Conti, B. 2017. A Late Cretaceous mixed (turbidite-contourite) system along the Uruguayan Margin: Sedimentary and palaeoceanographic implications. *Mar. Geol.,* 390, 234–253.

de Castro, S., Hernández-Molina, F.J., Rodríguez-Tovar, F.J., Llave, E., Ng, Z.L., Nishida, N., Mena, A. 2020a. Contourites and bottom current reworked sands. *Mar. Geol.,* 106267.

de Castro, S., Hernández-Molina, F.J., de Weger, W., Jiménez-Espejo, F.J., Rodríguez-Tovar, F.J., Mena, A., Llave, E. and Sierro, F.J. 2020b. Contourite characterization and its discrimination from other deep-water deposits in the Gulf of Cadiz contourite depositional system. *Sedimentology.* doi: 10.1111/sed.12813

de Ruijter, W.P.M., Ridderinkhof, H., Lutjeharms, J.R.E., Schouten, M.W., Veth, C. 2002. Observations of the flow in the Mozambique channel. *Geophys. Res. Lett.,* 29 (10), 140–141.

Deptuck, M.E., Piper, D.J., Savoye, B., Gervais, A. 2008. Dimensions and architecture of late Pleistocene submarine lobes off the northern margin of East Corsica. *Sedimentology,* 55(4), 869–898.

Dickson, A.J., Leng, M.J., Maslin, M.A., Röhl, U. 2010. Oceanic, atmospheric and ice-sheet forcing of South East Atlantic Ocean productivity and South African monsoon intensity during MIS-12 to 10. *Quat. Sci. Rev.,* 29, 3936–3947.

Donohue, K.A., Beal, L.M., Firing, E. 2000. Comparison of three velocity sections of the reversal of bottom water flow along the Pacific Margin of the Antarctic Peninsula: Stratigraphic evidence from a contourite sedimentary tail. *Mar. Geol.,* 228, 93–116.

Dorador, J., Rodríguez-Tovar, F.J. 2016. Stratigraphic variation in ichnofabrics at the "Shackleton Site" (IODP Site U1385) on the Iberian Margin: Paleoenvironmental implications*. Mar. Geol.,* 377, 118–126.

Dorador, J. and Rodríguez-Tovar, F.J. 2018. High-resolution image treatment in ichnological core analysis: initial steps, advances and prospects. *Earth Sci. Rev.,* 177, 226–237.

Dorador, J., Rodríguez-Tovar, F.J., IODP Expedition 339 Scientists. 2014a. Digital image treatment applied to ichnological analysis of marine core sediments. *Facies*, 60, 39–44.

Dorador, J., Rodríguez-Tovar, F.J., IODP Expedition 339 Scientists. 2014b. Quantitative estimation of bioturbation based on digital image analysis. *Mar. Geol.,* 349, 55–60.

Dorador, J., Rodríguez-Tovar, F.J., Mena, A., Francés, G. 2020. Lateral variability of ichnological content in muddy contourites: Weak bottom currents affecting organisms' behavior. Scientific Reports, 9, 17713.

Duan, T., Gao, Z., Zeng, Y., Stow, D.A.V. 1993. A fossil carbonate contourite drift on the Lower Ordovician palaeocontinental margin of the middle Yangtze Terrane, Jiuxi, northern Hunan, southern China. *Sedimentary Geology*, 82, 271–284.

Eberli, G.P., Betzler, C. 2019. Characteristics of modern carbonate contourite drifts. *Sedimentology*, 66(4), 1163–1191.

Ekdale, A.A., Bromley, R., Knaust, D. 2012. The ichnofabric concept. In: Knaust, D., Bromley, R.G. (Eds.), Trace Fossils as Indicators of Sedimentary Environments. *Developments in Sedimentology*. Elsevier, Amsterdam, 64, 139–155.

Faugères, J. C., Stow, D. A.V., Imbert, P., Viana, A. 1999. Seismic features diagnostic of contourite drifts. *Mar. Geol.,* 162(1), 1–38.

Faugères, J.C., Stow, D.A.V. 2008. Contourite drifts: nature, evolution and controls. *Dev. Sedimentol.,* 60, 257–288.

Flood, R.P., Orford, J.D., McKinley, J.M., Roberson, S. 2015. Effective grain size distribution analysis for interpretation of tidal–deltaic facies: West Bengal Sundarbans. *Sed. Geol.,* 318, 58–74.

Flood, R.P., Barr, I. D., Weltje, G. J., Roberson, S., Russell, M. I., Meneely, J., Orford, J.D. 2018. Provenance and depositional variability of the thin mud facies in the lower Ganges-Brahmaputra delta, West Bengal Sundarbans, India. *Mar. Geol.,* 395, 198–218.

Folk, R.L. and Robles, R. 1964. Carbonate sands of Isla Perez, Alacran reef complex, Yucatan. *J. Geol.,* 72(3), 255–292.

Folk, R.L. and Ward, W.C. 1957. Brazos River bar (Texas); a study in the significance of grain size parameters. *J. Sed. Res.,* 27(1), 3–26.

Fonnesu, M., Palermo, D., Galbiati, M., Marchesini, M., Bonamini, E., Bendias, D. 2020. A new world-class deep-water play-type deposited by the syndepositional interaction of turbidity flows and bottom currents: The giant Eocene Coral Field in northern Mozambique. *Mar. Petrol. Geol.,* 111, 179–201.

Fuhrmann, A., Kane, I.A., Clare, M.A., Ferguson, R.A., Schomacker, E., Bonamini, E., Contreras, F.A. 2020. Hybrid turbidite-drift channel complexes: An integrated multiscale model. *Geology*, 48(6), 562–568.

Gambacorta, G., Bersezio, R., Erba, E. 2014. Sedimentation in the Tethyan pelagic realm during the Cenomanian: Monotonous settling or active redistribution?. Palaeogeography, Palaeoclimatology, Palaeoecology, 409, 301–319.

Gervais, A., Savoye, B., Piper, D.J., Mulder, T., Cremer, M., Pichevin, L. 2004. Present morphology and depositional architecture of a sandy confined submarine system: the Golo turbidite system (eastern margin of Corsica). *Geological Society, London, Special Publications*, 222(1), 59–89.

Gervais, A., Mulder, T., Savoye, B., Gonthier, E. 2006. Sediment distribution and evolution of sedimentary processes in a small sandy turbidite system (Golo system, Mediterranean Sea): implications for various geometries based on core framework. *Geo-Marine Letters*, 26(6), 373.

Giresse, P., Wiewióra, A. 2001. Stratigraphic condensed deposition and diagenetic evolution of green clay minerals in deep water sediments on the Ivory Coast–Ghana Ridge. *Mar. Geol.,* 179(1-2), 51–70.

Giresse, P. 2008. Some aspects of diagenesis in contourites. *Dev. Sedimentol.*, 60, 203-221.

Gonthier, E.G., Faugères, J.C., Stow, D.A.V. 1984. Contourite facies of the Faro drift, Gulf of Cadiz. *Geological Society, London, Special Publications,* 15(1), 275–292.

Hammer, Ø., Harper, D.A., Ryan, P.D. 2001. PAST: Paleontological statistics software package for education and data analysis. *Palaeontologia electronica*, 4(1), 9.

Haq, B.U. 1993. Deep sea response to eustatic changes and significance of gas hydrates for continental margin stratigraphy. *Int. Assoc. Sediment., Spec. Pub.,* 118, 93–106.

Heaton, T.J., Köhler, P., Butzin, M., Bard, E., Reimer, R.W., Austin, W.E.N., Bronk Ramsey, C., Grootes, P.M., Hughen, K.A., Kromer, B., Reimer, P.J., Adkins, J.F., Burke, A., Cook, M.S., Olsen, J. and Skinner, L.C. 2020. Marine20—the marine radiocarbon age calibration curve (0–55,000 cal BP). *Radiocarbon*, 62, 725-757, doi:10.1017/RDC.2020.68

Hernández-Molina, F.J., Llave, E., Stow, D.A.V., García, M., Somoza, L., Vázquez, J.T., Lobo, F.J., Maestro, A., del Río, V.D., León, R., Medialdea, T. 2006. The contourite depositional system of the Gulf of Cadiz: a sedimentary model related to the bottom current activity of the Mediterranean outflow water and its interaction with the continental margin. *Deep-Sea Res. Part II Topical Stud. Oceanogr.,* 53(11-13), 1420–1463.

Hesse, R. 1975. Turbiditic and non-turbiditic mudstone of Cretaceous flysch sections of the East Alps and other basins. *Sedimentology*, 22, 387–416.

Hesse, R., Schacht, U. 2011. Early diagenesis of deep-sea sediments. *Dev. Sedimentol*., 63, 557–713.

Hodell, D., Crowhurst, S., Skinner, L., Tzedakis, P.C., Margari, V., Channell, J.E., Kamenov, G., Maclachlan, S., Rothwell, G. 2013. Response of Iberian Margin sediments to orbital and suborbital forcing over the past 420 ka. *Paleoceanography*, 28(1), 185–199.

Hüneke, H. Stow, D.A.V. 2008. Identification of ancient contourites: problems and palaeoceanographic significance. In: Rebesco, M., Camerlenghi, A. (Eds.), Contourites. *Dev. Sedimentol.*, 60, pp. 323-344.

Hüneke, H., Mulder, T. 2011. Deep-sea sediments. *Dev. Sedimentol*., 63, pp. 260-278.

Hüneke, H., Hernández-Molina, F.J., Rodríguez-Tovar, F.J., Llave, E., Chiarella, D., Mena, A., Stow, D.A.V. 2020. Diagnostic criteria based on microfacies for calcareous contourites, turbidites and pelagites in the Eocene-Miocene slope succession, southern Cyprus. *Sedimentology*, doi.org/10.1111/sed.12792

Jouet, G., Deville, E. 2015. PAMELA-MOZ04 cruise, RV Pourquoi pas ?, https://doi.org/10.17600/15000700

Kane, I.A., Clare, M. A., Miramontes, E., Wogelius, R., Rothwell, J.J., Garreau, P., Pohl, F. 2020. Seafloor microplastic hotspots controlled by deep-sea circulation. *Science,* 368(6495), 1140–1145.

Knaust, D. 2017. Atlas of Trace Fossils in Well Core: Appearance, Taxonomy and Interpretation. Springer, Dordrecht.

Krumbein, W.C. 1943. Fundamental attributes of sedimentary particles. *Univ. Iowa Stud. Eng. Bull.,* 27, 318–331.

La Violette, P.E. 1994. Overview of the major forcings and water masses of the western Mediterranean Sea. *Coastal and Estuarine Studies,* 1–1.

Li, H., van Loon, A.J., He, Y. 2020. Cannibalism of contourites by gravity flows: explanation of the facies distribution of the Ordovician Pingliang Formation along the southern margin of the Ordos Basin, China. *Canadian Journal of Earth Sciences*, 57, 331–347.

López Pérez, A., Rey, D., Martins, V., Plaza-Morlote, M., Rubio, B. 2019. Application of multivariate statistical analyses to ItraxTM core scanner data for the identification of deep-marine sedimentary facies: A case study in the Galician Continental Margin. *Quaternary International*, 514, 152–160.

López-Quirós, A., Escutia, C., Sánchez-Navas, A., Nieto, F., Garcia-Casco, A., Martín-Algarra, A., Evangelinos, D., Salabarnada, A. 2019. Glaucony authigenesis, maturity and alteration in the Weddell Sea: An indicator of paleoenvironmental conditions before the onset of Antarctic glaciation. *Scientific reports*, 9(1), 1–12.

Lowe, D.R. 1982. Sediment gravity flows; II, Depositional models with special reference to the deposits of high-density turbidity currents. *J. Sed. Res.,* 52(1), 279–297.

Lutjeharms, J.R.E. 2006. The Agulhas Current. vol. 329 Springer-Verlag Berlin Heidelberg, 978-3-540-37212-7.

Maboya, M.L., Meadows, M.E., Reimer, P.J., Backeberg, B.C. and Haberzettl, T. 2018. Late Holocene marine radiocarbon reservoir correction for the southern and eastern coasts of South Africa. *Radiocarbon*, 60, 571.

Mantyla, A.W., Reid, J. L. 1995. On the origins of deep and bottom waters of the Indian Ocean. *Journal of Geophysical Research: Oceans*, 100(C2), 2417–2439.

Margalef, O., Cañellas-Boltà, N., Pla-Rabes, S., Giralt, S., Pueyo, J.J., Joosten, H., Rull, V., Buchaca, T., Hernández, A., Valero-Gracés, B.L., Moreno, A., Sáez, A. 2013. A 70,000-year multiproxy record of climatic and environmental change from Rano Aroi peatland (Easter Island). *Global and Planetary Change*, 108, 72–84.

Martinez-Ruiz, F., Kastner, M., Gallego-Torres, D., Rodrigo-Gámiz, M., Nieto-Moreno, V., Ortega-Huertas, M. 2015. Paleoclimate and paleoceanography over the past 20,000 yr in the Mediterranean Sea Basins as indicated by sediment elemental proxies. *Quaternary Science Reviews*, 107, 25–46

Martorelli, E., Bosman, A., Casalbore, D., Chiocci, F., Conte, A. M., Di Bella, L., Ercilla, G., Falcini, F., Falco, P., Frezza, V., Gaglianone, G., Giaccio, B. and Mancini, M. 2020. Mid-to-late Holocene upper slope contourite deposits off Capo Vaticano (Mediterranean Sea): High-resolution record of contourite cyclicity, bottom current variability and sandy facies. *Mar. Geol.*, 106372.

Martins, L.R. 2003. Recent sediments and grain-size analysis. *Gravel,* 1, 90-105.

Matthew, A.J., Woods, A.J. Oliver, C. 1991. Spots before eyes: new comparison charts for visual percentage estimation in archaeological material. *In: Recent developments in ceramic petrology (Eds. A. Middleton and I. Freestone), Brit. Mus. Occasional Paper,* 81, 211–263.

Minto'o, C.A., Bassetti, M.A., Morigi, C., Ducassou, E., Toucanne, S., Jouet, G., Mulder, T. 2015. Levantine intermediate water hydrodynamic and bottom water ventilation in the northern Tyrrhenian Sea over the past 56,000 years: New insights from benthic foraminifera and ostracods. *Quaternary International*, 357, 295–313.

McCave, I.N. 1984. Size spectra and aggregation of suspended particles in the deep ocean. *Deep Sea Research Part A. Oceanographic Research Papers*, 31(4), 329–352.

McCave, I.N. Hall, I.R. 2006. Size sorting in marine muds: Processes, pitfalls and prospects for palaeoflow-speed proxies. *Geochem. Geophys. Geosyst.*, 7, Q10N05.

McCave, I.N. 2008. Size sorting during transport and deposition of fine sediments: sortable silt and flow speed. In: *Contourites* (Eds. M. Rebesco and A. Camerlenghi), *Dev. Sedimentol.*, 60, 121–142.

McCave, I.N., Thornalley, D.J.R., Hall, I.R. 2017. Relation of sortable silt grain-size to deep-sea current speeds: Calibration of the 'Mud Current Meter'. *Deep Sea Research Part I: Oceanographic Research Papers*, 127, 1–12.

Menard, H.W. 1950. Sediment movement in relation to current velocity. *J. Sediment. Petrol.,* 20, 148–160.

Middleton, G.V., Hampton, M.A. 1973. Sediment gravity flows: mechanics of flow and deposition. In Middleton, G.V., and Bouma, A.H. (eds.), Turbidity and Deep-Water Sedimentation. SEPM, Pacific Section, Short Course Lecture Notes, Anaheim, 1–38.

Millot, C. 1999. Circulation in the western Mediterranean Sea. *Journal of Marine Systems,* 20(1-4), 423–442.

Miramontes, E., Cattaneo, A., Jouet, G., Théreau, E., Thomas, Y., Rovere, M., Cauquil., E., Trincardi, F. 2016. The Pianosa contourite depositional system (northern Tyrrhenian Sea): Drift morphology and Plio-Quaternary stratigraphic evolution. *Mar. Geol.*, 378, 20–42.

Miramontes, E., Garziglia, S., Sultan, N., Jouet, G., Cattaneo, A. 2018. Morphological control of slope instability in contourites: a geotechnical approach. *Landslides,* 15(6), 1085–1095.

Miramontes, E., Penven, P., Fierens, R., Droz, L., Toucanne, S., Jorry, S. J., Jouet, G., Pastor, L., Silva Jacinto, R., Gaillot, A., Giraudeau, J., Raisson, F. 2019a. The influence of bottom currents on the Zambezi Valley morphology (Mozambique Channel, SW Indian Ocean): In situ current observations and hydrodynamic modelling. *Mar. Geol.,* 410, 42–55.

Miramontes, E., Garreau, P., Cattaneo, A., Caillaud, M., Jouet, G., Pellen, R., Hernández-Molina, F.J., Clare, M.A. 2019b. Contourite distribution in the NW Mediterranean Sea: new insights from hydrodynamic modelling. *Geomorphology*, 333, 43–60.

Miramontes E., Eggenhuisen J.T., Poneti, G., Silva Jacinto, R., Pohl, F., Hernández-Molina F.J. 2020a. Contour current-turbidity flow interaction from flume tank experiments: decoding processes and their morphological signatures. *Geology*, 48(4), 353–357.

Miramontes, E., Jouet, G., Thereau, E., Bruno, M., Penven, P., Guerin, C., Le Roy, P., Droz, L., Jorry, S.J., Hernández-Molina, F.J., Thiéblemont, A., Silva Jacinto, R., Cattaneo, A. 2020b. The impact of internal waves on upper continental slopes: insights from the Mozambican margin (southwest Indian Ocean). *Earth Surf. Process. Landforms*, 45, 1469–1482.

Mulder, T., Alexander, J. 2001. The physical character of subaqueous sedimentary density flows and their deposits. *Sedimentology,* 48(2), 269–299.

Mulder, T., Migeon, S., Savoye, B., Faugères, J.C. 2001. Inversely graded turbidite sequences in the deep Mediterranean: a record of deposits from flood-generated turbidity currents?. *Geo-Marine Letters*, 21(2), 86–93.

Mulder, T., Syvitski, J.P., Migeon, S., Faugeres, J.C., Savoye, B. 2003. Marine hyperpycnal flows: initiation, behavior and related deposits. A review. *Mar. Pet. Geol.,* 20(6-8), 861–882.

Mulder, T., Faugères, J.C., Gonthier, E. 2008. Mixed turbidite–contourite systems. In: Rebesco, M., Camerlenghi, A. (Eds.), Contourites. *Dev. Sedimentol.*, 60, 435–456.

Mulder, T., Hassan, R., Ducassou, E., Zaragosi, S., Gonthier, E., Hanquiez, Marchès, E., V., Toucanne, S. 2013. Contourites in the Gulf of Cadiz: a cautionary note on potentially ambiguous indicators of bottom current velocity. *Geo-Mar. Let.,* 33(5), 357–367.

Mulder, T., Gillet, H., Hanquiez, V., Ducassou, E., Fauquembergue, K., Principaud, M., Conesa, G., Le Goff, J., Ragusa, J., Bashah, S., Bujan, S., Reijmer, J.J.G., Cavailhes, T., Droxler, A.W., Blank, D.G., Guiastrennec, L., Fabregas, N., Recouvreur, A., Seibert, C. 2018a. Carbonate slope morphology revealing a giant submarine canyon (Little Bahama Bank, Bahamas). *Geology*, 46, 31–34.

Mulder, T., Gillet, H., Hanquiez, V., Reijmer, J.J.G., Droxler, A.W., Recouvreur, A., Fabregas, N., Cavailhes, T., Fauquembergue, K., Blank, D.G., Guiastrennec, L., Seibert, C., Bashah, S., Bujan, S., Ducassou, E., Principaud, M., Conesa, G., Le Goff, J., Ragusa, J., Busson, J., Borgomano, J. 2018b. Into the deep: a coarse-grained carbonate turbidite valley and canyon in ultra-deep carbonate setting. *Mar. Geol.,* 407, 316–333.

Mulder, T., Ducassou, E., Hanquiez, V., Principaud, M., Fauquembergue, K., Tournadour, E., Chabaud, L., Reijmer, J., Recouvreur, A., Gillet, H., Borgomano, J., Schmitt, A., Moal, P. 2019. Contour current imprints and contourite drifts in the Bahamian archipelago. *Sedimentology*, 66(4), 1192–1221.

Mutti, E., Cunha, R.S., Bulhoes, E.M., Arienti, L.M., Viana, A.R. 2014. Contourites and turbidites of the Brazilian marginal basins. In AAPG Annual Convention & Exhibition.

Näkki, P., Setälä, O., Lehtiniemi, M. 2017. Bioturbation transports secondary microplastics to deeper layers in soft marine sediments of the northern Baltic Sea. *Marine pollution bulletin*, 119(1), 255–261.

Näkki, P., Setälä, O., Lehtiniemi, M. 2019. Seafloor sediments as microplastic sinks in the northern Baltic Sea–Negligible upward transport of buried microplastics by bioturbation. *Environmental Pollution*, 249, 74–81.

O'Brien, N.R., Nakazawa, K. Tokuhashi, S. 1980. Use of Clay Fabric to Distinguish Turbiditic and Hemipelagic Siltstones and Silts. In: *Deep-Water Turbidite Systems*, D.A.V. Stow (Ed.).

Pemberton, S.G., Frey, R.W. 1982. Trace fossil nomenclature and the Planolites-Palaeophycus dilemma. *Journal of Paleontology*, 843–881.

Prager, E.J., Southard, J.B., Vivoni-Gallart, E.R. 1996. Experiments on the entrainment threshold of well-sorted and poorly sorted carbonate sands. *Sedimentology*, 43(1), 33–40.

Press, F. and Siever, F. 1986. Earth (2nd edition). W.H. Freeman, New York, 649 pp.

Rebesco, M., Pudsey, C.J., Canals, M., Camerlenghi, A., Barker, P. F., Estrada, F., Giorgetti, A. 2002. Sediment drifts and deep-sea channel systems, Antarctic Peninsula Pacific Margin. *Geological Society, London, Memoirs,* 22(1), 353–371.

Rebesco, M. 2005. Sedimentary environments contourites. In: *Encyclopedia of Geology*, Elsevier, Oxford, pp. 513–527.

Rebesco, M., Hernández-Molina, F.J., van Rooij, D., Wåhlin, A. 2014. Contourites and associated sediments controlled by deep-water circulation processes: state-of-the-art and future considerations. *Mar. Geol.,* 352, 111–154.

Revel, M., Ducassou, E., Skonieczny, C., Colin, C., Bastian, L., Bosch, D., Migeon, J., Mascle, J. 2015. 20,000 years of Nile River dynamics and environmental changes in the Nile catchment area as inferred from Nile upper continental slope sediments. *Quat. Sci. Rev.,* 130, 200–221.

Rodriguez-Tovar, F.J., Dorador, J. 2014. Ichnological analysis of pleistocene sediments from the IODP Site U1385 “Shackleton Site” on the Iberian margin: approaching paleoenvironmental conditions. *Palaeogeogr. Palaeoclimatol. Palaeoecol.*, 409, 24–32.

Rodríguez-Tovar, F.J., Miguez-Salas, O., Duarte, L.V. 2017. Toarcian Oceanic Anoxic Event induced unusual behaviour and palaeobiological changes in *Thalassinoides* tracemakers. *Palaeogeogr. Palaeoclimatol. Palaeoecol*., 485, 46–56.

Rodríguez-Tovar, F.J., Hernández-Molina, F.J., Hüneke, H., Llave, E. and Stow, D.A.V. 2019a. Contourite facies model: Improving contourite characterization based on the ichnological analysis. *Sedimentary Geology*, 384, 60–69.

Rodríguez-Tovar, F.J., Hernández-Molina, F.J., Hüneke, H., Chiarella, D., Llave, E., Mena, A., Miguez-Salas, O., Dorador, J., de Castro, S., Stow, D.A.V. 2019b. Key evidence for distal turbiditic-and bottom-current interactions from tubular turbidite infills. *Palaeogeogr. Palaeoclimatol. Palaeoecol*., 533, 109233.

Rohling, E.J., Foster, G.L., Grant, K.M., Marino, G., Roberts, A.P., Tamisiea, M.E., Williams, F. 2014. Sea-level and deep-sea-temperature variability over the past 5.3 million years. *Nature*, 508, 477–482.

Romahn, S., Mackensen, A., Kuhlmann, H. and Pätzold, J. 2015. Benthic foraminiferal response to Late Glacial and Holocene sea level rise and rainfall variability off East Africa. *Marine Micropaleontology*, 119, 34–48.

Rothwell, R.G., Hoogakker, B., Thomson, J., Croudace, I.W., Frenz, M. 2006. Turbidite emplacement on the southern Balearic Abyssal Plain (western Mediterranean Sea) during Marine Isotope Stages 1–3: an application of ITRAX XRF scanning of sediment cores to lithostratigraphic analysis. *Geological Society, London, Special Publications,* 267, 79–98.

Sansom, P. 2018. Hybrid turbidite–contourite systems of the Tanzanian margin. *Pet. Geosci.,* 24, 258–276.

Savoye, B. 2008. SIGOLO cruise, RV Le Suroît, https://doi.org/10.17600/80201

Schulz, H., Lückge, A., Emeis, K. C., Mackensen, A. 2011. Variability of Holocene to Late Pleistocene Zambezi riverine sedimentation at the upper continental slope off Mozambique, 15–21 S. *Mar. Geol.*, 286(1-4), 21–34.

Shanmugam, G. 2006. Deep-Water Processes and Facies Models: Implications for Sandstone Petroleum Reservoirs: Implications for Sandstone Petroleum Reservoirs, Vol. 5, Elsevier.

Shanmugam, G. .2008. Deep-water bottom currents and their deposits. In: *Contourites* (Eds Rebesco, M. and Camerlenghi). *Dev. Sedimentol*., 60, 59–81.

Shanmugam, G. 2016. Submarine fans: A critical retrospective (1950–2015). *J. Palaeogeog.*, 5(2), 110–184.

Siani, G., Paterne, M., Arnold, M., Bard, E., Métivier, B., Tisnerat, N., Bassinot, F. 2000. Radiocarbon reservoir ages in the Mediterranean Sea and Black Sea. *Radiocarbon*, 42, 271–280.

Smith, D.A., Cheung, K.F. 2005. Transport rate of calcareous sand in unidirectional flow. *Sedimentology*, 52(5), 1009–1020.

Southon, J., Kashgarian, M., Fontugne, M., Metivier, B., Yim, W. W-S. 2002. Marine reservoir corrections for the Indian Ocean and Southeast Asia. *Radiocarbon*, 44, 167–180.

Stanley, D.J. 1988. Turbidites reworked by bottom currents: upper cretaceous examples from St. Croix, US Virgin Islands. Smithsonian contributions to the marine sciences. *Mar. Sci.,* 33, pp. 85.

Stow, D.A.V., Piper, D.J.W. 1984. Deep-water fine-grained sediments: facies models. *Geol. Soc. Spec. Publ.*, 15(1), 611–646.

Stow, D.A.V., Wetzel, A. 1990. Hemiturbidite: a new type of deep-water sediment. In Proceedings of the ocean drilling program, scientific results. Ocean Drilling Program College Station, TX. Vol. 116, 25–34.

Stow, D.A.V., Tabrez, A.R. 1998. Hemipelagites: processes, facies and model. *Geol. Soc. Spec. Publ.,* 129(1), 317–337.

Stow, D. A. V., Faugères, J.C. 2008. Contourite facies and the facies model. *Dev. Sedimentol.*, 60, 223–256.

Stow, D.A.V., Hernández-Molina, F.J., Llave, E., Bruno, M., García, M., Díaz del Río, V., Somoza, L., Brackenridge, R.E. 2013. The Cadiz Contourite Channel: Sandy contourites, bedforms and dynamic current interaction. *Mar. Geol.,* 343, 99–114.

Stow, D.A.V., Smillie, Z. 2020. Distinguishing between Deep-Water Sediment Facies: Turbidites, Contourites and Hemipelagites. *Geosciences*, 10(2), 68.

Stuiver, M., Reimer, P.J., and Reimer, R.W. 2020. CALIB 8.2 [WWW program] at http://calib.org, accessed 2020-12-15.

Sierro, F.J., Flores, J.T., Baraza, J. 1999. Late glacial to recent paleoenvironmental changes in the Gulf of Cadiz and formation of sandy contourite layers. *Mar. Geol*., 155(1-2), 157–172.

Simons, D.B., Richardson, E.V., Albertson, M. 1961. Flume studies using medium sand (0.45 mm). *US Geol. Survey Water Supply Papers*, 1498-A.

Swart, N.C., Lutjeharms, J.R.E., Ridderinkhof, H., de Ruijter, W.P.M. 2010. Observed characteristics of Mozambique Channel eddies. *J. Geophys. Res.,* 115, 1–14.

Sweet, M.L., Gaillot, G.T., Jouet, G., Rittenour, T.M., Toucanne, S., Marsset, T., Blum, M.D. 2020. Sediment routing from shelf to basin floor in the Quaternary Golo System of Eastern Corsica, France, western Mediterranean Sea. GSA Bulletin, 132 (5-6), 1217–1234.

Takashimizu, Y., Kawamura, R., Rodríguez-Tovar, F.J., Dorador, J., Ducassou, E., Hernández-Molina, F.J., Stow, D.A.V., Alvarez-Zarikian, C.A. 2016. Reworked tsunami deposits by bottom currents: circumstantial evidences from Late Pleistocene to Early Holocene in the Gulf of Cádiz. *Mar. Geol.*, 377, 95–109.

Talling, P.J., Masson, D.G., Sumner, E.J. Malgesini, G. 2012. Subaqueous sediment density flows: Depositional processes and deposit types. *Sedimentology*, 59(7), 1937–2003.

Tallobre, C., Giresse, P., Bassetti, M. A., Loncke, L., Bayon, G., Buscail, R., Tudryn, A., Zaragosi, S. 2019. Formation and evolution of glauconite in the Demerara Contourite depositional system related to NADW circulation changes during late Quaternary (French Guiana). *J. S. Am. Earth Sci*., 92, 167–183.

Thiéblemont, A., Hernández-Molina, F. J., Miramontes, E., Raisson, F., Penven, P. 2019. Contourite depositional systems along the Mozambique channel: The interplay between bottom currents and sedimentary processes. *Deep Sea Research Part I: Oceanographic Research Papers*, 147, 79–99.

Thomson, J., Crudeli, D., de Lange, G.J., Slomp, C.P., Erba, E., Corselli, C.T., Calvert, S.E. 2004. Florisphaera profunda and the origin and diagenesis of carbonate phases in eastern Mediterranean sapropel units. *Paleoceanography*, 19(3).

Tisnérat-Laborde, N., Montagna, P., McCulloch, M., Siani, G., Silenzi, S., Frank, N. 2013. A high-resolution coral-based Δ14C record of surface water processes in the western Mediterranean Sea. *Radiocarbon*, 55, 1617–1630.

Toucanne, S., Jouet, G., Ducassou, E., Bassetti, M.A., Dennielou, B., Minto'o, C.M.A., Lahmi, M., Touyet, N., Charlier, K., Lericolais, G., Mulder, T. 2012. A 130,000-year record of Levantine Intermediate Water flow variability in the Corsica Trough, western Mediterranean Sea. *Quaternary Science Reviews,* 33, 55–73.

Ullgren, J.E., van Aken, H.M., Ridderinkohof, H., de Ruijter, W.P.M. 2012. The hydrography of the Mozambique Channel from six years of continuous temperature, salinity, and velocity observations. *Deep Sea Res. Oceanogr. Res. Pap.,* 69, 36–50.

van den Berg, B.C., Sierro, F.J., Hilgen, F.J., Flecker, R., Larrasoaña, J.C., Krijgsman, W., Flores, J.A., Mata, M.P. 2018. Imprint of Messinian salinity crisis events on the Spanish Atlantic margin. *Newsl. Stratigr.,* 51, 93–115.

van der Lubbe, H.J.L., Frank, M., Tjallingii, R., Schneider, R.R. 2016. Neodymium isotope constraints on provenance, dispersal, and climate-driven supply of Zambezi sediments along the Mozambique Margin during the past∼ 45,000 years. *Geochemistry, Geophysics, Geosystems*, 17(1), 181–198.

Viana, A.R., Faugères, J.C. 1998. Upper slope sand deposits: the example of Campos Basin, a latest Pleistocene-Holocene record of the interaction between along slope and down slope currents. In: Stoker, M. S., Evans, D., Cramp, A. (eds) Geological Processes on Continental Margins: Sedimentation, Mass-Wasting and Stability. *Geol. Soc. Spec. Publ.,* 129, 287–316.

Viana, A.R. 2008. Economic relevance of contourites. *Developments in Sedimentology*, 60, 491-510.

Vignudelli, S., Gasparini, G.P., Astraldi, M., Schiano, M.E. 1999. A possible influence of the North Atlantic Oscillation on the circulation of the Western Mediterranean Sea. *Geophysical Research Letters*, 26(5), 623–626.

Yu, X., Stow, D.A.V., Smillie, Z., Esentia, I., Brackenridge, R., Xie, X., Bankole, S., Ducassou, E., Llave, E. 2020. Contourite porosity, grain size and reservoir characteristics. *Mar. Pet. Geol.*, 104392.

Zavala, C., Arcuri, M., Di Meglio, M., Diaz, H. G., Contreras, C. 2011. A genetic facies tract for the analysis of sustained hyperpycnal flow deposits. in R. M. Slatt and C. Zavala, eds., Sediment transfer from shelf to deep water—Revisiting the delivery system: AAPG Studies in Geology, 61, 31–51.

Zavala, C. 2020. Hyperpycnal (over density) flows and deposits. *Journal of Palaeogeography*, 9(1), 1–21.

Walford, H.L., White, N.J., Sydow, J.C. 2005. Solid sediment load history of the Zambezi Delta. *Earth Planet Sci Lett.,* 238, 49–63.

Wang, X., Zhuo, H., Wang, Y., Mao, P., He, M., Chen, W., Wang, M. 2018. Controls of contour currents on intra-canyon mixed sedimentary processes: Insights from the Pearl River Canyon, northern South China Sea. *Mar. Geol.*, 406, 193–213.

Winterwerp, J.C., van Kesteren, W.G.M. 2004. Introduction to the Physics of Cohesive Sediment in the Marine Environment. *Dev. Sedimentol.*, 57, Elsevier, Amsterdam, 466 pp.

Wold, S., Esbensen, K., Geladi, P. 1987. Principal component analysis. *Chemometrics and intelligent laboratory systems*, 2(1-3), 37–52.

Zavala, C. 2020. Hyperpycnal (over density) flows and deposits. *Journal of Palaeogeography*, 9, 1-21.

Zhang, X., Zhang, T., Lei, B., Zhang, J., Yong, J. 2020. A giant sandy sediment drift in early Silurian (Telychian) and its multiple sedimentological process. *Mar. Pet. Geol.,* 113, 104077.

Ziegler, M., Simon, M. H., Hall, I. R., Barker, S., Stringer, C., Zahn, R. 2013. Development of Middle Stone Age innovation linked to rapid climate change. *Nature communications*, 41, 1–9.

Zou, H., Hastie, T., Tibshirani, R. 2006. Sparse principal component analysis. *Journal of computational and graphical statistics*, 15(2), 265–286.

Table captions.

Table 1. MOZ4-CSF19 and PSM3-CS009 core summary.

Table 2. Radiocarbon calibrated ages for PSM3-CS009 and MOZ4-CSF19. For PSM3-CS009 mean ΔR = -124, uncertainty = 22 (obtained from points number 221, 222, 1943) (Tisnérat-Laborde et al., 2013; Siani et al., 2000). For MOZ4-CSF19 mean ΔR = 45, uncertainty = 85 (obtained from points number 487, 488, 1909 and 1918) (Maboya et al., 2017; Southon et al., 2020).

Table 3. Synoptic table with sedimentary facies observations and interpretations.

Table 4. Relative percentage frequency of different components determined by means of the visual-comparison charts of Baccelle and Bosellini (1965) and Matthew et al. (1991).

Figure captions

Figure 1. A) Regional bathymetric map of the Mozambique Channel showing the main ocean currents. MC: Mozambique Current; MUC: Mozambique Undercurrent; ME: Mozambique eddies. B) Bathymetric map showing the study area and the location of the studied core MOZ4-CSF19 (modified from Miramontes et al., 2020b). The black line indicates the location of the seismic line used in Figure 2A. C) Regional bathymetric map of the Corsica Trough and extension of the contourite drifts that form the Pianosa Contourite Depositional System and of the turbidite lobes of the Golo Turbidite Network (modified from Miramontes et al., 2016). D) Bathymetric map showing the study area and the location of the studied core PSM3-CS009.

Figure 2. A) Multi-channel high-resolution seismic reflection profile (MOZ4-HR-114) showing the main depositional and erosional features observed in the upper and middle slope and the projected location of core MOZ4-CSF19 (modified from Miramontes et al., 202020). B) Photography of the seabed at the core site characterised by straight- to sinuous-crested current ripples. C) Sub-bottom profiler image (PSM2-CH-064) showing the location of core PSM3-CS009 with black line (modified from Miramontes et al., 2016).

Figure 3. A) Grain size distribution curve, and sedimentary facies log plotted against, linear sedimentation rates, PC distribution and elemental ratios downcore of MOZ4-CSF19. The coloured band indicates the interval when bottom currents and the sediment supply by the Zambezi river activity were coeval. Principal Component for M-PC1 (B) and M-PC2 (C) of MOZ4-CSF19.

Figure 4. High-resolution core images and X-Ray radiographs of the Mozambique channel (MOZ4-CSF19) for the sedimentary facies MF1 (A, B, C, D, E, F) and MF2 (E, F) showing the location and abundance of trace fossils assemblages and ichnofabrics: *Planolites* (*Pl*), *Thalassinoides* (*Th*), *Nereites* (*Ne*), *Scolicia* (*Sc*) and probable *Skolithos* (?*Sk*). Blue rhombuses indicate slight changes in matrix content in MF1 based on X-Ray radiographs and grain size curve of Fig. 3. The darkest areas in the X-Ray radiograph represent the coarsest grain size. The black boxes indicate the location for thin sections from Fig 6. A, B) MOZ4-CSF19-S1 shows the top of the bi-gradational sequence. The white box highlights the area where an irregular surface can be identified at 70 cm depth, under which *Thalassinoides* are very well developed suggesting the presence of an omission surface. The blue vertical arrow pointing downwards indicates the penetration depth of *Thalassinoides*. C, D) MOZ4-CSF19-S2 represents the bottom part of the sequence. (E, F) MOZ4-CSF19-S3 displays the bioturbated transition between MF2 and MF1 which is represented by ichnofabric i2, showing *Thalassinoides* filled by coarse-grained material from above or eroded layers. Here, MF1 is darker than in the rest of the sequence suggesting low-oxygen conditions during its deposit. MF2 is characterised by abundant and well-developed *Palaeophycus (Pa)* implying nutrient inputs (orange box).

Figure 5. Cross-plot of sorting (Φ) against D50 (µm) showing different trends for siliciclastic (MOZ4-CSF19) and bioclastic-rich (PSM3-CS009) contourite sands. Note how bioclastic-rich contourite sands are less sorted with the increase of grain size whereas siliciclastic sands are better sorted with the increased of grain size.

Figure 6. Photographs of large thin-sections showing the general texture of MF1 (A, B) and MF2 (C). A) Grain-supported texture in the middle and top part of the sequence. No significant lamination or bioturbation is present. The dark elongated particles comprise bioclasts (mainly coraline algae). B) Matrix-supported and grain-supported patches at the base of the sequence. The yellow dashed lines indicate the boundaries of the patches. This texture probably represents an originally more regular sedimentary lamination that was disturbed by bioturbation. C) Matrix-supported texture. Note that some areas are grain-supported and irregular laminae of dark-brown carbonaceous material is dominant. This texture could not represent the original depositional feature, since is related to the preparation of the thin section during induration. The white boxes indicate the location of thin sections in Fig. 7.

Figure 7. A, B) MF1 grain-supported fabric lacking any residual matrix at the top of the sequence showing major amount of larger bioclasts, planktic/benthic foraminifers and heavy minerals. C) MF1 grain-supported fabric with residual matrix surrounding quartz grains (blue arrows) and the presence of larger bioclasts (coralline algae on the left-hand side of the photograph) and heavy minerals (pink dots). D) Iron-rich matrix supported area in MF1 with subangular quartz grains, planktic foraminifers and few heavy minerals (pink dots). E) Grain-supported fabric in MF1 at the base of the sequence with a predominant quartz grain composition and rare foraminifers and bioclasts. Heavy minerals are common and marked with pink dots. Some of them are easily identified as titanite (Ti), garnet (Gt), zircon (Zr), epidote (Ep) or amphibole/pyroxene (Aph/Px). F) Cross-polarized (XPL) grain-supported fabric in MF1 at the base of the sequence with a preferential orientation of elongated particles such as bioclasts and micas (yellow dots). G, H) MF2 matrix-supported texture composed mainly by iron-

rich argillaceous matrix (50% in G and 80% in H) and subangular quartz grains. Heavy minerals, bioclasts, and foraminifers are rare.

Figure 8. High-resolution core images and X-Ray radiographs of the Mozambique channel (MOZ04-CSF19) MF2 (A, B) and MF3 (C, D) showing the location and abundance of trace fossil assemblages. ?*Zoophycos* (*?Zo*), *Nereites* (*Ne*), *Chondrites* (*Ch*), *Planolites* (*Pl*), *Thalassinoides* (*Th*) and *Mycelia* (*My*).

Figure 9. A) Grain size distribution curve, and sedimentary facies log plotted against PC distribution and elemental ratios downcore of MOZ4-CSF19. Coloured band indicates a terrigenous input related to a sediment suspension cloud. Principal Component of C-PC1 and C-PC2 of MOZ4-CSF19 are shown in B and C.

Figure 10. High-resolution core images (A, C, D) and X-Ray radiograph (B) of the Corsica Trough (PSM3-CS009). A, B) CF1 reversely- and normally-graded bioclastic sands showing the location and abundance of trace fossil assemblages. *Planolites* (*Pl*), *Thalassinoides* (*Th*) and *Chondrites* (*Ch*). The darker the area in the X-Ray radiograph, the coarser the grain size. The black boxes indicate the location for thin sections from Fig. 8. Blue rhomb indicates slight changes in matrix content in CF1 based on X-Ray radiograph and grain size curve of Fig. 3. Note the gradational contact between CF1 and CF2 at the top and CF3 at the bottom of the sequence. As in MF1 this bi-gradational sequence is characterised by i1, i2 and i3 ichnofabrics. The blue vertical arrows pointing downwards indicate the penetration depth of *Th*. C) CF2 muddy contourite burrowed with *Thalassinoides, Planolites* and rare *Chondrites* and *Scolicia* (*Sc*). D) CF3 Hemipelagite showing *Thalassinoides, Planolites*, *Chondrites* and *Scolicia* burrows. Although the visual distinction between CF3 and CF2 is not straightforward, not that the geochemical signal observed in Fig. 8C is different. E) Hemipelagite subjected to a distal turbulent flow. The trace fossil assemblage is different from the pure hemipelagites and muddy contourite displaying *Nereites* (*Ne*) and undifferentiated vertical traces (?vt), indicating relatively rapid deposition.

Figure 11. Photographs of large thin-sections (A, B, C) for CF1 with the general patchy texture of wackestone and packstone throughout the bi-gradational sequence. As in MF1, this texture probably

represents an originally more regular sedimentary lamination that was disturbed by bioturbation. The white boxes indicate the location for thin sections in Fig. 12.

Figure 12. Packstone fabric in CF1 (A, B) with abundant planktic and benthic foraminifers that may be empty (blue dots) or filled by glauconite (pink dots). Glauconite can present brownish (orange dots) or greenish (green dots) colours. Bioclasts are usually fragmented and the matrix is composed by micrite. C, D) CF1 wackestone fabric with different amounts of matrix (∼80% in C and ∼45% in D). In these areas, benthic foraminifers and foraminifers tests filled by glauconite are less abundant, but they have major proportions of fine-grained quartz grains.

Figure 13. PC1 vs. PC2 cross-plots for Mozambique (A) and Corsica (B) datasets.

Figure 14. Sketches explaining the differences between (A) winnowing and (B) reworking, and how they are reflected in Mozambique siliciclastic sands and Corsica bioclastic sands.

Figure 15. Schematic radiocarbon age model for Mozambique and Corsica bi-gradational sequences. Modified from Takashimizu et al. (2016). Models 1 and 2 assume that the base and top intervals of the sequences show different ages (i.e., $\Delta T \neq 0$), suggesting continuous accumulation over a relatively long period. Model 3 assumes that the top and basal horizons are of similar age (i.e., $\Delta T=0$) and, therefore, the deposit corresponds to a rapid deposition event from a gravity-driven flow.

Figure 16. Representation of the possible interactions between bottom currents, sediment input and hemipelagic settling in the development of *Planolites/Thalassinoides* ichnofabric. *Planolites* essentially reflects simple, horizontal, actively filled burrow systems of (respectively) deposit-feeding or predaceous organisms (Pemberton and Frey, 1982), and is usually associated with low-sedimentation rates (Rodríguez-Tovar et al., 2019a, b). *Planolites* is a softground tracemaker and usually develops bioturbation horizons up to 3 cm deep in the sediment-water interface (Interaction A, C, E and G). The presence of *Thalassinoides* indicates a break in sedimentation that led to early compaction (increased substrate consistency), of initial softground (Interaction B, D and F). *Planolites/Thalassinoides* ichnofabric indicates increasing substrate cohesion from softground (*Planolites*) conditions into firmground (*Thalassinoides*). This suggests that during the deposition of Mozambique siliciclastic

sands and Corsica bioclastic sands the energy regime was intermittent (Rodríguez-Tovar et al., 2019a, b; de Castro et al., 2020a, b). The colours do not represent changes in grain size, but are meant to differentiate each possible interaction. The order of the interactions does not represent a real trend.

Figure 17. Sketches explaining the facies identified in Mozambique (A) and Corsica (B), and related to the distal part of a contourite terrace and the adjacent plastered drift. Top-cut (A) and Complete (B) bi-gradational sequences and their sedimentary facies are illustrated in each setting, including the vertical changes in their microfacies and their link with dominant sedimentary processes (see text for further explanations).

Core ID	Cruise	Water depth	Core length	Total sections	Detailed studied sections	Deposit
MOZ4-CSF19	PAMELA-MOZ04, 2015 R/V Pourquoi pas?	315	9.24 m	10	S1, S2 and S3	Contourite terrace
PSM3-CS009	PRISME3, 2013 R/V Pourquoi pas?	370 m	21.26 m	23	S14	Plastered drift-mounded deposit

Core	Depth (m)	Lab. no.	Material	Age 14C (BP)	cal BP age range 1 sigma	cal BP range 2 sigma	Median probability
MOZ4-CSF19	0.055	Beta-447916	*G.trilobus trilubos*	3170 ± 30	2644 - 2897	2481 - 3023	2761
MOZ4-CSF19	2.155	Beta-447917	*G.trilobus trilubos*	8710 ± 30	9002 - 9264	8868 - 9407	9135
MOZ4-CSF19	3.005	Beta-462599	Bulk planktonic foraminifera	10180 ± 30	10913 - 11203	10729 - 11311	11060
MOZ4-CSF19	4.505	Beta-462602	Bulk planktonic foraminifera	11320 ± 30	12535 - 12729	12417 - 12834	12631
MOZ4-CSF19	7.005	Beta-470569	Bulk planktonic foraminifera	13240 ± 40	14875 - 15189	14653 - 15361	15031
MOZ4-CSF19	9.055	Beta-447918	Bulk planktonic foraminifera	14950 ± 40	17044 - 17354	16895 - 17564	17208
PSM3-CS009	11.26	Poz-63393	Bulk planktonic foraminifera	26880 ± 330	30051 - 30694	29777 - 30991	30368
PSM3-CS009	14.00	Beta-394859	Bulk planktonic foraminifera	26000 ± 110	29311 - 29690	29176 - 29836	29507

Facies acronym	MF1	MF2	MF3	CF1	CF2	CF3
Facies name	Mottled fine-grained sand	Homogenous medium-grained silt	Thin-bedded medium-grained silt	Mottled fine-grained sand	Mottled fine- to coarse-grained silt	Homogenous fine-grained silt
Grain size range	19.1-152.6 µm	4.9-20.32 µm	4.9-12.3 µm	6.1-275.4 µm	6.10-30.83 µm	5.96-11.49 µm
Gradation	Reversely graded	Massive	Bi-gradational	Bi-gradational	Massive	Massive
Sedimentary structures	- Ripples in the seafloor	-	Parallel to low-angle lamination (X-Ray)	-	-	-
Top	Seafloor	Gradational	Gradational	Gradational	Gradational	Gradational
Base	Gradational	Gradational	Gradational	Gradational	Gradational	Gradational
Thickness	2 m	Up to 3 m	1 m	Up to 60 cm	1 – 4 m	Up to 9.7 m
Geochemistry (PCA)	M-PC1 positively loaded High in Zr/Ti Low in K+Fe+Ti/Ca+Sr	M-PC1 negatively loaded or zero Low in Zr/Ti High in K+Fe+Ti/Ca+Sr	M-PC1 negatively loaded Low in Zr/Ti High in K+Fe+Ti/Ca+Sr	C-PC1 negatively loaded High in Sr/Ca Low in K+Fe+Ti/Ca+Sr	C-PC1 negatively loaded or zero Low in Sr/Ca Low in K+Fe+Ti/Ca+Sr	C-PC1 positively loaded Low in Sr/Ca High in K+Fe+Ti/Ca+Sr
Main trace fossil assemblages	*Palaeophycus, Planolites, Thalassinoides*	*Palaeophycus, Planolites, Thalassinoides, Nereites*	*Planolites, Thalassinoides, Nereites, Zoophycos*	*Planolites, Thalassinoides*	*Planolites, Thalassinoides, Scolicia, Chondrites*	*Planolites, Thalassinoides, Scolicia, Chondrites*
Microfacies	Rich in quartz grains, bioclasts and heavy minerals	Rich in clays and quartz grains	-	Rich in planktonic/benthonic foraminifers and other bioclasts	-	-
Fabric	Predominantly grain-supported	Matrix-supported	-	Grain-supported with matrix supported patches	-	-
Interpretation	Siliciclastic sandy contourite	Siliciclastic muddy contourite	Hyperpycnite	Bioclastic sandy contourite	Muddy contourite	Hemipelagite
Inferred sedimentary processes	Alternations of suspension and traction	Lateral advection from bottom currents	Lateral advection from a turbulent flow	Alternations of suspension and traction	Lateral advection from bottom currents	Vertical settling

MOZ4-CSF19

Section	Interval (m)	Facies	Quartz	Feldespar	Lithic fragments	Glauconite	Bioclasts	Benthic forams	Planktic forams	Matrix	Accessories
S1	0.1-0.2	MF1	60	5	0	0	10	2	5	0	5
S1	0.6-0.7	MF1	60	7.5	0	1	5	5	10	0	12.5
S2	0.95-1.05	MF1	40	5	1	1	20	10	15	0	5
S2	1.06-1.16	MF1	20	0	0	0	5	5	10	50	10
S2	1.69-1.79	MF1	70	2	0	1	10	5	15	0	10
S3	1.96-2.06	MF1	40	2.5	0	2	5	2	10	20	2
S3	2.43-2.53	MF2	50	5	0	0	0	5	5	25	5
S3	2.43-2.53	MF2*	10	2	0	0	0	0	2	85	1

PSM3-CS009

Section	Interval (m)	Facies	Quartz	Empty planktic forams	Forams filled by glauconite	Broken planktic forams	Empty Benthic forams	Glauconite	Bioclast	Matrix	Accessories/ opaques
S14	12.40-12.50	CF1 (P)	5	20	20	5	10	5	15	20	0
S14	12.40-12.50	CF1 (W)	1	10	10	2	15	5	15	45	0
S14	12.50-12.60	CF1 (P)	2	15	5	2	15	3	10	35	0
S14	12.50-12.60	CF1 (W)	5	10	0	0	2	1	2	80	0
S14	12.72-12.82	CF1 (P)	1	15	15	2	15	5	10	35	1
S14	12.72-12.82	CF1 (W)	1	10	5	0	1	1	2	80	0

Highlights

- Reworking proxies are different for bioclastic and siliciclastic sands
- Winnowing and reworking bottom current effects have a distinctive geochemical signal and they are observed at the microfacies scale
- Bi-gradational contourite sequence show evidences of intermittent depositional conditions
- Sediment input and distance to sediment source has a strong impact on the bi-gradational contourite sequence formation
- Contourite drifts are not only formed by contourite deposits

Declaration of Interest statement

We declare that we do not have any commercial or associative interest that represents a conflict of interest in connection with the work submitted.

Sandra de Castro

Figure 1

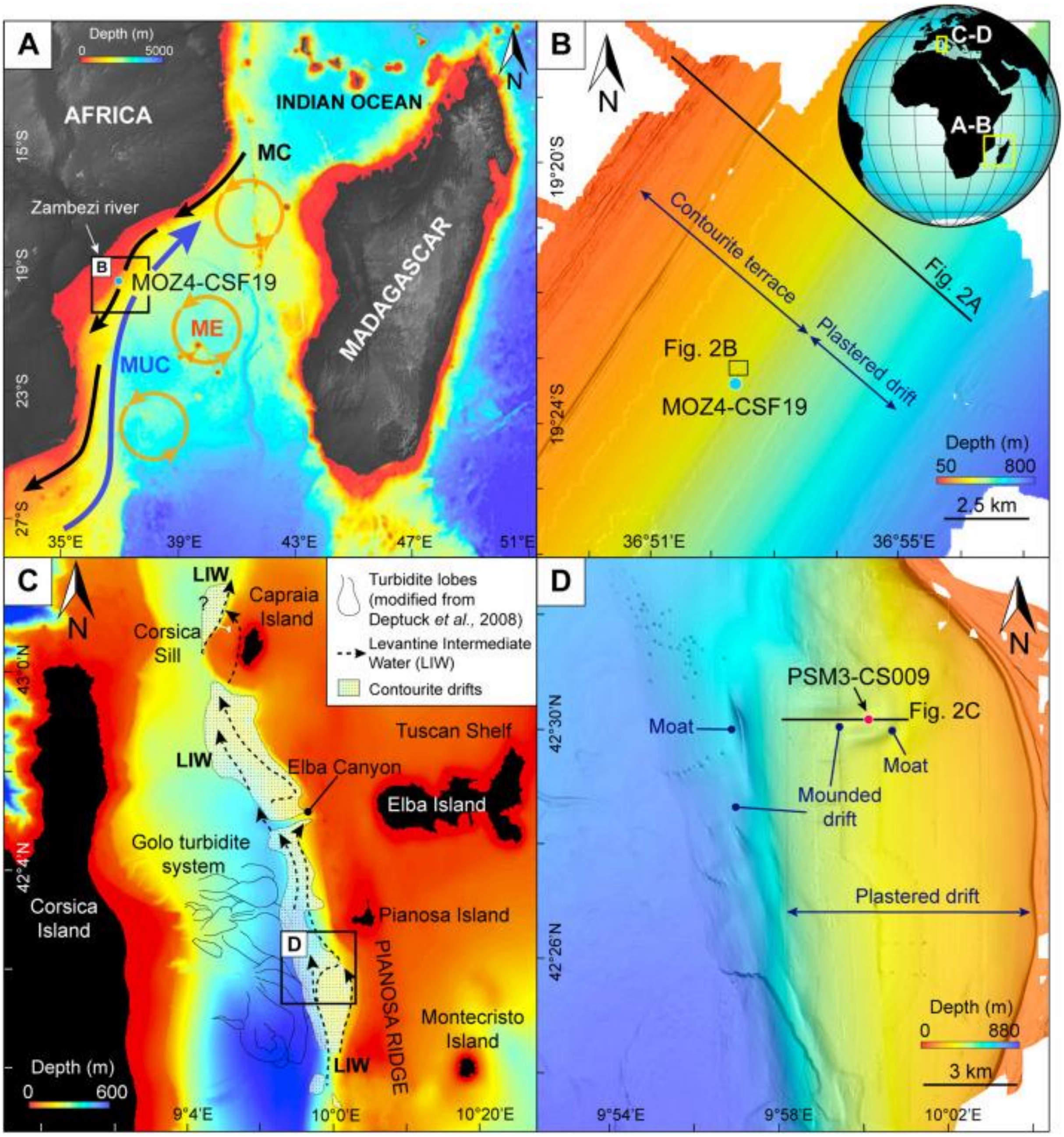

A
Depth (m)
0
5000
N
AFRICA
INDIAN OCEAN
MC
15°S
Zambezi river
B
19°S
MOZ4-CSF19
ME
MADAGASCAR
MUC
23°S
27°S
35°E
39°E
43°E
47°E
51°E
B
N
19°20'S
Contourite terrace
Fig. 2A
Plastered drift
Fig. 2B
MOZ4-CSF19
19°24'S
Depth (m)
50
800
2.5 km
36°51'E
36°55'E
C-D
A-B
C
N
LIW
?
Capraia Island
Corsica Sill
Turbidite lobes (modified from Deptuck et al., 2008)
Levantine Intermediate Water (LIW)
Contourite drifts
43°0'N
Tuscan Shelf
LIW
Elba Canyon
Elba Island
Golo turbidite system
42°4'N
Corsica Island
Pianosa Island
D
PIANOSA RIDGE
Montecristo Island
LIW
Depth (m)
0
600
9°4'E
10°0'E
10°20'E
D
N
PSM3-CS009
Moat
Fig. 2C
42°30'N
Moat
Mounded drift
Plastered drift
42°26'N
Depth (m)
0
880
3 km
9°54'E
9°58'E
10°02'E

Figure 2

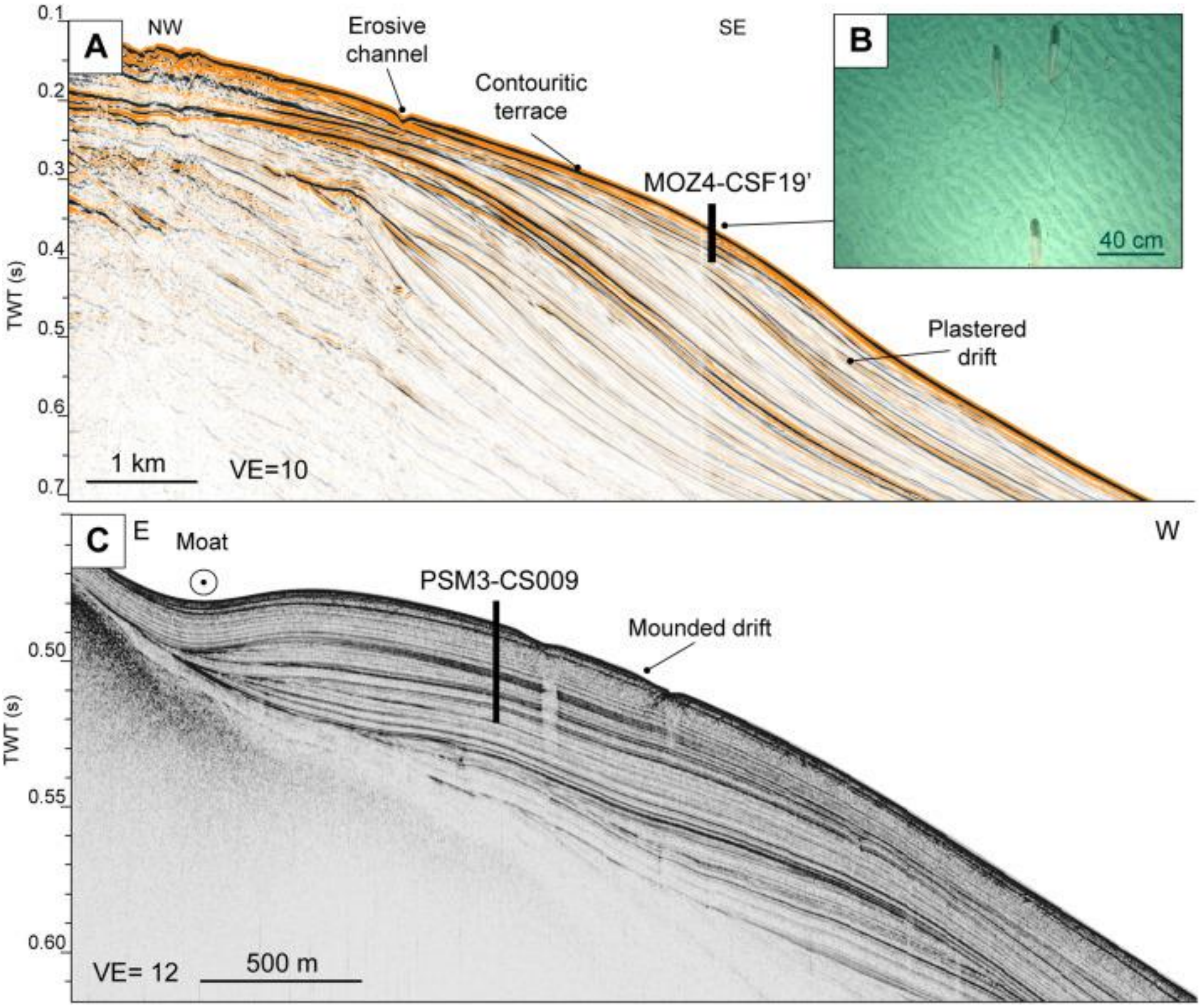
A
NW
Erosive channel
Contouritic terrace
SE
MOZ4-CSF19'
Plastered drift
B
40 cm
TWT (s)
0.1
0.2
0.3
0.4
0.5
0.6
0.7
1 km
VE=10
C
E
Moat
W
PSM3-CS009
Mounded drift
0.50
0.55
0.60
VE= 12
500 m

Figure 3

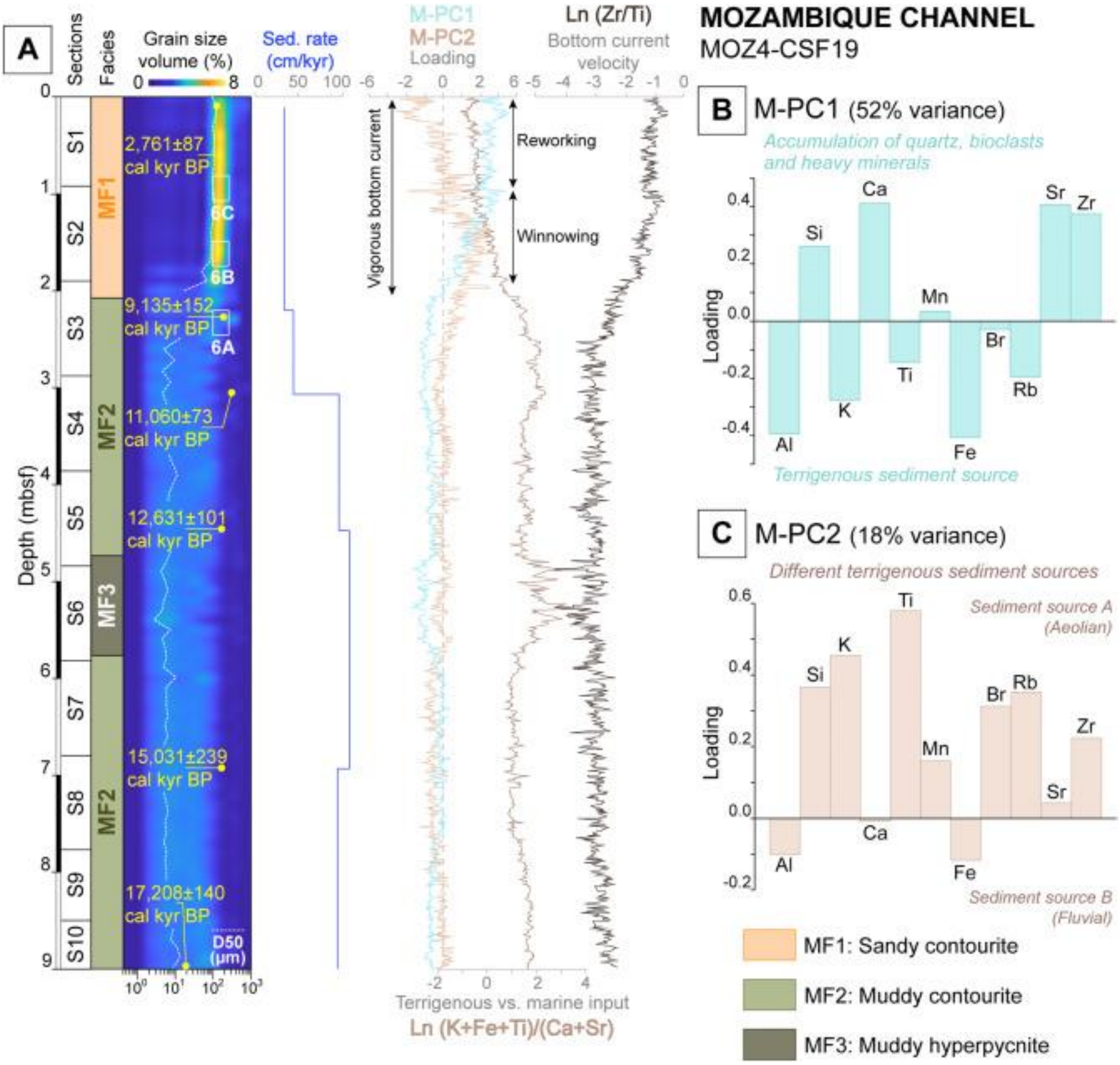
A
Sections
Facies
Grain size volume (%)
0
8
Sed. rate (cm/kyr)
0 50 100
M-PC1
M-PC2
Loading
-6 -2 0 2 6
Ln (Zr/Ti)
Bottom current velocity
-5 -4 -3 -2 -1 0
Depth (mbsf)
0 1 2 3 4 5 6 7 8 9
S1 S2 S3 S4 S5 S6 S7 S8 S9 S10
MF1
MF2
MF3
MF2
2,761±87 cal kyr BP
6C
6B
9,135±152 cal kyr BP
6A
11,060±73 cal kyr BP
12,631±101 cal kyr BP
15,031±239 cal kyr BP
17,208±140 cal kyr BP
D50 (µm)
10^0 10^1 10^2 10^3
Vigorous bottom current
Reworking
Winnowing
-2 0 2 4
Terrigenous vs. marine input
Ln (K+Fe+Ti)/(Ca+Sr)
MOZAMBIQUE CHANNEL
MOZ4-CSF19
B
M-PC1 (52% variance)
Accumulation of quartz, bioclasts and heavy minerals
Loading
0.4
0.2
0.0
-0.2
-0.4
Al
Si
K
Ca
Ti
Mn
Fe
Br
Rb
Sr
Zr
Terrigenous sediment source
C
M-PC2 (18% variance)
Different terrigenous sediment sources
Loading
0.6
0.4
0.2
0.0
-0.2
Al
Si
K
Ca
Ti
Mn
Fe
Br
Rb
Sr
Zr
Sediment source A (Aeolian)
Sediment source B (Fluvial)
MF1: Sandy contourite
MF2: Muddy contourite
MF3: Muddy hyperpycnite

Figure 4

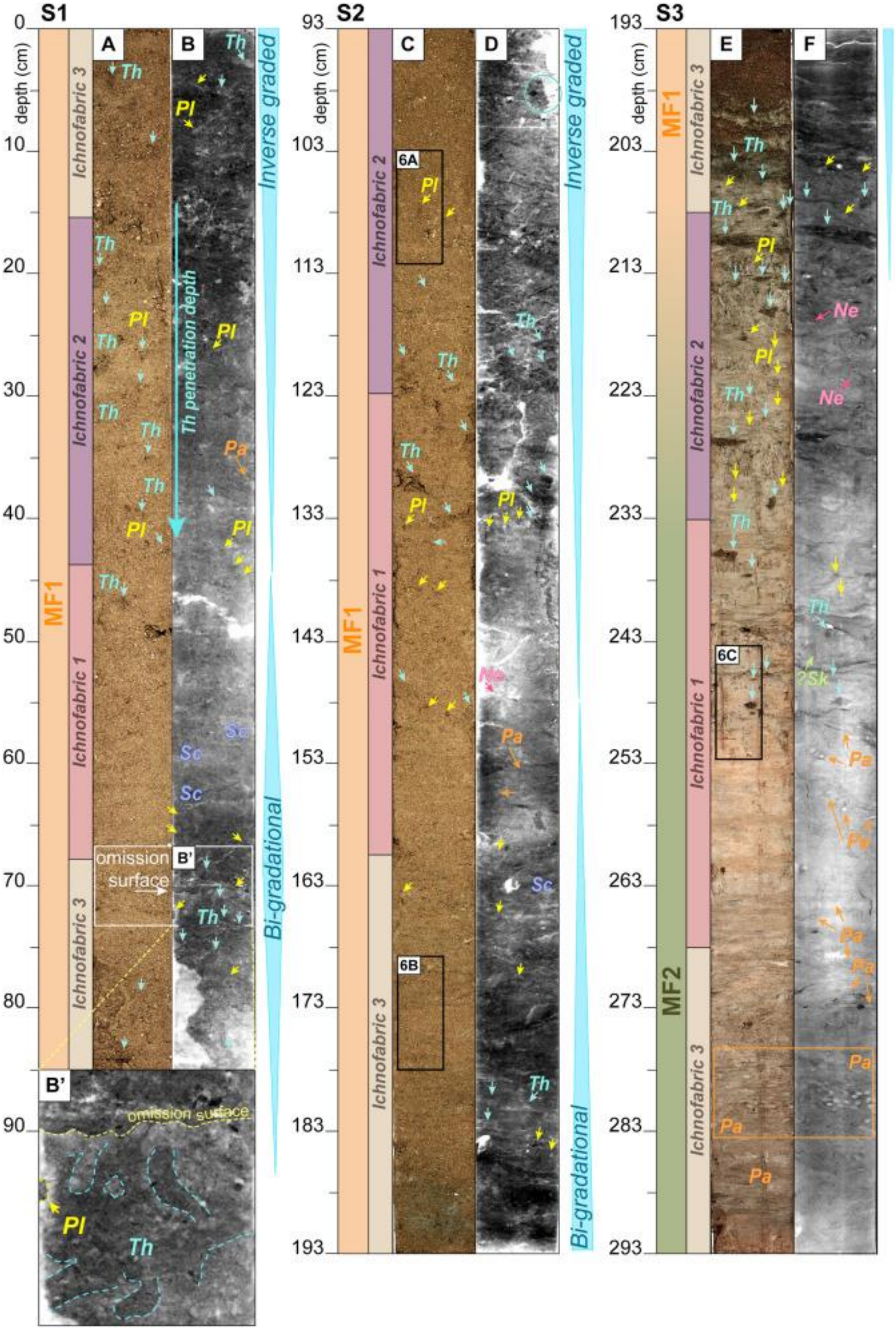
S1
S2
S3
depth (cm)
0
10
20
30
40
50
60
70
80
90
93
103
113
123
133
143
153
163
173
183
193
203
213
223
233
243
253
263
273
283
293
A
B
B'
C
D
E
F
MF1
MF2
Ichnofabric 1
Ichnofabric 2
Ichnofabric 3
Th
Pl
Pa
Sc
Ne
?Sk
Th penetration depth
omission surface
Inverse graded
Bi-gradational
6A
6B
6C

Figure 5

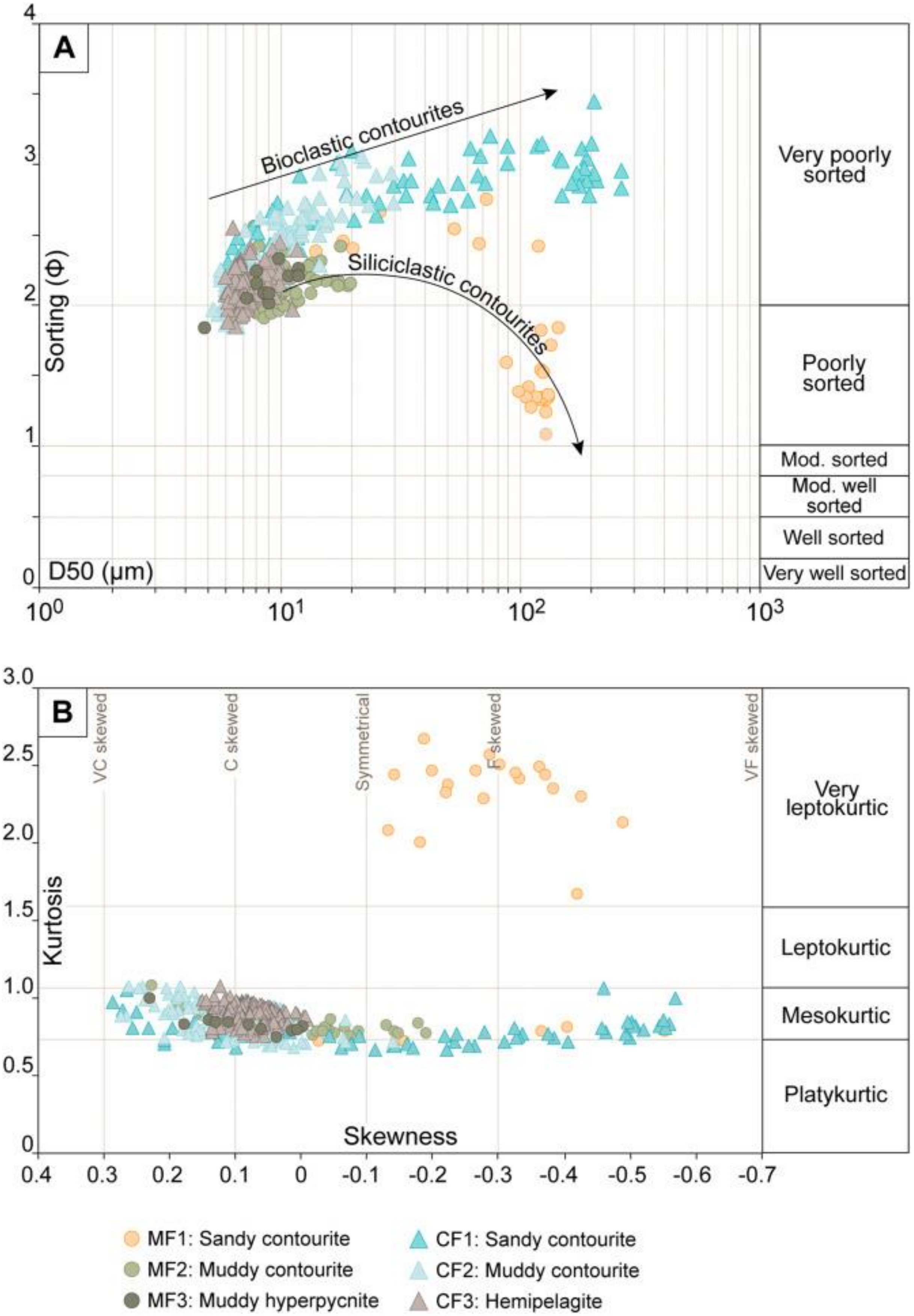
A
Bioclastic contourites
Siliciclastic contourites
Sorting (Φ)
D50 (µm)
0
1
2
3
4
10^0
10^1
10^2
10^3
Very poorly sorted
Poorly sorted
Mod. sorted
Mod. well sorted
Well sorted
Very well sorted
B
Kurtosis
Skewness
VC skewed
C skewed
Symmetrical
F skewed
VF skewed
0
0.5
1.0
1.5
2.0
2.5
3.0
0.4
0.3
0.2
0.1
0
-0.1
-0.2
-0.3
-0.4
-0.5
-0.6
-0.7
Very leptokurtic
Leptokurtic
Mesokurtic
Platykurtic
MF1: Sandy contourite
MF2: Muddy contourite
MF3: Muddy hyperpycnite
CF1: Sandy contourite
CF2: Muddy contourite
CF3: Hemipelagite

Figure 6

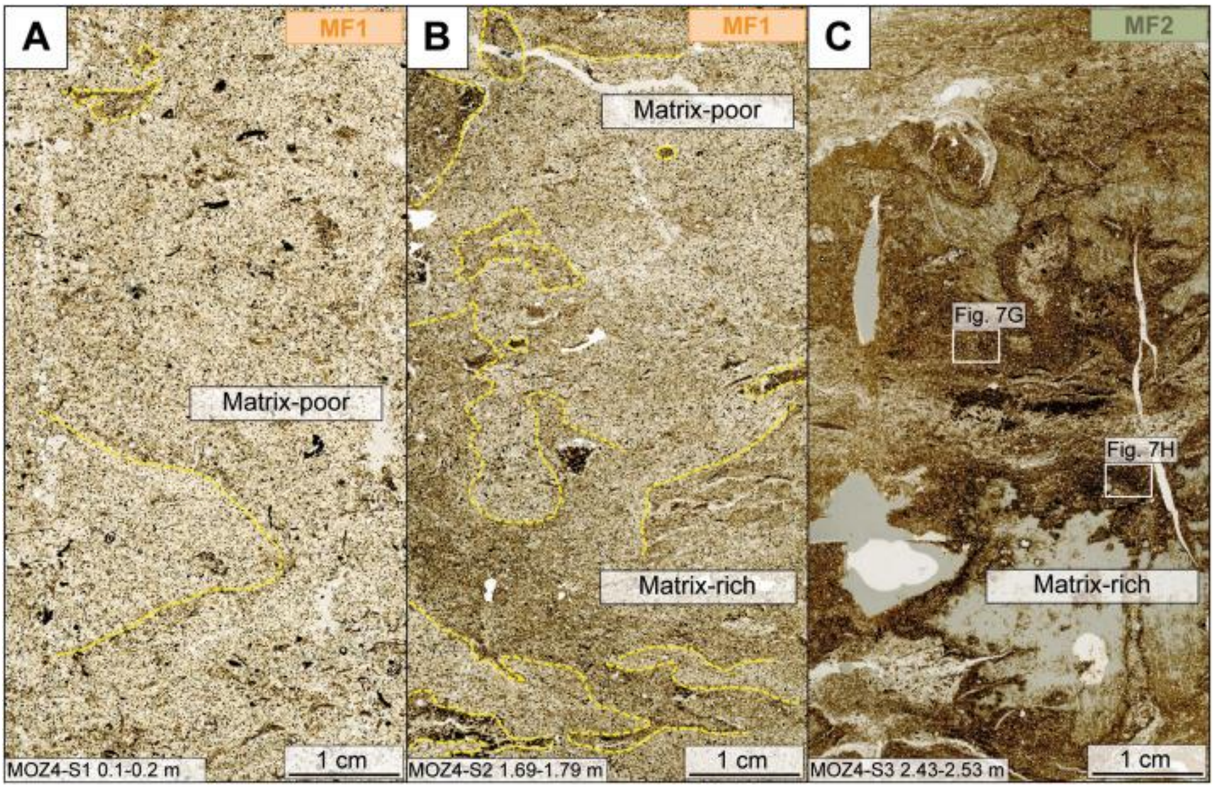
A
MF1
Matrix-poor
MOZ4-S1 0.1-0.2 m
1 cm
B
MF1
Matrix-poor
Matrix-rich
MOZ4-S2 1.69-1.79 m
1 cm
C
MF2
Fig. 7G
Fig. 7H
Matrix-rich
MOZ4-S3 2.43-2.53 m
1 cm

Figure 7

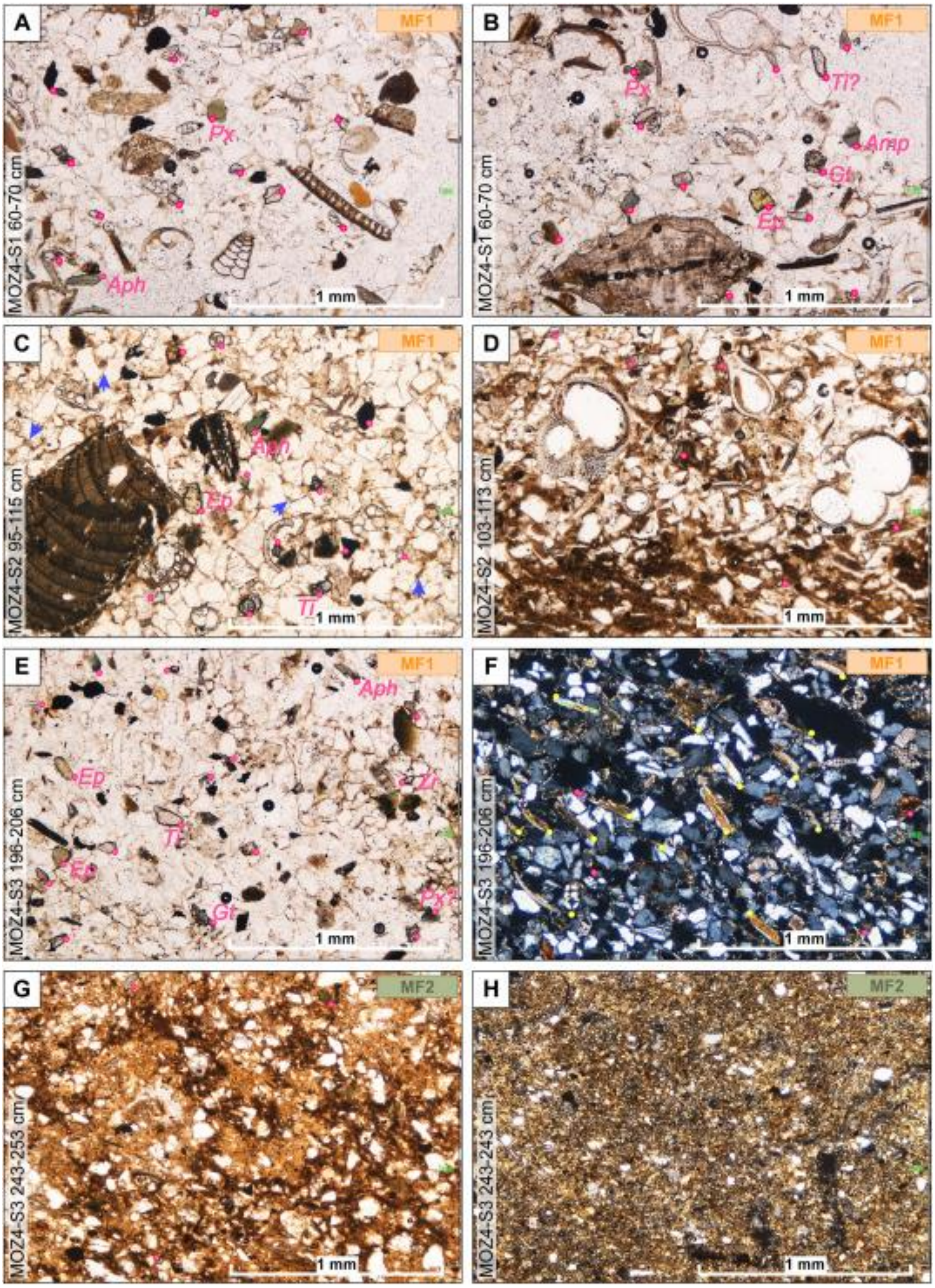

A
MF1
MOZ4-S1 60-70 cm
Px
Aph
1 mm
B
MF1
Px
Tl?
Amp
Gt
Ep
MOZ4-S1 60-70 cm
1 mm
C
MF1
Aph
Ep
Tl
MOZ4-S2 95-115 cm
1 mm
D
MF1
MOZ4-S2 103-113 cm
1 mm
E
MF1
Aph
Ep
Zr
Tl
Ep
Gt
Px?
MOZ4-S3 196-206 cm
1 mm
F
MF1
MOZ4-S3 196-206 cm
1 mm
G
MF2
MOZ4-S3 243-253 cm
1 mm
H
MF2
MOZ4-S3 243-243 cm
1 mm

Figure 8

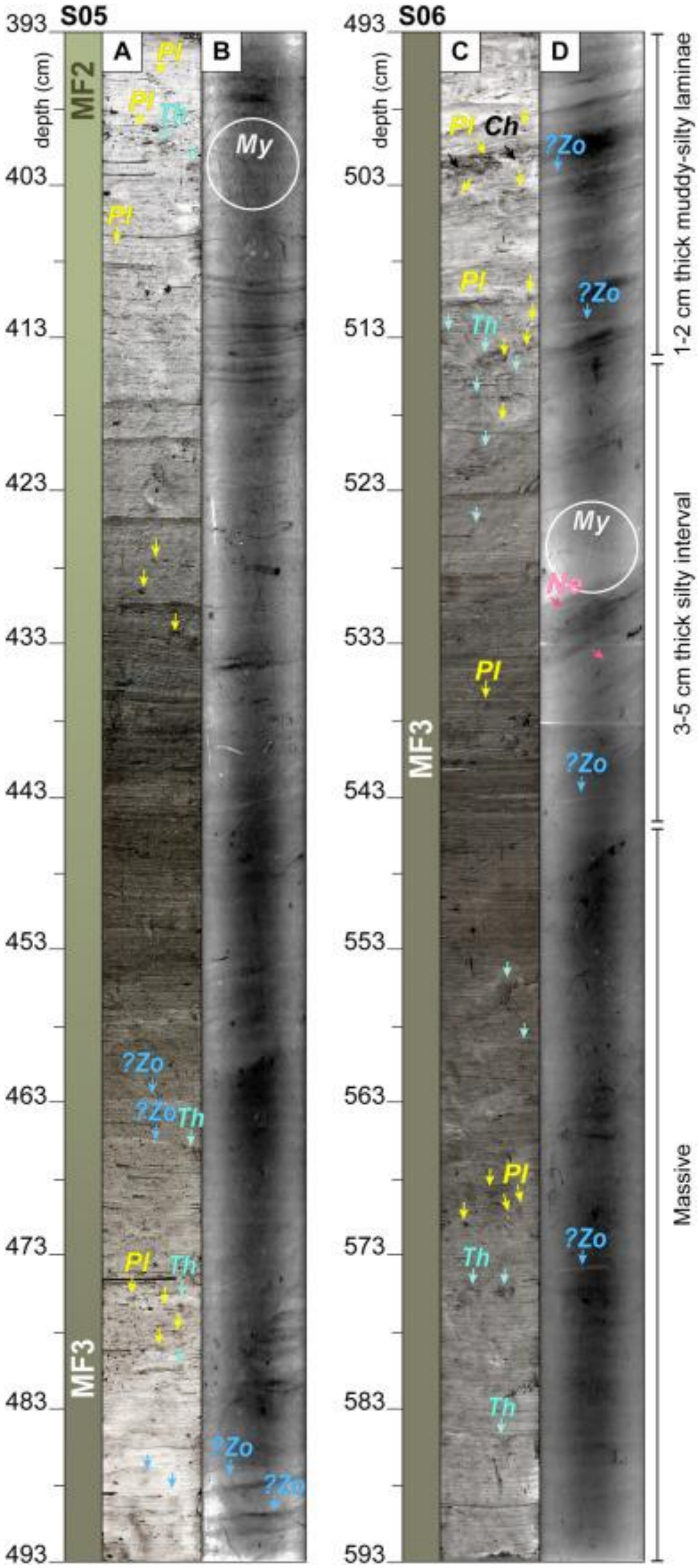
S05
S06
depth (cm)
393
403
413
423
433
443
453
463
473
483
493
503
513
523
533
543
553
563
573
583
593
A
B
C
D
MF2
MF3
Pl
Th
My
?Zo
Ch
Ne
1-2 cm thick muddy-silty laminae
3-5 cm thick silty interval
Massive

Figure 9

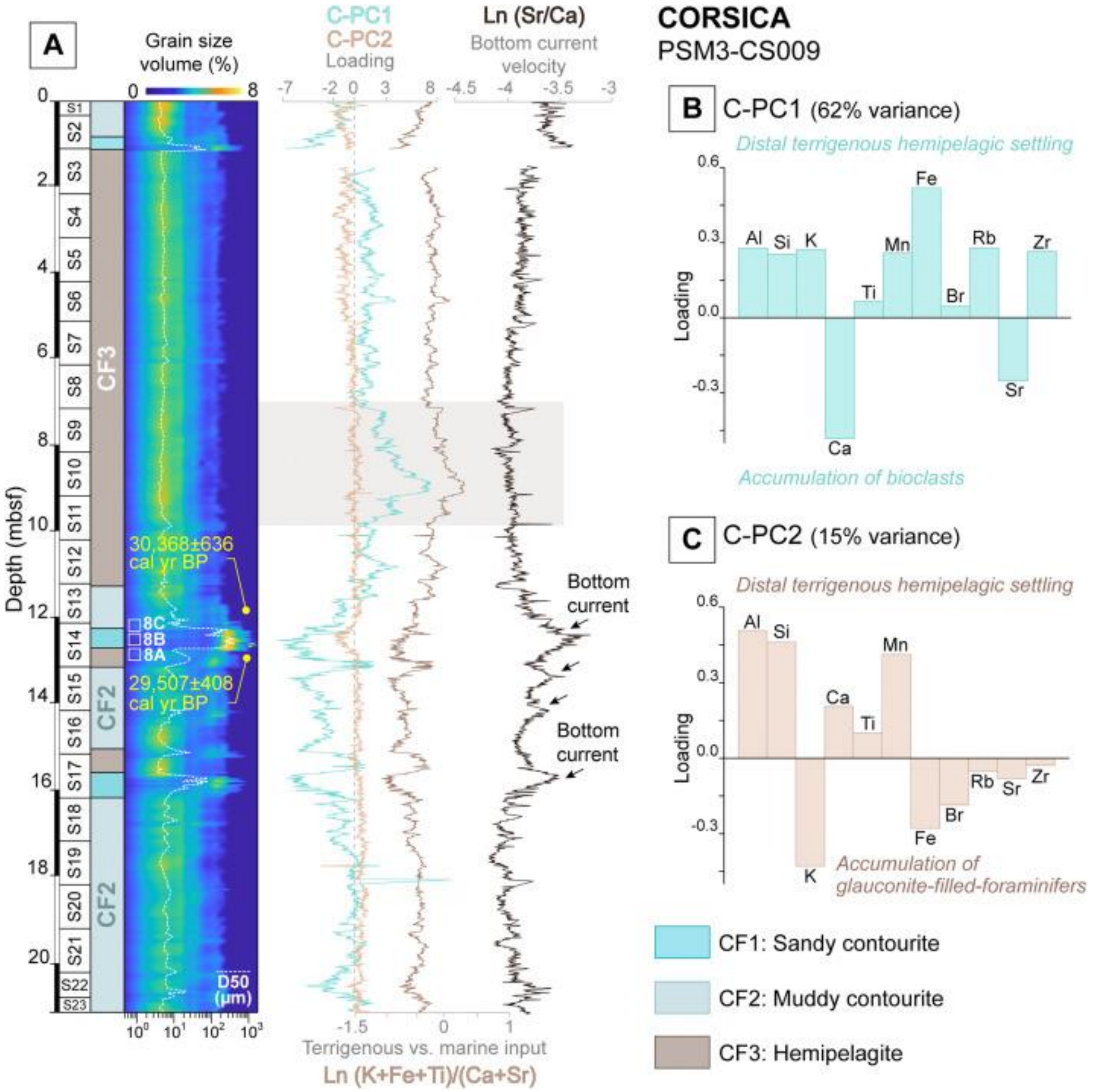
A
Grain size volume (%)
0
8
C-PC1
C-PC2
Loading
-7
-2
0
3
8
Ln (Sr/Ca)
Bottom current velocity
-4.5
-4
-3.5
-3
CORSICA
PSM3-CS009
Depth (mbsf)
0
2
4
6
8
10
12
14
16
18
20
S1
S2
S3
S4
S5
S6
S7
S8
S9
S10
S11
S12
S13
S14
S15
S16
S17
S18
S19
S20
S21
S22
S23
CF3
CF2
CF2
30,368±636 cal yr BP
8C
8B
8A
29,507±408 cal yr BP
D50 (µm)
10^0
10^1
10^2
10^3
-1.5
0
1
Terrigenous vs. marine input
Ln (K+Fe+Ti)/(Ca+Sr)
Bottom current
Bottom current
B
C-PC1 (62% variance)
Distal terrigenous hemipelagic settling
Accumulation of bioclasts
Loading
0.6
0.3
0.0
-0.3
Al
Si
K
Ca
Ti
Mn
Fe
Br
Rb
Sr
Zr
C
C-PC2 (15% variance)
Distal terrigenous hemipelagic settling
Accumulation of glauconite-filled-foraminifers
Loading
0.6
0.3
0.0
-0.3
Al
Si
K
Ca
Ti
Mn
Fe
Br
Rb
Sr
Zr
CF1: Sandy contourite
CF2: Muddy contourite
CF3: Hemipelagite

Figure 10

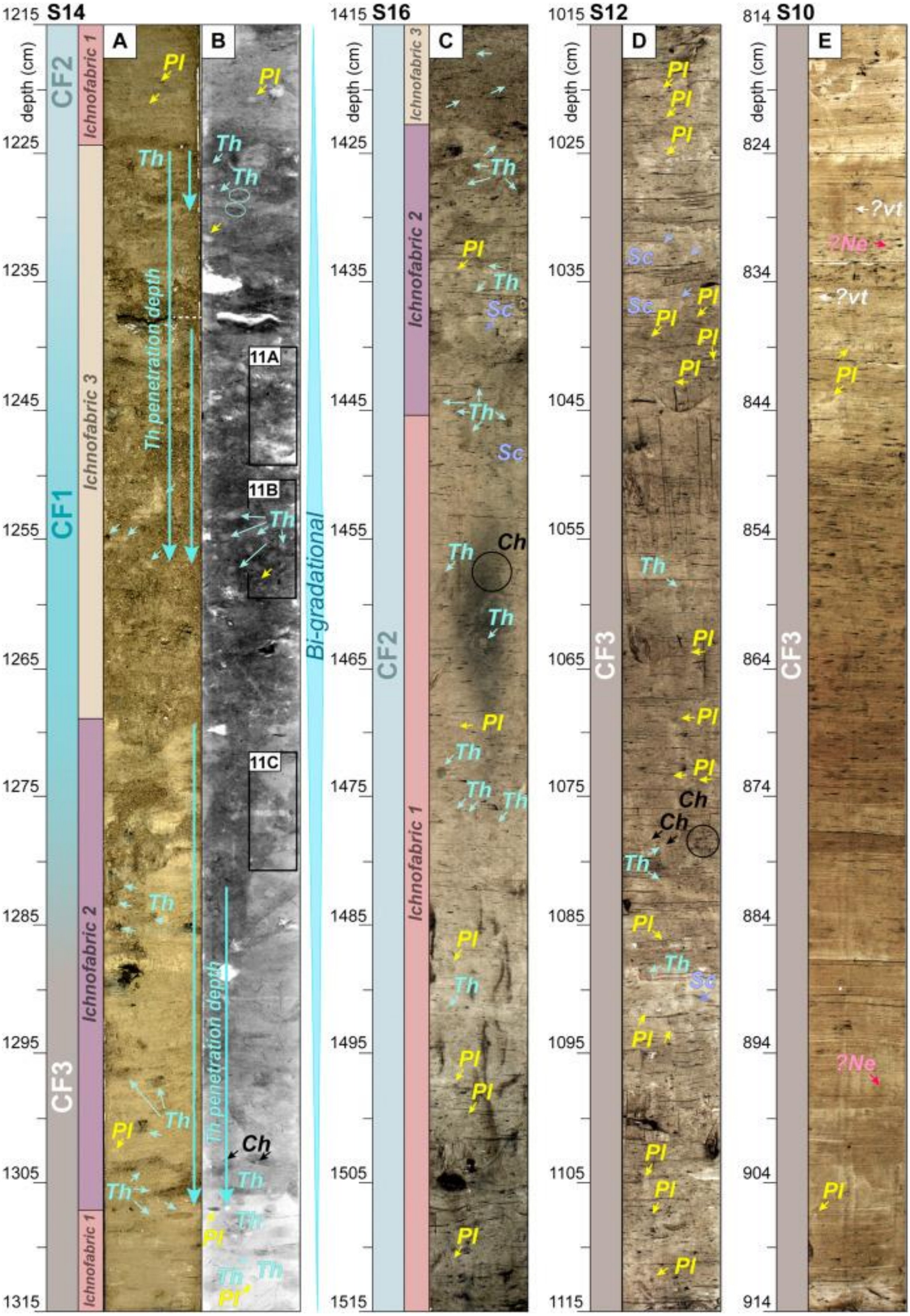

S14
S16
S12
S10
A
B
C
D
E
depth (cm)
1215
1225
1235
1245
1255
1265
1275
1285
1295
1305
1315
1415
1425
1435
1445
1455
1465
1475
1485
1495
1505
1515
1015
1025
1035
1045
1055
1065
1075
1085
1095
1105
1115
814
824
834
844
854
864
874
884
894
904
914
CF1
CF2
CF3
Ichnofabric 1
Ichnofabric 2
Ichnofabric 3
Th penetration depth
Bi-gradational
11A
11B
11C
Pl
Th
Ch
Sc
?vt
?Ne

Figure 11

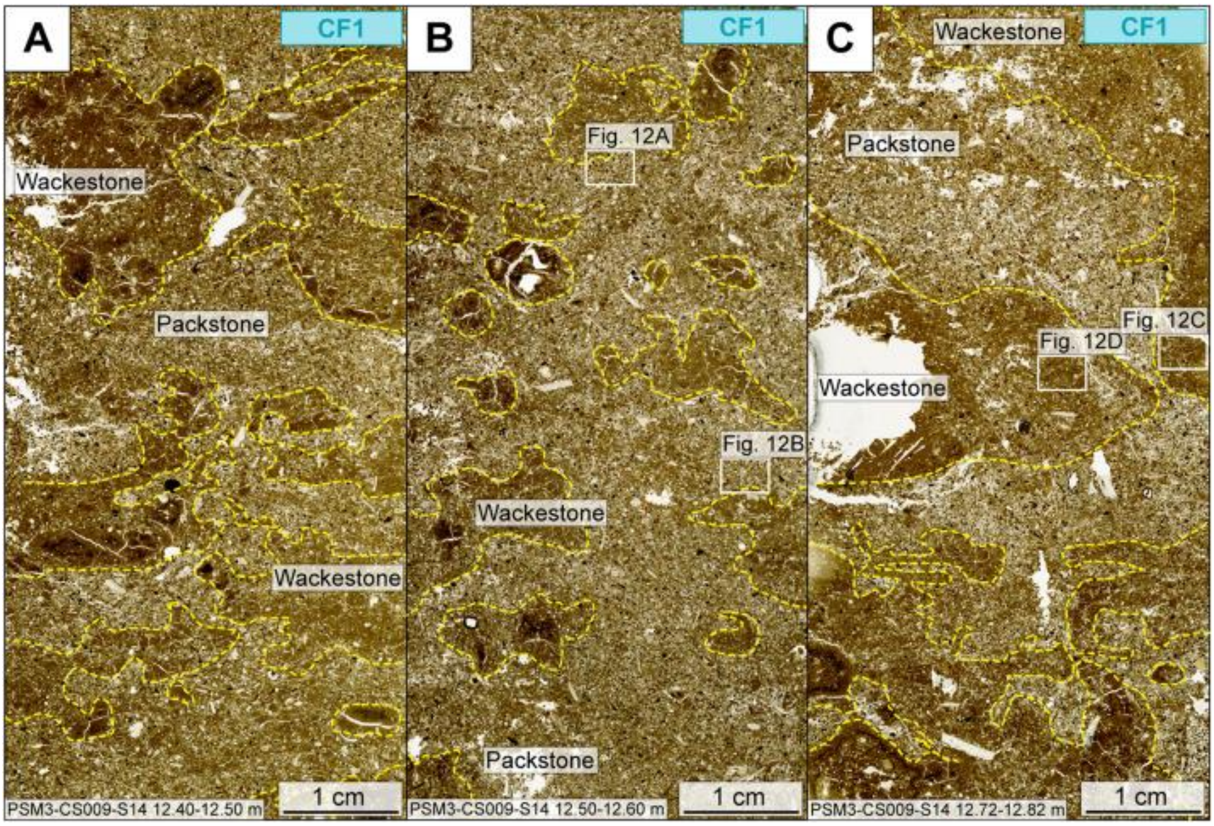
A
CF1
Wackestone
Packstone
Wackestone
PSM3-CS009-S14 12.40-12.50 m
1 cm
B
CF1
Fig. 12A
Fig. 12B
Wackestone
Packstone
PSM3-CS009-S14 12.50-12.60 m
1 cm
C
Wackestone
CF1
Packstone
Fig. 12C
Fig. 12D
Wackestone
PSM3-CS009-S14 12.72-12.82 m
1 cm

Figure 12

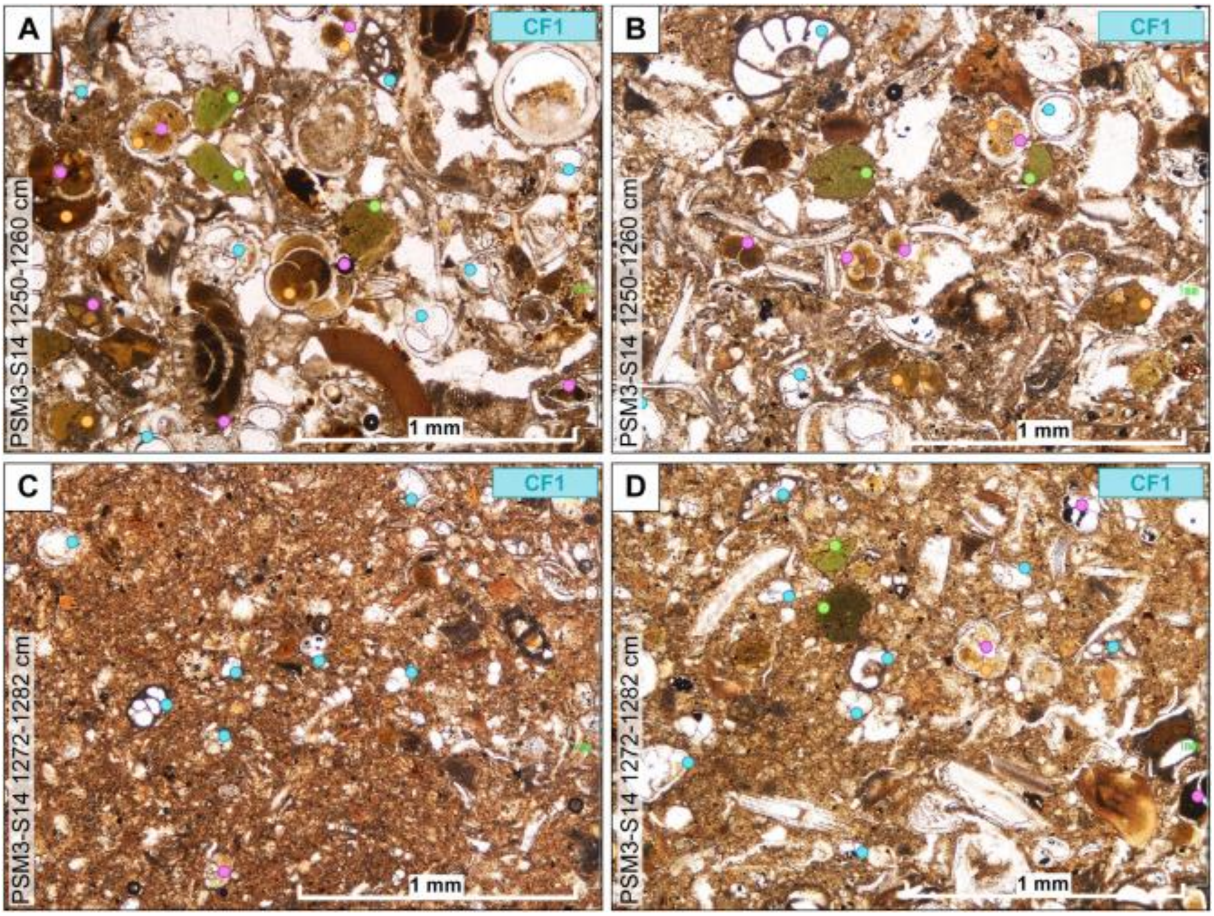
A
CF1
PSM3-S14 1250-1260 cm
1 mm
B
CF1
PSM3-S14 1250-1260 cm
1 mm
C
CF1
PSM3-S14 1272-1282 cm
1 mm
D
CF1
PSM3-S14 1272-1282 cm
1 mm

Figure 13

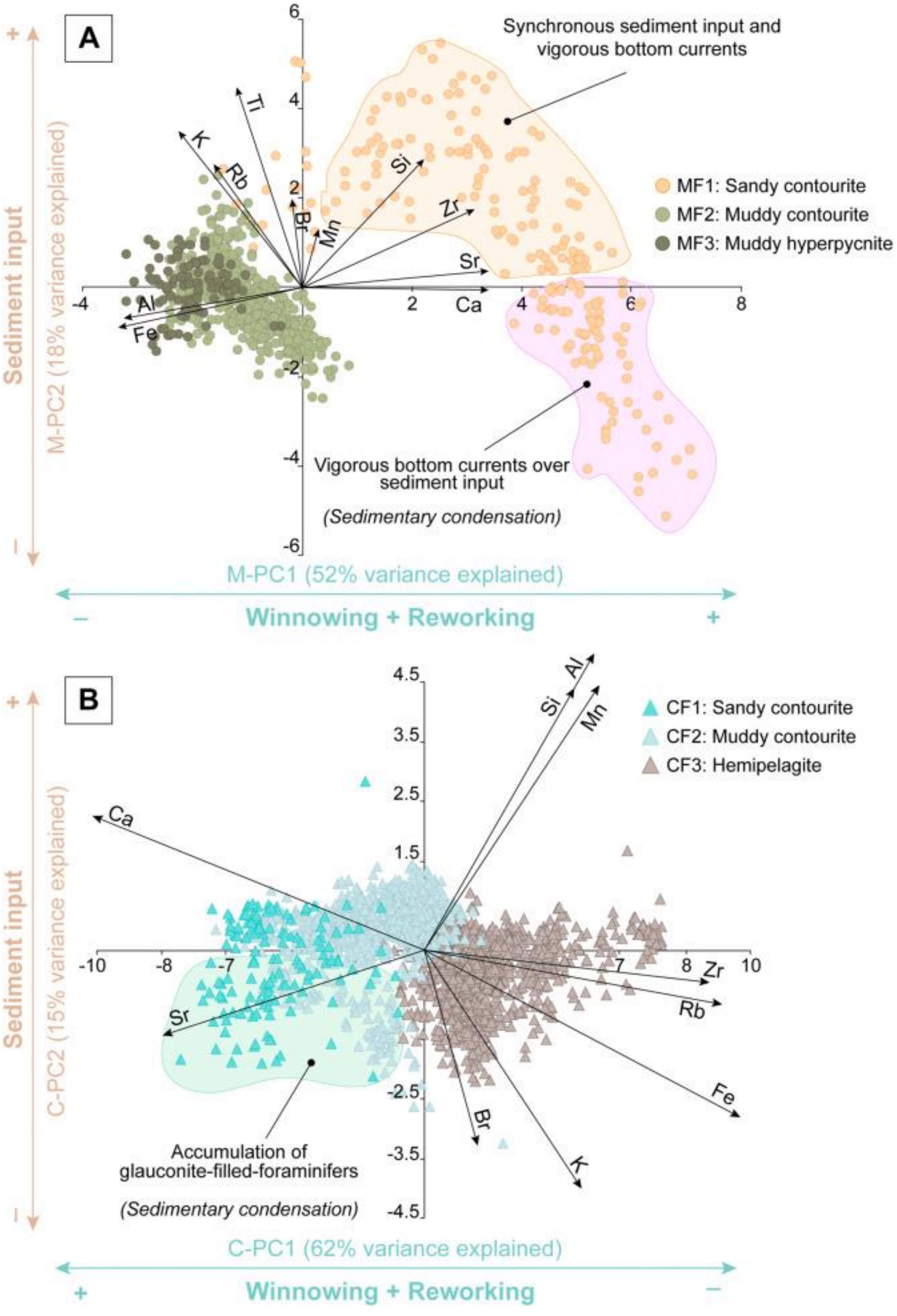
A
Synchronous sediment input and vigorous bottom currents
MF1: Sandy contourite
MF2: Muddy contourite
MF3: Muddy hyperpycnite
Vigorous bottom currents over sediment input
(Sedimentary condensation)
Ti
K
Rb
Br
Mn
Si
Zr
Sr
Ca
Al
Fe
6
4
2
-2
-4
-6
-4
2
4
6
8
Sediment input
M-PC2 (18% variance explained)
M-PC1 (52% variance explained)
Winnowing + Reworking
B
CF1: Sandy contourite
CF2: Muddy contourite
CF3: Hemipelagite
Accumulation of glauconite-filled-foraminifers
(Sedimentary condensation)
Ca
Si
Al
Mn
Sr
Zr
Rb
Fe
Br
K
4.5
3.5
2.5
1.5
-2.5
-3.5
-4.5
-10
-8
-7
7
8
10
Sediment input
C-PC2 (15% variance explained)
C-PC1 (62% variance explained)
Winnowing + Reworking

Figure 14

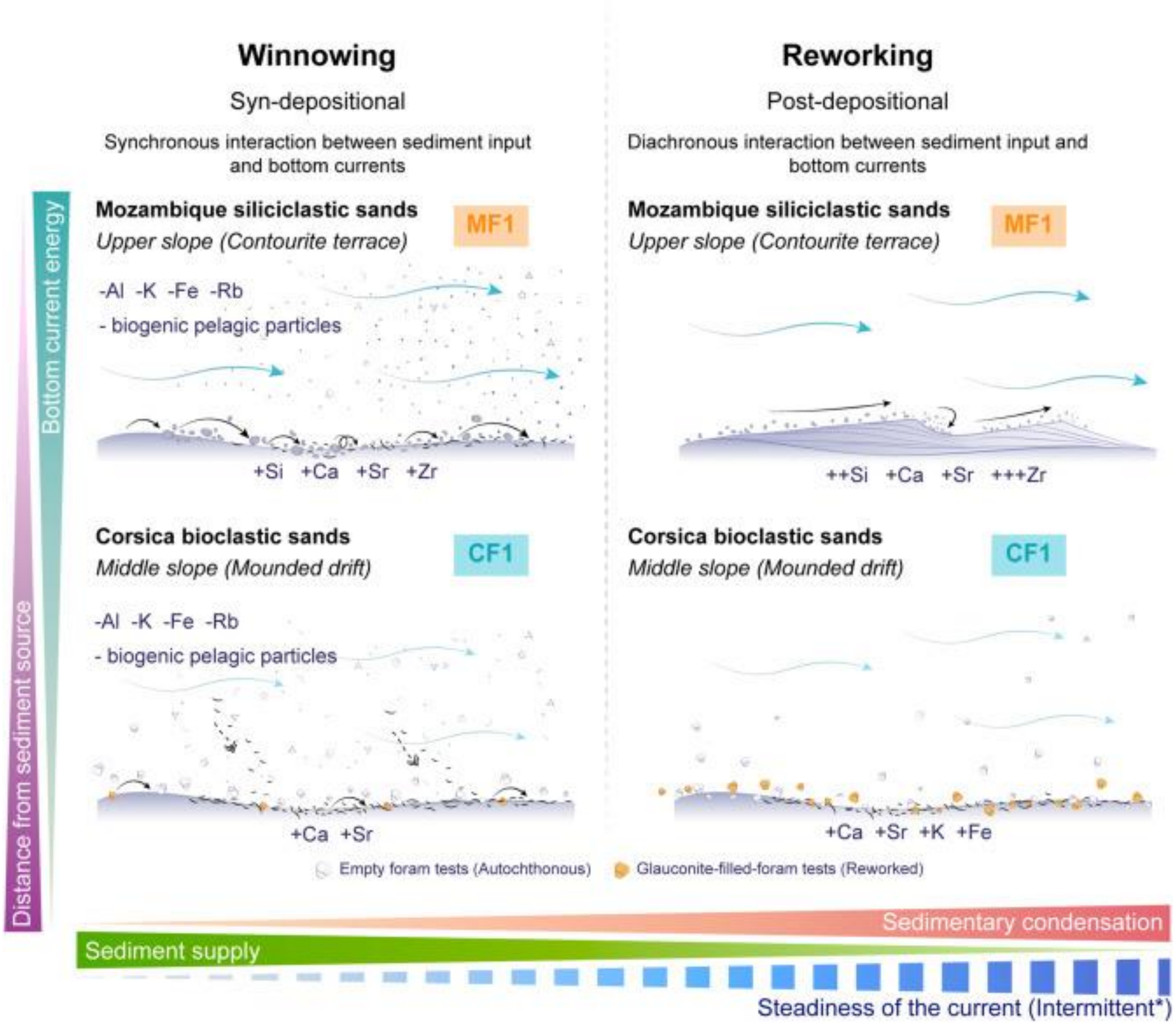
Winnowing
Syn-depositional
Synchronous interaction between sediment input and bottom currents
Reworking
Post-depositional
Diachronous interaction between sediment input and bottom currents
Mozambique siliciclastic sands
Upper slope (Contourite terrace)
MF1
-Al -K -Fe -Rb
- biogenic pelagic particles
+Si +Ca +Sr +Zr
Mozambique siliciclastic sands
Upper slope (Contourite terrace)
MF1
++Si +Ca +Sr +++Zr
Corsica bioclastic sands
Middle slope (Mounded drift)
CF1
-Al -K -Fe -Rb
- biogenic pelagic particles
+Ca +Sr
Corsica bioclastic sands
Middle slope (Mounded drift)
CF1
+Ca +Sr +K +Fe
Empty foram tests (Autochthonous)
Glauconite-filled-foram tests (Reworked)
Bottom current energy
Distance from sediment source
Sedimentary condensation
Sediment supply
Steadiness of the current (Intermittent*)

Figure 15

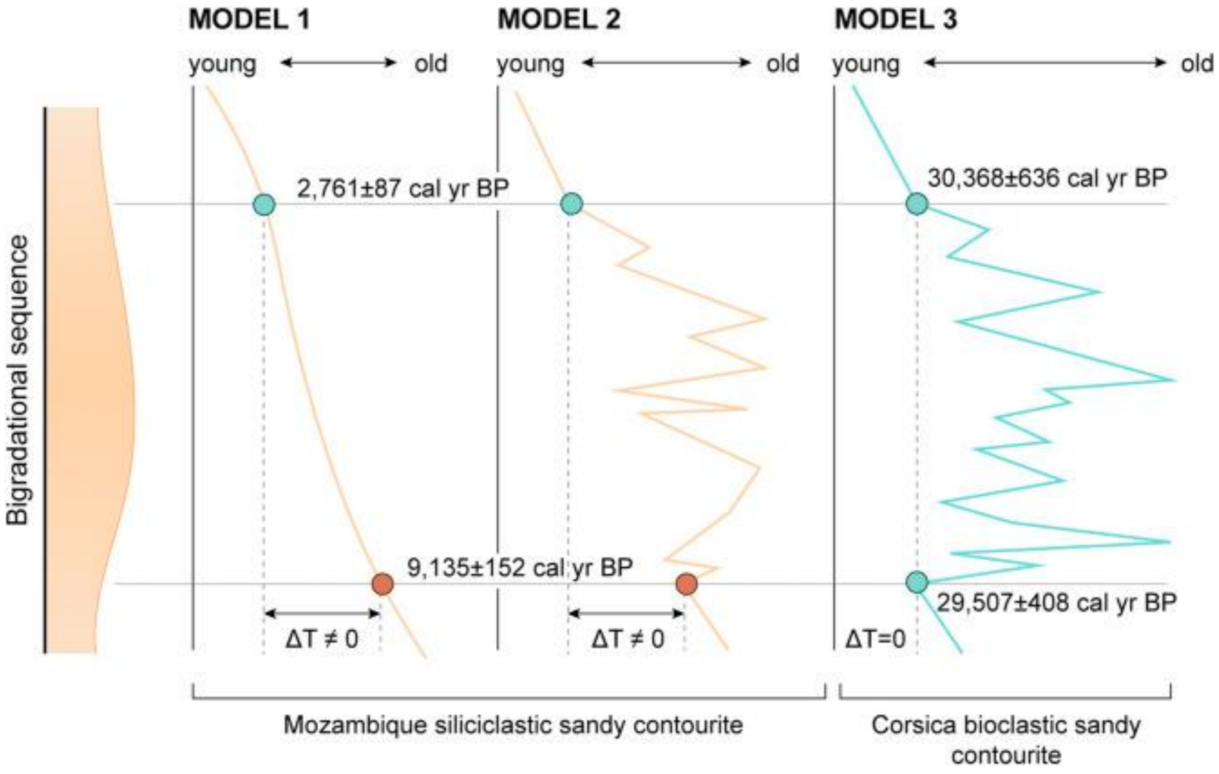

MODEL 1
young
old
MODEL 2
young
old
MODEL 3
young
old
Bigradational sequence
2,761±87 cal yr BP
9,135±152 cal yr BP
30,368±636 cal yr BP
29,507±408 cal yr BP
ΔT ≠ 0
ΔT ≠ 0
ΔT=0
Mozambique siliciclastic sandy contourite
Corsica bioclastic sandy contourite

Figure 16

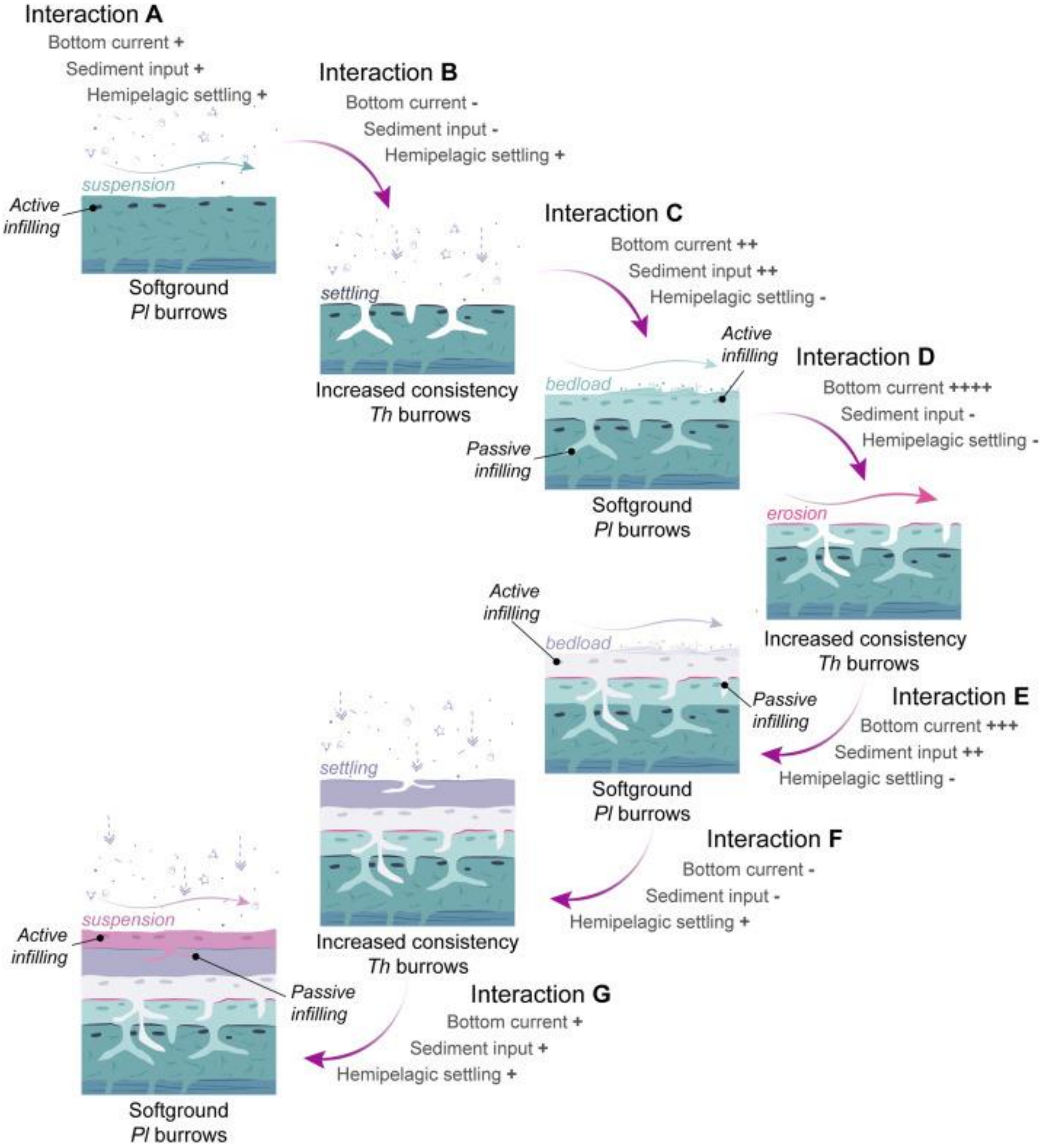

Interaction A
Bottom current +
Sediment input +
Hemipelagic settling +
suspension
Active infilling
Softground
Pl burrows
Interaction B
Bottom current -
Sediment input -
Hemipelagic settling +
settling
Increased consistency
Th burrows
Interaction C
Bottom current ++
Sediment input ++
Hemipelagic settling -
Active infilling
bedload
Passive infilling
Softground
Pl burrows
Interaction D
Bottom current ++++
Sediment input -
Hemipelagic settling -
erosion
Increased consistency
Th burrows
Active infilling
bedload
Passive infilling
Softground
Pl burrows
Interaction E
Bottom current +++
Sediment input ++
Hemipelagic settling -
settling
Increased consistency
Th burrows
Interaction F
Bottom current -
Sediment input -
Hemipelagic settling +
suspension
Active infilling
Passive infilling
Softground
Pl burrows
Interaction G
Bottom current +
Sediment input +
Hemipelagic settling +

Figure 17

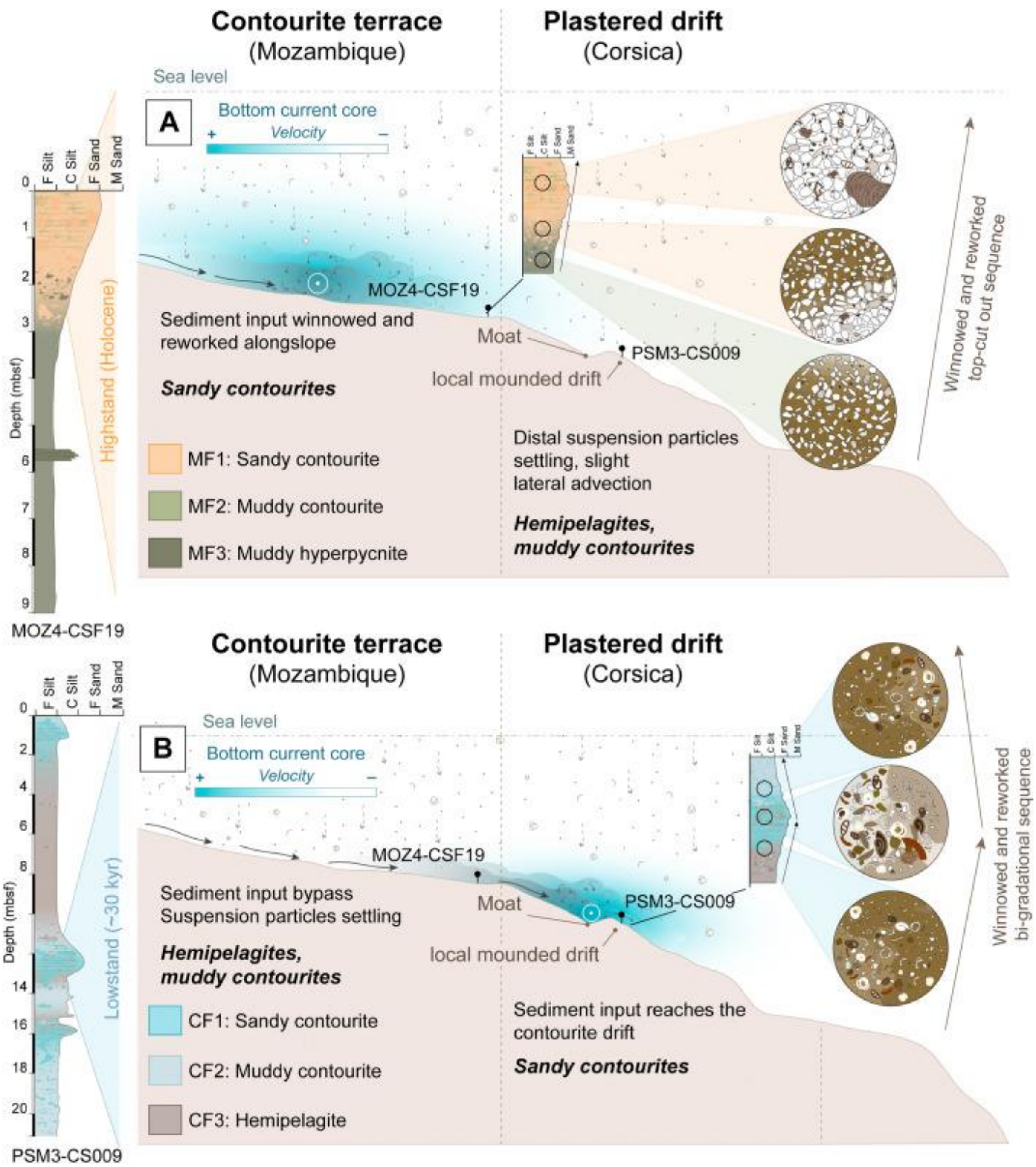
Contourite terrace
(Mozambique)
Plastered drift
(Corsica)
Sea level
A
Bottom current core
+ Velocity −
MOZ4-CSF19
Sediment input winnowed and reworked alongslope
Sandy contourites
Moat
local mounded drift
PSM3-CS009
Distal suspension particles settling, slight lateral advection
Hemipelagites, muddy contourites
MF1: Sandy contourite
MF2: Muddy contourite
MF3: Muddy hyperpycnite
Winnowed and reworked top-cut out sequence
F Silt
C Silt
F Sand
M Sand
Depth (mbsf)
0
1
2
3
6
7
8
9
Highstand (Holocene)
MOZ4-CSF19
Contourite terrace
(Mozambique)
Plastered drift
(Corsica)
Sea level
B
Bottom current core
+ Velocity −
MOZ4-CSF19
Sediment input bypass
Suspension particles settling
Hemipelagites, muddy contourites
Moat
local mounded drift
PSM3-CS009
Sediment input reaches the contourite drift
Sandy contourites
CF1: Sandy contourite
CF2: Muddy contourite
CF3: Hemipelagite
Winnowed and reworked bi-gradational sequence
F Silt
C Silt
F Sand
M Sand
Depth (mbsf)
0
2
4
6
8
14
16
18
20
Lowstand (~30 kyr)
PSM3-CS009